Using Long Term Composites and Objective Tracking to Assess The Spatiotemporal Characteristics, Variability, and Future Changes in Atmospheric Rivers

By

HÉCTOR ALEJANDRO INDA DÍAZ
DISSERTATION

Submitted in partial satisfaction of the requirements for the degree of

DOCTOR OF PHILOSOPHY

in

Atmospheric Science

in the

OFFICE OF GRADUATE STUDIES

of the

UNIVERSITY OF CALIFORNIA

DAVIS

Approved:

Paul Ullrich, Chair

William Collins

Shu-Hua Chen

Travis O'Brien

Committee in Charge

2022

"The important thing is not to stop questioning. Curiosity has its own reason for existence. One cannot help but be in awe when he contemplates the mysteries of eternity, of life, of the marvelous structure of reality. It is enough if one tries merely to comprehend a little of this mystery each day"

— Albert Einstein

I want to especially thank my Ph.D. advisor, Travis O'Brien. Travis, you have been an extraordinary advisor, colleague, teacher, and friend. This work could not exist without your help and support.

This dissertation is dedicated to my parents and my brothers, whose example has set my path and guided me along with it. Wherever you are, you are always with me.

I dedicate this work to you, Miriam. Your love and unconditional support have given me the strength to get here. Thank you for sharing with me this journey; everything is better with you in my life.

Contents

List of Figures

List of Tables

Abstract

Atmospheric rivers (ARs) are large and narrow filaments of poleward horizontal water vapor transport. AR carry over 90% of moisture from the tropics to higher latitudes but cover only between 2% and 10% of the earth's surface. When ARs are forced upwards frequently lead to heavy precipitation. ARs are associated with up to half of the extreme events in the top 2% of the precipitation and wind distribution across most mid-latitude regions. ARs can lead to hydrological hazards, and a better understanding of AR can help in the study, forecasting, and communication of flooding. Because of its direct relationship with horizontal vapor transport, extreme precipitation, and overall AR impacts over land, the AR size is an important characteristic that needs to be better understood. Furthermore, most of the ARs research work focuses on midlatitudes and polar regions. It is not until recently that ARs in tropical latitudes are starting to generate interest within the scientific AR community. We develop and implement five size estimation methods independent of the AR detection algorithms and use them to characterize the size of ARs. We create North American landfalling ARs composites using ERA5 reanalysis data in the 1980-2017 period. To study how AR size changes with future climate scenarios, we use data from the Coupled Model Intercomparison Project 5 and 6 (CMIP5/6) to create historical and future AR composites in the 1950-2100 period. We apply our size estimation methods to study how AR size responds to climate change. Additionally, we use data from the ERA-20C reanalysis to study the relationship between lower latitude ARs and the extreme precipitation in Central-Western Mexico (CWM) during the dry-season (November-March) in the 1900-2010 period.

North American landfall ARs (NALFARs) that originate in the Northwest Pacific (WP) (100°E-180°E) have larger sizes and are more zonally oriented than those from the Northeast Pacific (EP) (180°E-240°E). ARs become smaller through their life cycle, mainly due to reductions in their width. They also become more meridionally oriented towards the end of their life cycle. NALFARs become smaller through their life cycle, mainly due to reductions in their width. They also become more meridionally oriented towards the end of their life cycle. Overall, the size estimation methods developed in this work provide a range of AR

areas (between $7x10^{11}m^2$ and 10^{13} m^2) that is several orders of magnitude narrower than the current estimation by the AR detectors from the Atmospheric River Tracking Method Intercomparison Project (ARTMIP).

From a global AR size analysis, we show an increase between 10% and 21% in the background IVT field among CMIP5/6 models. According to our results, AR width is more sensitive to climate change and has a larger contribution than length to the change in the AR area. We find a mean AR area of $3.15x10^6$ ($2.32x10^6$-$3.98x10^6$) km^2 for historical runs, and $3.42x10^6$ ($2.73x10^6$-$4.11x10^6$) km^2 for future runs. Most size estimation methods and CMIP5/6 models show positive trends in AR area, length, and width, between historical and strong radiative forcing future simulations (CMIP5: RCP-8.5, CMIP6: SSP-858). Regardless of the individual sign in AR size change, the mean AR cross-section water vapor transport increases between 8% and 37% for future simulations. Additionally, our results suggest that NALFARs are more likely to penetrate further inland under climate change.

Regarding landfalling ARs in CWM, our results suggest that more than 25% of the extreme dry-season precipitation is associated with AR-like events, with up to 75% in December and January. This AR-associated precipitation is associated with an enhanced mean vertically integrated water vapor (IWV) and horizontal vapor transport (IVT) fields (30 kg m^{-2} and IVT 400 kg $m^{-1}s^{-1}$, respectively). The meteorological state of the atmosphere shows "ideal" conditions for orographic precipitation due to landfalling ARs: high plume of horizontal vapor transport perpendicular to the mountain range. These events are associated with a weakening of the westward equatorial IVT and a tropospheric wave pattern, observable in the mean sea level pressure and geopotential height anomalies.

We believe that the size estimation methods developed in this work provide statistical constraints for AR size and geometry, and how they change in future climates. These results could help as a reference for tuning existing ARDTs or designing new AR detection algorithms. Furthermore, we demonstrate the relationship between ARs and winter rainfall in CWM. This relationship leaves the question open of how similar are these tropical ARs to the more studied higher latitude ARs and how they will respond in a warming world.

Chapter 1

Introduction

Atmospheric rivers (ARs) are long, narrow filaments of poleward water vapor transport from the tropics. They were first described by Newell and Zhu (1994) and Zhu and Newell (1998) as high tropospheric water vapor flux with a filamentary structure or "tropospheric rivers". AR carry over 90% of moisture from the tropics to higher latitudes but cover only ∼10% of the total earth circumference at a given latitude (Zhu and Newell, 1998) (between 2 and 10 percent of the earth's surface (O'Brien et al., 2021)). ARs are associated with up to half of the extreme events in the top 2% of the precipitation and wind distribution across most mid-latitude regions (Waliser and Guan, 2017). Moreover, landfalling ARs are associated with about 40-75% of extreme wind and precipitation events over 40% of the world's coastlines (Waliser and Guan, 2017). Midlatitude continental regions around the world (western North America, South America, Europe, and South Africa) have large amounts of precipitation and with hydrological impacts associated with ARs (Neiman et al., 2002, 2008; Ralph et al., 2004, 2005; Leung and Qian, 2009; Guan et al., 2010; Viale and Nuñez, 2011; Warner et al., 2012; Neiman et al., 2013; Ralph et al., 2013; Lavers and Villarini, 2013b; Rutz et al., 2014; Ramos et al., 2015; Gimeno et al., 2016; Waliser and Guan, 2017; Blamey et al., 2018; Viale et al., 2018; Ramos et al., 2019; Huang et al., 2021).

ARs can have both positive and negative effects in continental regions. Their absence can lead to droughts (Dettinger, 2013), whereas numerous ARs can lead to flooding and other hydrological hazards (Ralph et al., 2006; Dettinger, 2011; Ralph and Dettinger, 2011; Lavers and Villarini, 2013a). ARs have significant consequences on the hydrological cycle of regions like California and contribute to the accumulation of the snowpack and the reservoir level and water availability (Dirmeyer and Brubaker, 2007; Guan et al., 2010; Kim et al., 2013; Goldenson et al., 2018; Eldardiry et al., 2019). Ultimately, a better understanding of

AR can help in the study, forecasting, and communication of flooding, droughts, and water management (Lavers et al., 2016b,a; Ralph et al., 2019b). Landfalling ARs provide water resources to over 300 million people (Paltan et al., 2017), having a substantial hydrological and socioeconomic impact. For some regions, fewer than average ARs could mean drought, whereas a higher number or intensity of ARs can produce floods and other hazards (Dettinger, 2011).

1.1 What is an Atmospheric River?

ARs were first described ARs in the late 1990s as "tropospheric rivers" (Newell and Zhu, 1994; Zhu and Newell, 1998). Since then, there has been a growing interest in studying ARs in the last few decades. Until 2018, there was no "official" definition of what an AR is. An exact definition is still a topic of research and debate. In 2018, a definition was submitted to the AMS Glossary of Meteorology (GoM)[1]: "A long, narrow, and transient corridor of strong horizontal water vapor transport that is typically associated with a low-level jet stream ahead of the cold front of an extratropical cyclone. The water vapor in atmospheric rivers is supplied by tropical and/or extratropical moisture sources. Atmospheric rivers frequently lead to heavy precipitation when forced upward—for example, by mountains or by an ascent in the warm conveyor belt. Horizontal water vapor transport in the midlatitudes occurs primarily in atmospheric rivers and focuses on the lower troposphere. Atmospheric rivers are the largest 'rivers' of fresh water on earth, transporting on average more than double the flow of the Amazon River" (Ralph et al., 2019a). This definition is an outcome of two meetings: a 2015 workshop that gathered more than 25 experts in ARs, warm conveyor belt (WCB), and tropical moisture exports (TMEs) (Dettinger et al., 2015); and the First International Atmospheric Rivers Conference (IARC) in August 2016 (Ralph et al., 2017b), that brought together more than 100 individuals from across the globe for four days to discuss AR dynamics, observations, impacts, climate change implications, and applications (Ralph et al., 2019a).

Observational work using dropsonde measurements deployed from aircraft across 21 land-

[1] `https://glossary.ametsoc.org/wiki/Atmospheric_river`

falling atmospheric rivers along the US West Coast provided an insight into the ARs structure: vertically integrated water vapor (IWV) higher than 20 kg m^{-2} (IWV$\geq$2 cm), wind speed greater than 15 ms^{-1}, concentrated mainly in the lower 3 km of the troposphere, with a horizontal cross-section of $\sim$850 km. Figure 1.1 shows the structure of an average midlatitude AR. Width is defined by the vertically integrated water vapor transport (IVT) $\geq$250 kg $m^{-1}s^{-1}$ (from the surface to 300 hPa), and depth corresponds to the altitude below which 75% of IVT occurs. IVT and IWV are the most common variables used to describe and detect ARs, calculated as:

$$\text{IWV} = -\frac{1}{g}\int_{P_\text{b}}^{p_\text{t}} q dp \approx -\frac{1}{g}\sum_{k=1}^{N} q_k \Delta p_k, \tag{1.1}$$

$$\text{IVT} = \left|-\frac{1}{g}\int_{p_\text{b}}^{p_\text{t}} q\vec{u} dp\right| \approx \left|-\frac{1}{g}\sum_{k=1}^{N} \vec{u}_k\, q_k, \Delta p_k\right| \tag{1.2}$$

where p is pressure, $\vec{u}$ is the horizontal wind vector at a given pressure, P_b and P_t are the bottom and top pressure in the atmosphere, and q is the specific humidity. In Ralph et al. (2017a) and the GoM, P_b and P_t are the surface pressure and 300 hPa. In model and reanalysis data, we can calculate IVT and IWV using the native vertical grid levels of the model, where index k corresponds to model levels going from the surface ($k = 1$) to the top of the model atmosphere ($k = N$), and Δp_k is the difference in level pressures, estimated at level k. Calculating IVT and IWV in the model levels helps reduce the error in calculating the vertical integrals, particularly in continental regions where the topography can allow levels below ground to exist in isobaric coordinates.

1.2 Detecting Atmospheric Rivers and Estimating Their Size

Detecting and defining the boundaries of AR is a particularly complicated task. The Atmospheric River Tracking Method Intercomparison Project (ARTMIP) is an international

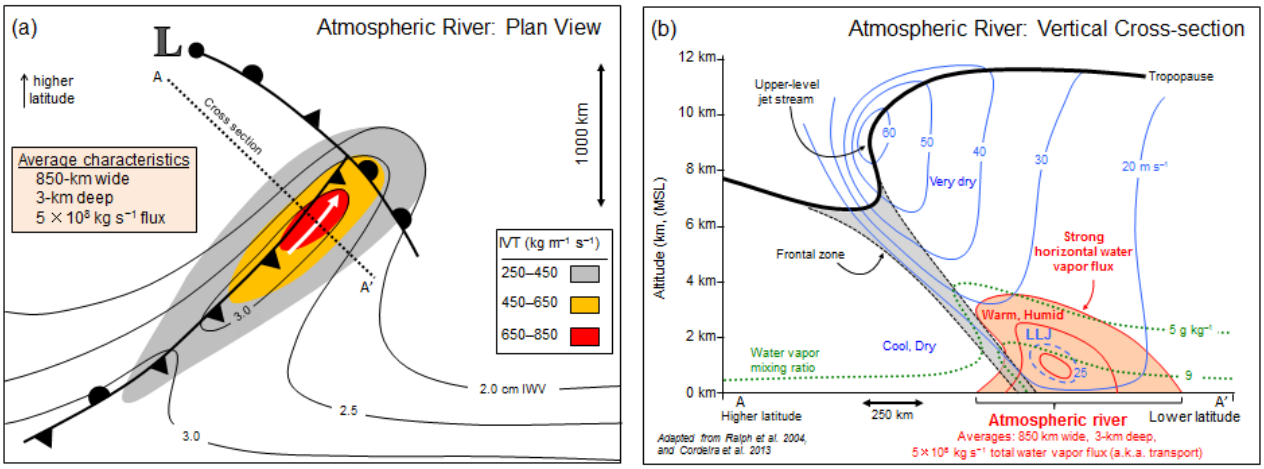

Figure 1.1: (a) Plain view of a mean AR and its associated surface front. IVT [kg $m^{-1}s^{-1}$] is show in color-filled contours; IWV [cm] is shown in solid black contours. (b) Mean AR vertical cross-section. Green dotted contours are water vapor mixing ratio [g kg^{-1}], blue contours are normal to cross-section isotachs [m s^{-1}], and orange filled contours represent the AR core. Water vapor flux corresponds to the transport along an AR, bounded by IVT = 250 kg $m^{-1}s^{-1}$, and by the surface and 300 hPa levels. Figure from the AMS Glossary of Meteorology. Ralph et al. (2017a). **©American Meteorological Society. Used with permission**.

effort to understand and quantify uncertainties in atmospheric river (AR) science based on the choice of detection/tracking methodology and whether and how our scientific understanding of ARs may depend on the detection algorithm.

AR detection and tracking are heavily influenced by how researchers have quantitatively defined this phenomenon and how are AR detectors (ARDTs) designed. For example, the use of 250 kg $m^{-1}s^{-1}$ minimum threshold for IVT does not account for size but only for the concentration of flow and moisture levels. These different rules and algorithm thresholds have resulted in significant uncertainty in estimating the AR size, with areas varying over several orders of magnitude among different detection methods (see Figure 1.2). ARTMIP has (at this moment) 30 different algorithms. The different ARTMIP ARDTs are designed to answer different questions, producing differences in AR climatology (Shields et al., 2018; Rutz et al., 2019; Lora et al., 2020). However, there is still an overlap among the different ARDTs (Payne et al., 2020). Together with horizontal vapor transport, AR size (width, length, and area) is an important characteristic that needs to be better understood, and a robust connection between AR size and their impacts over land and intensity scale still has to be studied and determined. Ralph et al. (2019a) introduced a scale to categorize AR strength based on vapor

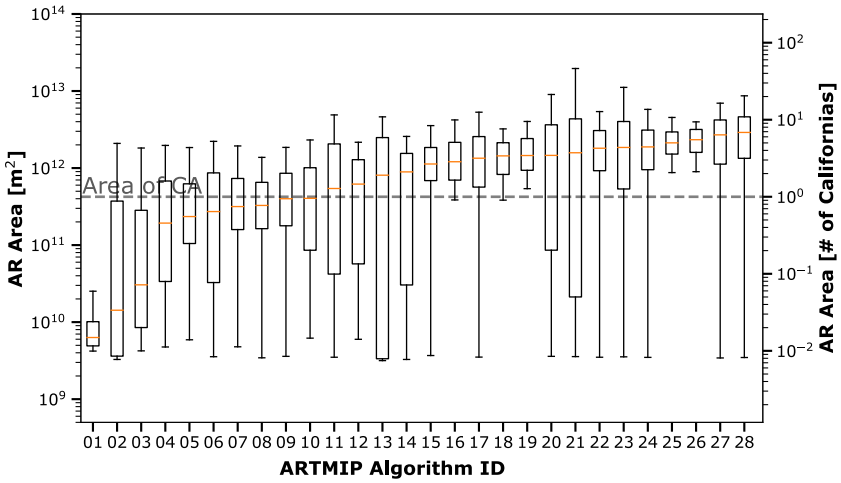

Figure 1.2: AR area calculated from different methods in ARTMIP, ordered by median area (01-28). Algorithm names are included in the supporting information in Table A.1 for reference.

transport intensity and landfall duration and show that there are beneficial and hazardous impacts associated with AR events. AR size can impact the area of influence of AR at the time of landfalling. Moreover, if ergodicity relates AR size and duration, AR size could directly relate to its benefits and hazards. Therefore, in addition to integrated vapor transport (IVT) and AR duration, the question "how large are atmospheric rivers?" represents a key aspect of research in the atmospheric river research community. The first two core chapters of this dissertation (Chapters 2 and 3) focus on AR size, its evolution during its lifecycle, and how AR size responds to climate change scenarios.

1.3 Atmospheric Rivers in Lower Latitudes

Due to the significant impact of ARs in midlatitudes hydro-climatology, there is an extensive amount of work and ARs literature in these regions. On the other hand, the occurrence of ARs in low latitudes is less studied within the AR research community. Furthermore, there is not much literature regarding tropical ARs. Lately, they are starting to gain interest within the AR community (De Luna et al., 2020; De Luna, 2021). In Chapter 4, we study the relationship between extreme precipitation during the dry season (November-March) in Central Western Mexico (CWM) and low latitude ARs. This anomalous rainfall during the can

have significant impacts on the regional agricultural production. Different crops like beans, coffee, and corn, are sensitive to changes in the environment, and modifications of climate conditions could affect the productivity and quality of the crops (Cruz López, 2011; Porter and Semenov, 2005). Furthermore, changes in wind speed, direction, and moisture transport could have an impact on the regional weather and the oceanic state. These extreme rainfall events produce increased river discharges associated with changes in chlorophyll concentration, turbidity, temperature, and salinity of coastal ecosystems (Domínguez-Hernández et al., 2020; Romero-Rodríguez et al., 2020). Although there are numerous possible effects related to these anomalous winter precipitation in CWM, there is still a lack of documentation about these events and their impacts. Moreover, no research links these events with ARs. In Chapter 4 we study this relationship and raise the question, what is the state of the atmosphere during these low latitude ARs? How much of the dry season precipitation in CWM is associated with ARs?

1.4 Outline of Dissertation and Main Objectives

This dissertation's core chapters (Chapters 2 through 4) can be divided in two main scopes: AR size estimation and its response to climate change (Chapters 2 and 3), and landfalling ARs in Western Central Mexico and their relationship with the dry season (November-March) extreme precipitation.

In **Chapter 2**, we take a novel approach in AR size estimation. Our research works toward developing and implementing five different AR size estimation methods independent from the ARDTs algorithms. Since we do not develop a new ARDT, and the methods developed in this chapter are not directly related to any existing ARDT, we argue that they collectively provide a robust and objective way to estimate AR size. Our methods provide a lower range of AR sizes than the ARTMIP collection of ARDTs.

We analyze the wet season (November-April) of North American landfalling ARs and create a composite for the 1980-2018 period to objectively estimate the size of ARs using the IVT from ERA5 reanalysis data Copernicus Climate Change Service (2017). We also analyze

the evolution of AR size (width, length, area) and geometry (aspect ratio, angle with respect to the equator) thought the AR lifecycle. All the content in Chapter 2 (with format changes) is published in *Journal of Geophysical Research: Atmospheres* as:

Inda-Díaz, H. A., O'Brien, T. A., Zhou, Y., & Collins, W. D. (2021). Constraining and characterizing the size of atmospheric rivers: A perspective independent from the detection algorithm. *Journal of Geophysical Research: Atmospheres*, 126, e2020JD033746. https://doi.org/10.1029/2020JD033746

In **Chapter 3**, we focus on how the AR size changes between historical and future climate scenarios using the data from the ARTMIP tier 2 experiment and the Coupled Model Intercomparison Project 5 (CMIP 5) and CMIP 6. To do this, we develop and calculate the atmospheric river confidence index (ARCI), a quantity representing the fraction of ARDTs that agree with the presence of an AR in a given grid cell. As a first approach, We use the ARCI to estimate ARs areas. Then, using the AR centroid given by ARCI, we implement and apply three AR size estimation methods from Chapter 2 as part of the Toolkit for Extreme Climate Analysis (TECA)[2]. We study how the background IVT field and the AR size respond to the future climate scenarios: the representative concentration pathway 8.5 (RCP8.5, CMIP5) and shared socioeconomic pathways 5-8.5 experiments (SSP5-8.5, CMIP6).

In **Chapter 4** we explore the association between dry season (November-March) extreme precipitation in Central Western Mexico (CWM) and atmospheric rivers. The study of ARs in lower latitudes is still a new research area, with few works studying tropical ARs. Moreover, a large part of the ARTMIP ARDTs are designed to study ARs in higher latitudes and filter out tropical IVT. We use reanalysis data from the ECMWF Atmospheric Reanalysis of the Twentieth Century ERA-20C[3] to extract IVT and precipitation in the 1900-2010 period, and the Bayesian AR Detector `TECA-BARD v1.0.1`, (O'Brien et al., 2020a) to calculate the probability of AR presence in CWM. In this fashion, we calculate how much of the dry season rainfall in CWM is associated with ARs. Moreover, we calculate composites of the general state of the atmosphere at the time of AR landfall on the coast of CWM.

[2] `https://github.com/lbl-eesa/teca`

[3] `https://www.ecmwf.int/en/forecasts/datasets/reanalysis-datasets/era-20c`

Lastly, in Chapter 5 we present a recapitulation of the main conclusions of this work and the possible future research paths and recommendations.

Chapter 2

Constraining and Characterizing the Size of Atmospheric Rivers: A Perspective Independent From the Detection Algorithm

The full content of this Chapter is published in *Journal of Geophysical Research: Atmospheres* (with some style and journal format modifications) as:

Inda-Díaz, H. A., O'Brien, T. A., Zhou, Y., & Collins, W. D. (2021). Constraining and characterizing the size of atmospheric rivers: A perspective independent from the detection algorithm. *Journal of Geophysical Research: Atmospheres*, 126, e2020JD033746. `https://doi.org/10.1029/2020JD033746`

2.1 Abstract

Atmospheric rivers (ARs) are large and narrow filaments of poleward horizontal water vapor transport. Because of its direct relationship with horizontal vapor transport, extreme precipitation, and overall AR impacts over land, AR size is an important characteristic that needs to be better understood. Current AR detection and tracking algorithms have resulted in large uncertainty in estimating AR sizes, with areas varying over several orders of magnitude among different detection methods. We develop and implement five independent size estimation methods to characterize the size of ARs that make landfall over the west coast of North America in the 1980-2017 period and reduce the range of size estimation from ARTMIP. ARs that originate in the Northwest Pacific (WP) (100°E-180°E) have larger sizes and are more zonally oriented than those from the Northeast Pacific (EP) (180°E-240°E). ARs become smaller through their life cycle, mainly due to reductions in their width. They also become

more meridionally oriented towards the end of their life cycle. Overall, the size estimation methods proposed in this work provide a range of AR areas (between $7x10^{11}m^2$ and 10^{13} m^2) that is several orders of magnitude narrower than current methods estimation. This methodology can provide statistical constraints in size and geometry for the design and tuning of AR detection and tracking algorithms; and an objective insight for future studies about AR size changes under different climate scenarios.

2.2 Introduction

Atmospheric rivers (ARs) are long and narrow filaments of poleward water vapor transport from the tropics (Newell et al., 1992; Zhu and Newell, 1998; Ralph et al., 2018), that carry over 90% of the meridional moisture transport from the tropics to higher latitudes but may occupy only about 10% of the total longitudinal length (Zhu and Newell, 1998). AR have been associated as a main source of precipitation around midlatitude continental regions around the world (Ramos et al., 2015; Neiman et al., 2008; Lavers and Villarini, 2013b; Waliser and Guan, 2017; Viale et al., 2018). ARs are associated with up to half of the extreme events in the top 2% of the precipitation and wind distribution across most mid-latitude regions (Waliser and Guan, 2017). Moreover, landfalling ARs are associated with about 40-75% of extreme wind and precipitation events over 40% of the world's coastlines (Waliser and Guan, 2017). ARs can have both positive and negative effects in continental regions. Their absence can lead to droughts (Dettinger, 2013), whereas numerous ARs can lead to flooding and other hydrological hazards (Ralph et al., 2006; Dettinger, 2011; Ralph and Dettinger, 2011; Lavers and Villarini, 2013a). Ultimately, ARs have important consequences in the hydrological cycle of regions like California. They contribute to the accumulation of the snowpack and the reservoir level and water availability (Dirmeyer and Brubaker, 2007; Guan et al., 2010; Kim et al., 2013; Goldenson et al., 2018; Eldardiry et al., 2019).

Along with horizontal vapor transport, AR size (length and width) is an important characteristic that needs to be better understood. Nevertheless, a robust connection between AR size and their impacts over land and intensity scale still has to be studied and determined.

Ralph et al. (2019a) introduced a scale to categorize AR strength based on vapor transport intensity and landfall duration and show that there are beneficial and hazardous impacts associated with AR events. If ergodicity relates AR size and duration, AR size could be directly related to the benefits and hazards associated with them. Therefore, in addition to integrated vapor transport (IVT) and AR duration, the question "how large are atmospheric rivers?" represents a key aspect of research in the atmospheric river research community.

The Atmospheric River Tracking Method Intercomparison Project (ARTMIP) has made an international effort to understand whether and how our scientific understanding of ARs may depend on the detection algorithm. The different ARTMIP detection and tracking algorithms are designed to answer different questions, and they produce differences in AR climatology (Shields et al., 2018; Rutz et al., 2019; Lora et al., 2020); therefore, there are differences in their detected shape and size. It has become clear that AR detection and tracking are heavily influenced by how researchers have quantitatively defined this phenomenon, for example, the use of 250 kg $m^{-1}s^{-1}$ minimum threshold for IVT, which does not account for size but only for the concentration of flow and moisture levels. These different rules and algorithm thresholds have resulted in large uncertainty in estimating the AR size, with areas varying over several orders of magnitude among different detection methods (see Figure 2.1).

The definition of the boundaries and size quantification of ARs are ongoing research questions, and therefore a great uncertainty among methods is expected. Some recommendations made after the formal AR definition in the Glossary of Meteorology in 2018 were "to keep the definition as short as possible and to leave specifications of how the boundaries of an AR are to be quantified open for future and specialized developments" (Ralph et al., 2018).

The research described in this manuscript works toward the development and implementation of five independent AR size estimation methods. Since we do not develop a new AR detection algorithm, and the methods described here are not directly related to any existing AR detection or tracking algorithm, we argue that they collectively provide a robust and objective way to estimate AR size with a lower range of AR sizes than ARTMIP. The methods presented in this work does not preclude the possibility that the parameter choices are made

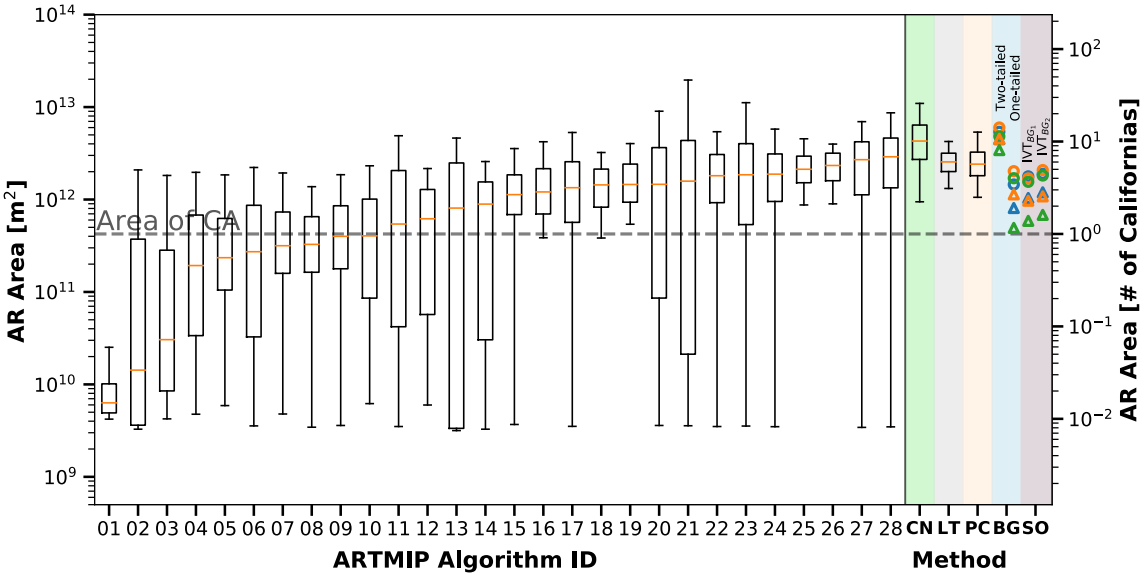

Figure 2.1: White background: AR area calculated from different methods in ARTMIP, ordered by median area (01-28). Colored background: AR area calculated in this work using the ClimateNet ARTMIP campaign (CN), Lagrangian Tracers method (LT), Principal Component Analysis of IVT (PC), KS-test between the IVT of AR and the background IVT field (BG), and the statistical overlapping of the conditional probability distribution of IVT given distance to the center of AR and the background IVT probability density function (SO): see Sections 2.4.1-2.4.4 for details. For BG and SO methods, triangles represent the composite of AR with Northeast Pacific origin (EP) and circles represent the composite of AR with Northwest Pacific origin (WP). Blue, orange, and green markers account for the 25, 50, and 75% of the AR life cycle, respectively. For the BG method, we show the results from the two-tailed and one-tailed KS-test. For the SO method, we show the results using IVT_{BG_1} and IVT_{BG_2}, that correspond to a $p \geq \sigma^+$ at 179.5 and 193.9 kg m^{-1}s^{-1}s, respectively. (Algorithm names are included in the supporting information Table S1 for reference).

by the same group people. Nevertheless, we used statistical quantities to estimate ARs size and objectively tested these methods' sensitivity to the chosen parameters. For this work, we analyze the winter (November-April) North American coast landfalling ARs and create a composite for the 1980-2018 period, to objectively estimate the size of ARs using the IVT from ERA5 reanalysis data (Copernicus Climate Change Service, 2017).

2.3 Data

In this work, we use the AR detection results from three different ARTMIP methods (Shields et al., 2018; Rutz et al., 2019): `CASCADE_BARD_v1` (O'Brien et al., 2020b), `Lora_global` (Lora et al., 2017), and `Mundhenk_v3` (Mundhenk et al., 2016). Employing these three different detection algorithms allows us to broadly sample ARs in the North Pa-

cific Ocean. Each of these methods generates a binary flag: 1 for "AR conditions exist" and 0 for "AR conditions do not exist"; for each latitude-longitude grid point. AR binary flags were calculated using thermodynamic and dynamical fields from the Modern-Era Retrospective Analysis for Research and Applications Version 2 (MERRA-2) reanalysis (Gelaro et al., 2017) as a part of the ARTMIP Tier 1 experiment (Shields et al., 2018). In the methods section, we describe how we use these binary flags to create the AR composite.

The column-integrated water vapor (IWV) and IVT, are the two main variables used to define and characterize ARs (Ralph et al., 2018). For this work, we focus on IVT and calculate it using the vertically integrated eastward and northward water vapor flux $[\dot{q}_x, \dot{q}_y]$ (kg m^{-1}s^{-1}) provided by the ERA5 reanalysis. IVT is defined as

$$\mathrm{IVT} = \sqrt{\dot{q}_x^2 + \dot{q}_y^2}, \tag{2.1}$$

where

$$\dot{q}_x = -\frac{1}{g}\int_{p_b}^{p_t} q\, u\, dp, \tag{2.2}$$

$$\dot{q}_y = -\frac{1}{g}\int_{p_b}^{p_t} q\, v\, dp, \tag{2.3}$$

q is the specific humidity [kg kg^{-1}], u and v the zonal and meridional wind velocity [m s^{-1}] over the pressure surface p, P_b is 1000 hPa, P_t is 200 hPa, and g is the gravitational acceleration. We also use u and v for the Lagrangian in subsection 2.4.3. ERA5 data have a temporal resolution of 1 hour and a horizontal resolution of 0.25 degrees. We focus our work on the 1980-2017 period.

Following (O'Brien et al., 2020b), in order to avoid the large contiguous regions of high IVT near the tropics associated with the intertropical convergence zone (ITCZ), we spatially filter the IVT field as

$$\mathrm{IVT}' = \mathrm{IVT} \cdot (1 - \mathrm{e}^{\frac{-y^2}{2\Delta y^2}}), \tag{2.4}$$

where IVT'(x, y) is the filtered IVT field, x and y are the longitude and latitude, respectively,

and Δy is half-width at half-maximum of the filter. We use $\Delta y = 15°$, which effectively damps the IVT to zero within the ITCZ. Hereon we refer to the filtered field as IVT for simplicity.

This analysis focuses on 37 wet seasons (November-April) in the 1980-2017 period over the North American coast. We focus on landfalling ARs and effectively restrain the study domain to the North Pacific Basin (0°N-90°N, 100°E-240°E).

Furthermore, since this work's primary focus is to study the size of ARs, we only utilize output from the three ARTMIP algorithms to obtain a broad and robust sample of AR occurrences (time and approximate location). With the exception of the areas shown in Figure 2.1, we explicitly avoid using the exact shape or size determined by any detection and tracking algorithm.

2.4 Methods

We apply the AR life cycle tracking algorithm from Zhou et al. (2018) to the AR binary flag data (from the three detection methods used in this work) and record each detected AR position and timestamp. To ensure we sample over the highest possible number of ARs and avoid double-sampling events, we start by taking all the ARs detected from one tracking method. We add the AR events from the second tracking method that are not detected by the first, and finally, we add the ones from the third method that are not in the first or the second. It is essential to note that we only record the AR time stamp and center coordinates of each object through its life cycle (calculated using Equations 2.7 and 2.8), and we do not infer the shape or size of ARs from these detection algorithms. Our size-estimating methods later use the recorded AR center as a first guess on the time and location of an AR.

In this fashion, we create a 1980-2017 wet season (November-April) dataset of North American coast landfalling AR objects. Each object corresponds to one instantaneous snapshot of an AR and contains its center's timestamp and location through its life cycle. The dataset is divided into two parts, based on AR origin location (Northwest Pacific "WP" 100°E-180°E vs. Northeast Pacific "EP" 180°E-240°E); and classified by its life cycle stage, at 25%, 50%, and 75% of the AR total life cycle. All subsequent analyses and methods in this work

are applied separately for each of these six sub-datasets.

2.4.1 Principal Component Analysis of IVT (PC Method)

Recognizing that ARs are associated with ridge-like structures in the IVT field, the principal components (PC) method is designed to estimate AR size by modeling AR shapes as Gaussian. For each object, we apply principal component analysis (PCA) to the high IVT cluster closest to the AR object's center (or first guess) and compute the weighted covariance matrix C_w (Price, 1972) of latitude and longitude

$$C_w = \frac{\Sigma_{i=1}^{\mathrm{nx}}\Sigma_{j=1}^{\mathrm{ny}}\mathrm{IVT}_{ij}(x_{ij}-\overline{x})^T(y_{ij}-\overline{y})}{\Sigma_{i=1}^{\mathrm{nx}}\Sigma_{j=1}^{\mathrm{ny}}\mathrm{IVT}_{ij}}, \tag{2.5}$$

where x_{ij} and y_{ij} are the longitude and latitude of the ERA5 grid, $\overline{x}, \overline{y}$ are the spatial zonal and meridional mean, and the weight is given by the IVT_{ij} at each grid point. C_w is a 2x2 matrix, such that

$$C_w \begin{pmatrix} \vec{s_0} \\ \vec{s_1} \end{pmatrix} = \begin{pmatrix} \lambda_0\, \vec{s_0} \\ \lambda_1\, \vec{s_1} \end{pmatrix}, \tag{2.6}$$

where the eigenvectors $\vec{s_0}$,$\vec{s_1}$ are the principal components of the IVT field, and λ_0,λ_1 are the eigenvalues. The principal components represent the directions of maximum variance of the IVT field near the AR. The largest eigenvalue represents the direction that explains the largest IVT variance, hence the longest AR axis (along the AR, $\vec{s_0}$), while the smallest would represent the shortest AR axis (across the AR, $\vec{s_1}$).

To filter the IVT field that is far from one AR object, we use a 2-step iterative method. First, we find the IVT cluster closest to the first guess location and define the AR "core" as the points where IVT is greater than 0.5 times the local maximum IVT. We apply PCA to the AR core and use the eigenvalues and eigenvectors to create a 2D Gaussian function using Equation (2.11). Then, we filter all the points from the original ERA5 IVT field where the core Gaussian function is less than 10^{-3} (we found this value worked well for the ARs objects analyzed in this work). We then apply PCA to the filtered IVT field and use the results to

estimate the size of the AR object.

We define the length (width) of the AR as twice the magnitude of $\vec{s}_0$ ($\vec{s}_1$), and its area as the ellipse whose axes are the principal components $\vec{s}_0$ and $\vec{s}_1$ (white solid lines and ellipse in Figure 3.1). The AR orientation θ is defined as the angle between $\vec{s}_1$ and the equator. Estimating the area of an AR as an ellipse is an idealization that allows us to simplify the problem and avoid the introduction of more rules and thresholds that would essentially result in a new detection algorithm. We realize that this will affect the calculation of areas with more highly irregular AR shapes. However, in a case-by-case inspection, we find that this is a good approximation for the average AR in this work. Moreover, an overlap plot of all the AR events (Figure 2.8) shows that, on average, this is an adequate idealized model representation of ARs, which becomes particularly relevant for the statistical methods described in section 2.4.2. We utilize `fastKDE` (O'Brien et al., 2014, 2016) to calculate probability density functions (PDF) of length, width, area, and orientation, using all the AR objects in our six sub-datasets (`https://github.com/LBL-EESA/fastkde/releases/tag/v1.0.18`). The method described in this section –applying PCA to the IVT field and define length and width– is labeled PC throughout this work.

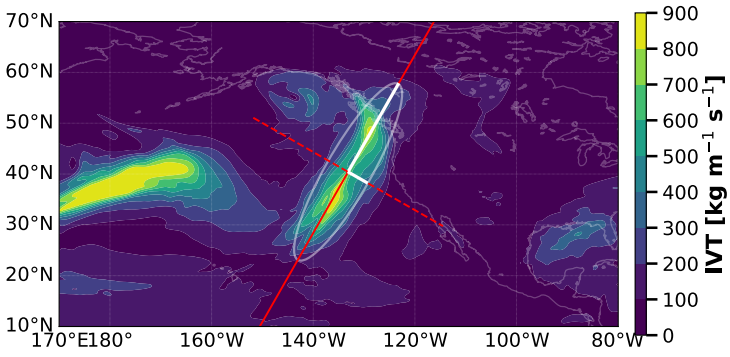

Figure 2.2: Principal component analysis method. White lines represent the PC of the AR, and the white contour is the area estimated from the ellipse whose axes are the PC. The red lines represent directions along and across AR used to sample IVT for SO and BG methods (dashed/solid represent the first/second PC).

2.4.2 Estimating AR Size from Composites and Background IVT Field (BG and SO Methods)

To estimate the AR length and width, we use two different statistical methods for determining the distance at which the AR composite becomes indistinguishable from the background IVT field (from now on referred only as background for simplicity). We create an AR composite from a total of 1,150 (980) AR objects for the WP (EP) in the 1980-2017 wet seasons. We randomly sub-sample 300 AR objects (from each region) to ensure independence between each AR object used to create the composite and increase the statistical robustness of these methods.

The statistical overlapping method (SO) looks at the overlapping between the background PDF and the composite as a function of the distance to the AR center. On the other hand, the background method (BG) uses a Kolmogorov–Smirnov test (KS-test) to look at the difference between the background cumulative distribution function (CDF) and the conditional probability distribution (CPD) of the composite IVT given the distance to the AR center. We describe both methods in §2.4.2 and §2.4.2. For the SO and BG methods, we calculate the AR composite area by modeling the shape of ARs as ellipses, whose axes are the length and width calculated by each method.

We define the AR center coordinates $(\overline{x}, \overline{y})$ for every AR object within the composite as the IVT-weighted center of mass:

$$\overline{x} = \frac{\Sigma_{i=1}^{nx}\Sigma_{j=1}^{ny}\mathrm{IVT}_{ij}x_{ij}}{\Sigma_{i=1}^{nx}\Sigma_{j=1}^{ny}\mathrm{IVT}_{ij}}, \tag{2.7}$$

$$\overline{y} = \frac{\Sigma_{i=1}^{nx}\Sigma_{j=1}^{ny}\mathrm{IVT}_{ij}y_{ij}}{\Sigma_{i=1}^{nx}\Sigma_{j=1}^{ny}\mathrm{IVT}_{ij}}. \tag{2.8}$$

We then sample IVT along the direction of the principal components (see Section 2.4.1) through all the domain (represented by the red lines in Figure 3.1), and calculate the distance

d of each point along this line to the AR center

$$d = ||(x', y') - (\overline{x}, \overline{y})||, \tag{2.9}$$

where (x', y') represent the coordinates of the points along each of the principal components' direction. In this fashion, we create a joint distribution of IVT and d for the AR composite, and utilize `fastKDE` to calculate the CPD of IVT given d: $P(\text{IVT} \mid d)$.

Estimation of the Background

We estimate the PDF and CDF of the background by randomly sampling IVT from ERA5 reanalysis data through the North Pacific Ocean in the period of study. Since the definition of 'background' is somewhat ambiguous, we calculate two separate backgrounds: IVT_{bk_1}, where the grid cells inside an AR are masked at the time of sampling (AR grid cells not used to calculate the background); and IVT_{bk_2}, where ARs are not masked at the time of IVT sampling. Despite the fact that IVT_{bk_2} includes high-IVT points inside some ARs, we remark that both backgrounds are statistically indistinguishable with a confidence level of 95% according to a two-sample KS-test. The CDF of the background is higher than 0.84 ($p \geq \sigma^+$, where σ^+ is the value of CDF at +1 standard deviation) at 179.5 kg $\text{m}^{-1}\text{s}^{-1}s$ and 193.9 kg $\text{m}^{-1}\text{s}^{-1}s$ for IVT_{bk_1} and IVT_{bk_2} respectively, which are later used for the SO and BG methods (§2.4.2 and §2.4.2) and referred to in the text label in Figure 2.1.

Statistical Overlapping of IVT With the Background Field PDF (SO)

One way to estimate the AR composite's length and width is by looking at the overlap of the background PDF and the composite IVT conditional probability distribution given the distance to the center of AR (CPD(d)). We define the statistical boundary of the AR composite as the distance where the CPD(d)=0.16 contour is greater or equal to background IVT value at CDF=0.16. In other words, where CPD(d) at -1 standard deviation (σ^1) intersects with the background PDF at +1 standard deviation (σ^+) (where the lower boundary of the shading contour intersects the dotted line in Figure 2.4). With this method, we determine the

AR extent by determining the distance d where the overlap between the composite PDF and the background PDF is less than two standard deviations. This method is referred to as SO throughout this work.

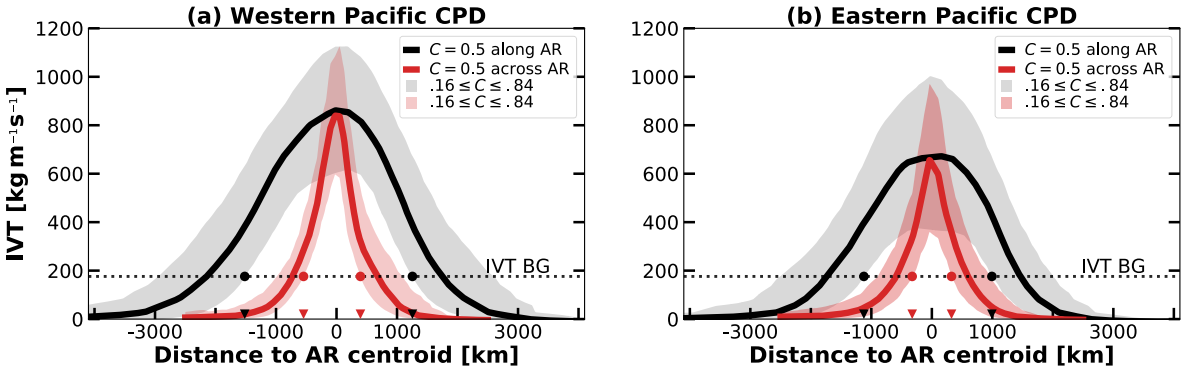

Figure 2.3: Conditional probability distribution of IVT given the distance to the center of the AR. Red colors represent the transverse direction (across AR), black colors represent the longitudinal direction (along AR). The 0.5 conditional probability C is represented in solid thick lines. The shading corresponds to probabilities between 0.16 and 0.84. According to the statistical overlapping method, the AR is delimited by those distances where the dashed line (background IVT $p \geq 0.84$) intersects the 0.16 CPD contour (marked in red and black dots). For example, for the Northwest Pacific composite (WP) in panel (a), these intersections occur at approximately from -1,500 and 1,200 km along the AR, and -600 and 400 km across the AR. The triangles mark these distances of overlapping with the background.

K-S Statistics Between AR Composite and the Background CDF (BG)

The KS-test is used to determine at which distance the CDF of the composite IVT is indistinguishable from the background CDF. This method assumes that the IVT distribution within ARs differs from the background.

From the CPD(d), we calculate the CDF of the composite IVT at different distances along and across the AR composite (CDF(d)). We compare the CDF(d) against the background CDF (2.4) and apply two-tailed and one-tailed KS-tests (KS1 and KS2, respectively). For the KS1, we define the AR boundaries at the distance where the background CDF is significantly lower than the background at the 95% confidence level. For the KS2, the AR boundaries are delimited by those distances at which the KS-statistic reaches a minimum value, *i.e.* where the CDF(d) and the background CDF are most similar. Figure 2.4 shows how the CDF(d) (colored dashed lines) converges to the background CDF (solid black line) far from the center

of the AR composite ($d = 0$ km, represented by the most transparent dashed lines). Both

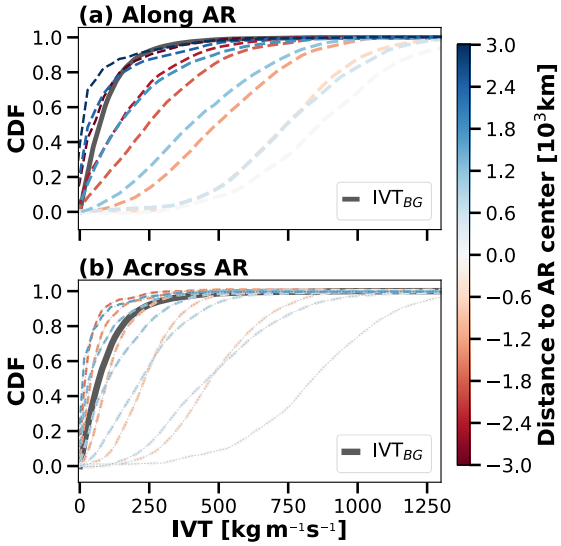

Figure 2.4: Colored lines show the CDF of IVT for the AR composite, at different distances from the AR center (CDF(d)); less transparent dashed lines represent a farther distance to the AR center. The black solid line shows the CDF of the background. The KS-test evaluates where the composite IVT and the background are statistically indistinguishable (for the two-tailed test) or where the composite IVT CDF is statistically lower than the background CDF (for the one-tailed test).

BG and SO methods provide a robust statistical estimation of the AR composite size. In the supporting information, we show a test of the sensitivity of the SO method to changes in the background PDF and to changes in the CPD(d) overlapping values; we also test the sensitivity of the BG method to changes in the statistical level of significance for the one-tailed BG method (Text S1 and Figures S1(a-b)).

2.4.3 Lagrangian Tracers for Area Estimation (LT)

Previous work by (Garaboa-Paz et al., 2015) suggests that ARs relate to attracting Lagrangian Coherent Structures (LCS) in the 2D and 3D flow fields. With this in mind, we hypothesize that Lagrangian tracers can be used to estimate AR area from a fluid dynamics point of view. The association of ARs with LCS implies that tracers inside the AR are more likely to preserve spatial coherence through backward and forward trajectory integration. Furthermore, tracers near the boundaries and outside of the AR, compared with those inside the

AR, would be more likely to disperse and end up at a final location farther from its initial location.

To do so, we use a 2D passive Lagrangian tracer advection model. Tracers are advected over pressure surfaces using 2D velocity fields from ERA5 reanalysis following a stochastic advection equation

$$dx_i = (u_i + \sqrt{2}\overline{u}_i\, w_i)dt, \tag{2.10}$$

where i represents the zonal or meridional directions, u the 2D velocity over pressure surfaces, $\overline{u}_i$ is the root mean square of the local velocity near the tracer (Sawford, 1991; Griffa et al., 1995; Rodean, 1996; LaCasce, 2008), and w_i is a random perturbation with zero mean and unit variance (i.e., a Wiener process). This random nudging in the tracer position at each step helps represent diffusion, turbulence, and other processes not resolved by the model. In the supporting information Text S2 and Figure S2, we show a test of the sensitivity of AR area to changes of the scaling velocity $\sqrt{2\overline{u}_i}$. We solve Equation (2.10) using the Euler method with a time-step of 1 hour (same as the ERA5 resolution, thus avoiding the need for time interpolation). The model uses bilinear interpolation in space to estimate the velocity at the tracer location.

We select the tracers' initial positions in the vicinity of a given AR by randomly selecting 2000 points from the entire study domain (-80S to 80N, 180W to 180E), with a probability given by a 2D Gaussian function centered in the AR

$$g(x, y) = \exp(-(a(x - \overline{x})^2 + 2b(x - \overline{x})(y - \overline{y}) + c(y - \overline{y})^2)), \tag{2.11}$$

where

$$a = \frac{\cos^2(\theta)}{2\lambda_0^2} + \frac{\sin^2(\theta)}{2\lambda_1^2}, \tag{2.12}$$

$$b = \frac{\sin(2\theta)}{4\lambda_0^2} - \frac{\sin(2\theta)}{4\lambda_1^2}, \tag{2.13}$$

$$c = \frac{\sin^2(\theta)}{2\lambda_0^2} + \frac{\cos^2(\theta)}{2\lambda_1^2}, \tag{2.14}$$

λ_0 and λ_1 are the eigenvalues of the covariance matrix in Equation (2.5), $\overline{x}$ and $\overline{y}$ are the longitude and latitude of the AR center, and θ is the angle between the along the AR axis ($\vec{s_1}$ from Equation (2.5)) and the equator. We observe that for fewer than 500 tracers, the AR area might not be correctly resolved since, for larger ARs, there might be regions inside the AR without initial tracers. We find that, in general, 2,000 is a sufficient number of initial tracers and allows a spatial distribution that concentrates in the vicinity of the IVT blob and extends further from it. Our results do not vary for larger number of tracers. In this fashion, we ensure that the initial position of tracers is distributed inside and outside of the AR, but no tracers (or a negligible number) are far from the AR (the tracers initial position distribution is represented by the black dots in Figure 2.5 (a)). Additionally, we simulate 50 tracers for each initial position, resulting in 50 different trajectories due to the random term in Equation (2.10). This is equivalent to repeating the experiment 50 times, thus increasing the statistical robustness of the results. We find similar results using a higher number of repetitions.

The area estimation is done as follows. Starting from the initial position (black dots), we compute trace trajectories five days backward in time (resulting in the orange dots in Figure 2.5 (a)). We then use these new locations to calculate the forward in time five days trajectory (resulting in the blue dots in Figure 2.5 (a)). We compute this process for all pressure levels between the surface and 500 hPa and record the tracers' final position at each level. We choose five days because we need a timescale longer than the boundary layer and convective timescales, and we want a timescale as long as possible without exceeding the Rossby timescale by too much. Moreover, other works have found that few ARs have a longer duration than five days (Payne and Magnusdottir, 2016; Zhou et al., 2018).

We gather the final tracers from all levels and calculate the bivariate PDF of the final tracer latitudes and longitudes. We estimate the AR area as the size of the largest contiguous contour of PDF=0.68 (the PDF of the final position within two standard deviations), corresponding to the thicker green contour if Figure 2.5 (b). In the Appendix A we present a sensitivity test of AR area relative to PDF value changes.

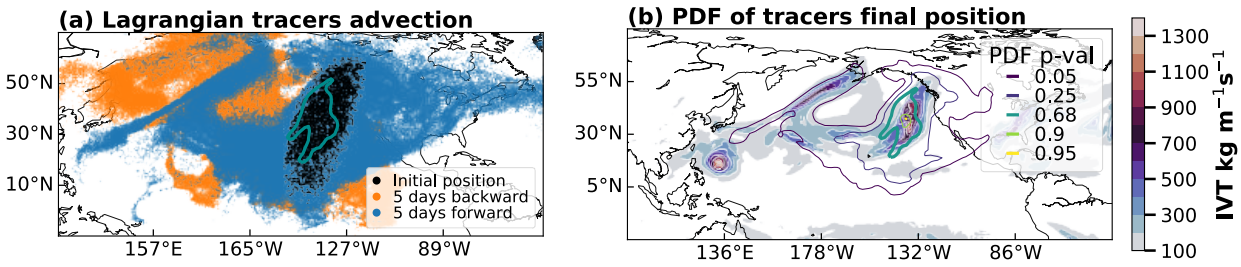

Figure 2.5: (a) Initial position (black), after five days backward advection (orange), and five days forward advection from the orange tracer locations (blue).The cyan contour shows the region with most (68%) of the tracers after the the five-day forward advection. (b) IVT (filled contours) and PDF of the tracers' final position (contours). Thicker cyan contour at $p = 0.68$ area is used to estimate the AR size in the Lagrangian tracers method (LT).

2.4.4 ClimateNet Method (CN)

We use *ClimateNet* Climate Contours (`https://www.nersc.gov/research-and-development/data-analytics/big-data-center/climatenet/`, `http://labelmegold.services.nersc.gov/climatecontours_gold/tool.html`), which is a guided user interface for annotating climate events, facilitating the collection of hand-labeled weather datasets (Prabhat et al., 2021).

We use the data generated using the ClimateNet labeling tool during the 3rd ARTMIP workshop (`http://www.cgd.ucar.edu/projects/artmip/meetings.html`) in October 2019. Half a day out of a 2.5-day workshop was devoted to this task, including over 15 workshop participants who labeled 660 time slices of data during the session (O'Brien et al., 2020a). A total of 1822 AR detections were made over the whole globe, and 378 were made in the North Pacific Ocean region (which will be referred to as global and NP, respectively) using an Atmospheric Model Intercomparison Project (AMIP) simulation performed with the Community Atmosphere Model (version 5) running at 25-km resolution (Wehner et al., 2014). We calculate the area and orientation of each of these hand-labeled ARs. Unlike the methods described in Sections 2.4.1-2.4.3, this method does not distinguish between the AR-genesis location or life cycle.

2.4.5 AR Size Calculation Methods Summary

To help the reader keep track of the various methods used in this work, Table 2.1 summarizes a description for each method and the short names used throughout this work.

Table 2.1: Methods for AR size estimation used in this work.

Acronym	Description	Section
PC	Principal components analysis of atmospheric river integrated vapor transport field.	§2.4.1
SO	Statistical overlapping of AR composite conditional probability distribution of IVT given the distance to the AR center and the PDF of the background IVT field.	§2.4.2
BG	Comparison of the IVT CDF of AR composite with the CDF of the background IVT field.	§2.4.2
LT	PDF of Lagrangian tracers final position near an AR after backward and forward 5 days advection.	§2.4.3
CN	Hand-labeled ARs using CLIMANET contours labeling tool by a group of experts at the 2019 ARTMIP workshop.	§2.4.4

A deeper insight into the design of the PC, SO, and BG methods is shown in Sections A.1 and A.2.

2.5 Results

We focus on the size of North American landfalling ARs. Our results are consistent among methods: with AR areas within the 10^{11} to 10^{12} m^2 range in four of the five methods: PC, LT, BG, and SO; and between 10^{11} to 10^{13} m^2 for CN. Our results have a narrower range of AR area than the ARTMIP ensemble (Figure 2.1), with order-of-magnitude consistency with the majority of the algorithms used in ARTMIP. The novel statistical methods in this study (PC, SO, BG, and LT) are in good agreement with the manually labeled AR sizes from the ClimateNet method. Table 2.2 contains a summary of the length, width, and area for all four methods, depending on the AR genesis location and life cycle. Figure 2.8 shows a visual representation of the size results for PC, LT, BG, and SO methods for WP and WP at 50%

life cycle.

2.5.1 AR Length and Width

Figure 2.6 (a-c) shows the PDF of length and width calculated by PC. The PDF exhibits the typical "long and narrow" AR shape, from 2.3 to 4.5 times longer than the width (Table 2.3). According to PC, ARs have a median width of 844 km (90% of the cases were between 520 and 1386 km), and length of 3842 km (90% between 2495 and 5816 km) for the AR with WP origin; and median width of 814 km (90% of the cases were between 6477 and 1476 km), and length of 3413 km (90% between 2321 and 5400 km) for the ARs with EP Origin.

According to PC, WP has larger and wider ARs than EP. The differences in length are statistically significant at a 99% confidence level, however differences in width are not. Concerning the life cycle, the WP composite has the smallest AR size at 25% and the largest at 50% of its life cycle, nevertheless only the differences in length are statistically significant. The EP composite length does not change much through the life cycle. However, the width decreases monotonically through its life cycle, with differences statistically significant at a 99% confidence level.

Consistently with PC, BG, and SO methods show larger ARs originating in the WP. According to BG, the ARs composite length (width) at 50% life cycle is 4019 (1121) km for the WP and 3275 (501) km for the EP. The SO's composite length (width) at 50% life cycle is 2751 (916) km for the WP and 2107 (646) km for the EP. It is possible that the EP and WP ARs' size differences might come from the landfall condition and that focusing on landfall means that we are preferentially looking at that type of AR, since this work is focused specifically on landfalling ARs. The difference in size between WP and EP ARs and of non-land-falling ARs could be explored in future work.

The lengths determined by the BG and SO methods exhibit little variation throughout the life cycle. In contrast, AR width decreased by a factor of 0.67 (WP) and 0.60 (WP) for BG, and 0.85 (WP) 0.69 (EP) for SO. These results suggest that the AR area difference

through the life cycle is mainly due to changes in width.

2.5.2 AR Area

Figure 2.6 (d-e) show the PDFs of the AR area, calculated by PC method (solid lines) and LT (dashed lines). For the WP ARs, the area has a median of $2.47\text{x}10^{12}\text{m}^2$ and $2.75\text{x}10^{12}\text{m}^2$ for PC and LT, respectively. For the EP ARs, the area has a median of $2.23\text{x}10^{12}\text{m}^2$ and $2.33\text{x}10^{12}\text{m}^2$ for PC and LT, respectively. The WP composite has larger areas than the EP at a 99% confidence level. EP ARs do not show a significant difference in the area through the life cycle, while WP ARs attain maximum area at their mid-life cycle for both the PC and LT methods.

The one-tailed KS-test (one-tailed BG) estimates the AR composite area as $3.67\text{x}10^{12}\text{m}^2$ and $1.40\text{x}10^{12}\text{m}^2$ for WP and EP, respectively (at 50% life cycle). SO estimates a composite area of $1.75\text{x}10^{12}\text{m}^2$ and $8.74\text{x}10^{11}\text{m}^2$ for WP and EP, respectively (at 50% life cycle), with more extensive (both width and length) AR from WP when compared with the EP AR.

BG results show a decrease the AR composite area decreases through the life cycle by a factor of 0.68 and 0.54 for the WP and EP, respectively (decrease of $\sim$0.83 and $\sim$0.62 according to SO). These changes come mainly from differences in width.

CN results show a median area of $3.34\text{x}10^{12}\text{m}^2$ (90% of data between $6.15\text{x}10^{11}$ and $7.70\text{x}10^{12}\text{m}^2$) in the North Pacific region. Figure 2.7(a) shows larger AR areas for the global analysis $4.29\text{x}10^{12}\text{m}^2$ (90% of data between $9.43\text{x}10^{11}$ and $1.09\text{x}10^{13}\text{m}^2$). All the other methods (PC, LT, BG, and SO) are consistent with the CN area result, which are in fact hand-labeled AR by experts, demonstrating that these methods give reasonable estimates for AR size. If so, our results using ClimateNet might be on the larger side in terms of AR area, which could be related to the specific shapes the user can determine, or where the user exactly locates the AR "boundary" polygon at the time of labeling, however, these details are outside of the scope of this study.

The sensitivity tests presented in Section A.3 show that for the SO method, variations in the overlapping background PDF and composite CPD values from (PDF, CPD)=(0.05,0.95)

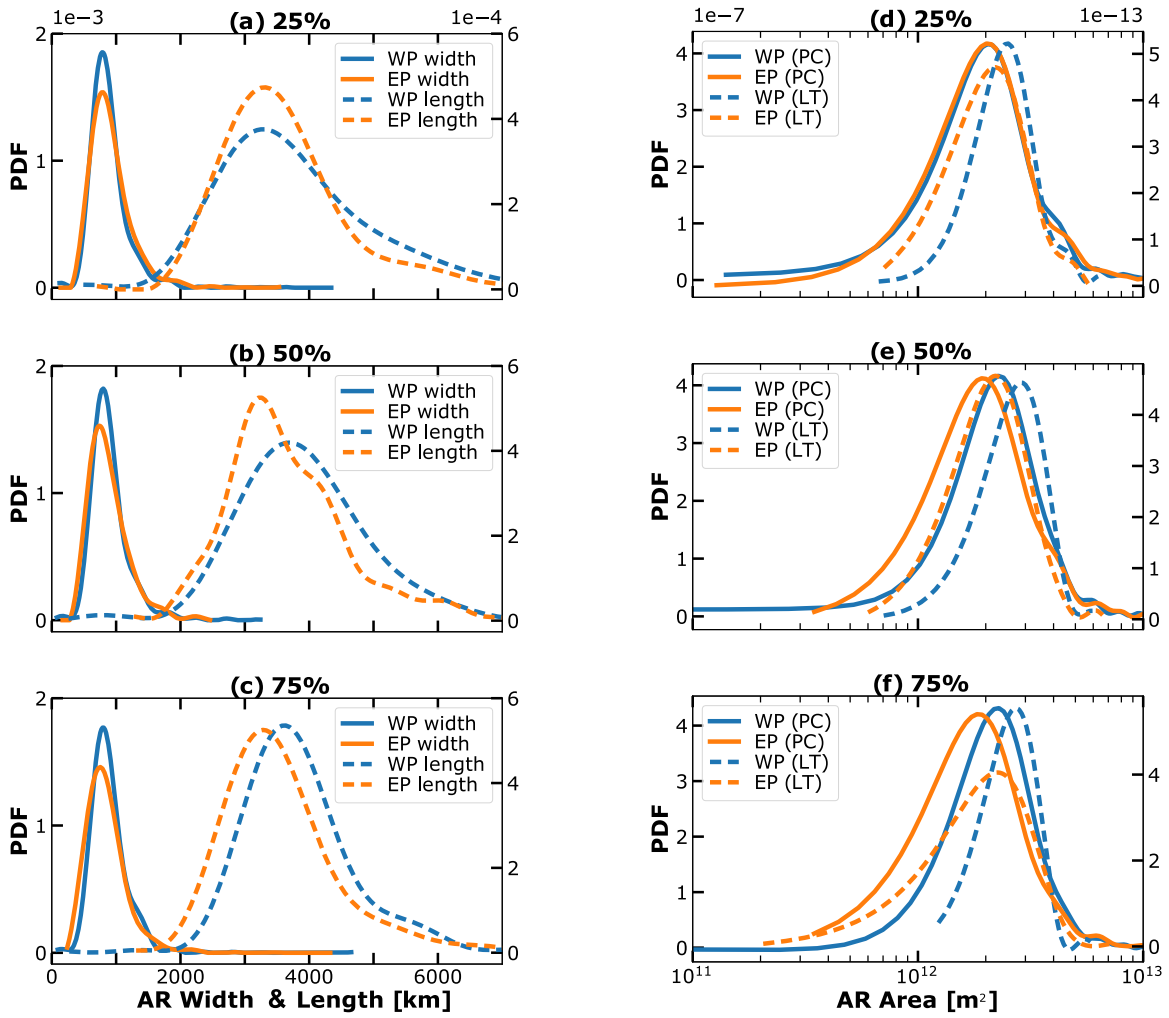

Figure 2.6: (a-c) PDF of AR length (dashed lines) and width (solid lines) using the principal components method (PC), at 25, 50, and 75% of the AR life cycle. WP composite in blue lines, EP composite in orange lines. (d-f) PDF of AR area for the PC method in solid lines, and the LT method in dashed lines. Lines colors are the same as in (a-c).

(minimum overlapping) to (PDF, CPD)=(0.5,0.5) (large overlapping) result in area changes from 2.84x10^{11} to 9.97^{12} m^2. The one-tailed BG sensitivity test to the significance level ($p = 0.8$ to $p = 0.99$) shows a change in AR area from 2.26^{12} to 1.48^{12} m^2. For BG and SO, AR length shows more sensitivity to variations in the parameters than width.

The LT sensitivity test shows that using 0.68 as the PDF contour to define AR size, variations in the scaling velocity (from 0.125 times to 4 times $\sqrt{\overline{u}}$) result in an area changes from 1.53^{12} to 4.16^{12} m^2. Variations in the PDF value used (ranging from 0.4 to 0.93) result in area changes between one and two orders of magnitude (Section A.3). All the sensitivity

analysis described here are computed for the WP at 50% life cycle. We find similar results for different stages of the life cycle and for EP.

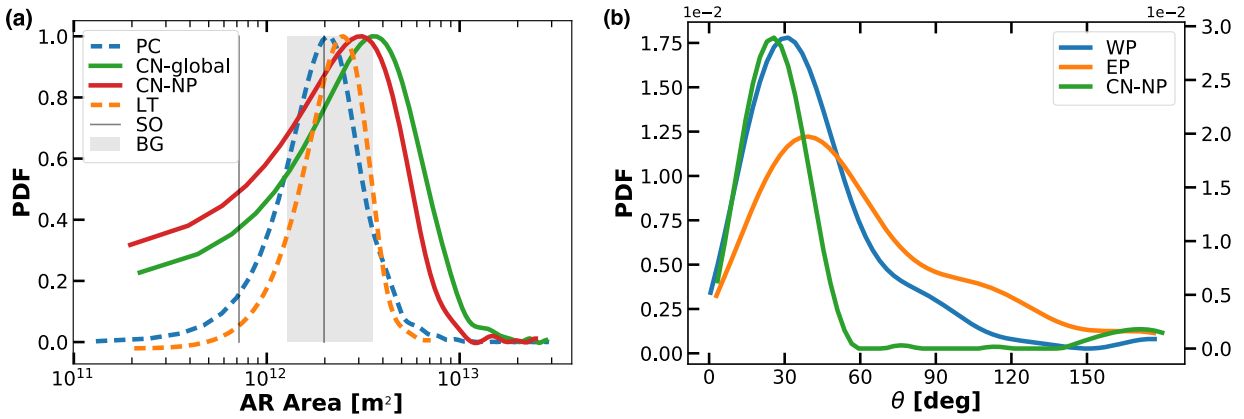

Figure 2.7: (a) PDFs of AR area (PDFs are not normalized for visualization). PDFs from the PC and LT methods are calculated using data from WP and EP at 50% life cycle. The lowest to highest obtained values from the BG (SO) methods are represented in the shaded gray area (between solid gray lines) for comparison. (b) PDF of AR orientation with respect to the equator from the PC method at 50% of the AR life cycle for the WP (blue line), EP (orange line), and the North Pacific ClimateNet (green line) composites.

2.5.3 AR Orientation

Figure 2.7(b) shows the PDF of the AR orientation with respect to the equator θ, calculated using PC and CN methods. PC method results show that ARs originating in the WP are more zonally orientated than those originating in the EP. WP ARs have a median θ of 13.7° (with 90% of the data between 7.7° and 99.8°). EP ARs have a median θ of 49.1° (with 90% of the data between 10.4° and 142.6°). CN results show a median θ of 26.5° (with 90% of the data between 6.9° and 157.2°) for the North Pacific AR.

With respect to the AR life cycle, both WP and EP show an increase in the median θ: 28° to 37° for the WP, and 46° to 53° for the EP. Table 2.2 summarizes the results of length, width, and area of the AR composite from all the methods in this work. AR geometrical characteristics (aspect ratio and orientation) are summarized in Table 2.3.

2.6 Discussion and Conclusions

Figure 2.8 (color contours) shows the superimposition of IVT from all the AR objects in this study for WP and EP at 50% AR life cycle. We present Figure 2.8 as a summary of the PC, SO, BG, and LT methods. We aim to illustrate the methods together and make them more clear to the reader. To generate this plot, we rotated all the AR objects to the same frame of reference. The angle of orientation θ of each AR represents the median angle with respect to the equator, and the dotted angle is the -1 and +1 standard deviations of θ. EP ARs are not only more zonally oriented, but they also have greater variance in θ than WP ARs. The dashed gray lines represent the 5th, 50th, and 95th percentile of the PC method. The golden and red bars represent the SO and BG length and width. The solid cyan line represents the LT method and was created by rotating the final position of all tracers to the same system of reference of the plot and then calculating the bivariate PDF (cyan contour corresponds to p=0.68). We can see that BG, SO, PC and LT are very consistent in estimating the AR width. On the other hand, AR length seems to have more variability among methods (in Appendix A, we show that AR length shows to be more sensitive than width to parameter variations). The results from LT show an asymmetric contour with an elongated tail to the southwest end of the AR. They suggest that an AR detection algorithm based on "fluid dynamics" could be helpful to determine the AR boundaries independently of thresholds or parameter choices and other variables such as IVT. This is worthy of exploring in future works.

In previous works, two main areas of AR-genesis have been identified: over the subtropical Northwest Pacific and the Northeast Pacific (Sellars et al., 2017; Zhou et al., 2018). Here, we find robust evidence of a statistically significant difference in size of landfalling ARs, depending on their region of genesis, with longer and broader ARs from the Northwest Pacific relative to those originating over the Northeast Pacific. This result may be related to the dynamical process driving the AR formation. It has previously been suggested that WP ARs have a stronger association with a thermally driven jet over the North Pacific Ocean; while EP ARs are thought to be more associated with extratropical cyclone activity and to the commonly

Table 2.2: Summary of AR size statistics by method.

	Northwest Pacific			Northeast Pacific		
	0.25	**0.5**	**0.75**	**0.25**	**0.5**	**0.75**
Method	**Length** [km]					
PC	3553	3842	3757	3366	3413	3425
5-95%	2168-5984	2495-5816	2608-5562	2239-5596	2321-5454	2315-5400
BG	2783	2932	2813	2431	1640	1764
SO	2422	2650	2532	1986	1944	1580
Method	**Width** [km]					
PC	823	844	838	845	814	809
5-95%	520-1386	530-1405	510-1366	513-1550	477-1476	454-1516
BG	664	912	769	465	882	355
SO	850	812	771	625	582	394
Method	**Area** [10^{12} m^2]					
PC	2.32	2.60	2.49	2.26	2.24	2.19
5-95%	1.02-5.29	1.23-5.22	1.26-4.98	1.03-5.30	1.03-5.09	0.97-5.22
LT	2.55	2.91	2.74	2.35	2.34	2.32
5-95%	1.52-4.54	1.49-4.47	1.59-3.88	1.26-4.32	1.25-3.97	1.09-4.01
BG	1.45	2.10	1.70	0.88	1.13	0.49
SO	1.61	1.69	1.53	0.97	0.89	0.48
CN	3.34					
5-95%	0.61-7.70					

known phenomenon "Pineapple Express" (Li and Wettstein, 2012; Cordeira et al., 2013; Zhang et al., 2019a; Zhou and Kim, 2019; Zhang and Ralph, 2021). We also found evidence WP ARs tend to have more zonal orientation than those originating in the EP, which we believe could also relate to the dynamical feature driving the AR. This difference in AR size and orientation between the EP and WP may have implications for where moisture transport occurs.

PC, BG, and SO methods agree on the typical "long and narrow" shape from the AR literature, with a median aspect ratio of approximately 4 (length/width). Other detection algorithms could use these findings as geometrical constraints in the future. The AR orientation difference between WP and EP could also directly affect the precipitation associated with landfalling AR, depending on the relative angle to the coastal mountain range, and hence the orographic lifting (Hu et al., 2017). More meridionally oriented AR towards the end of

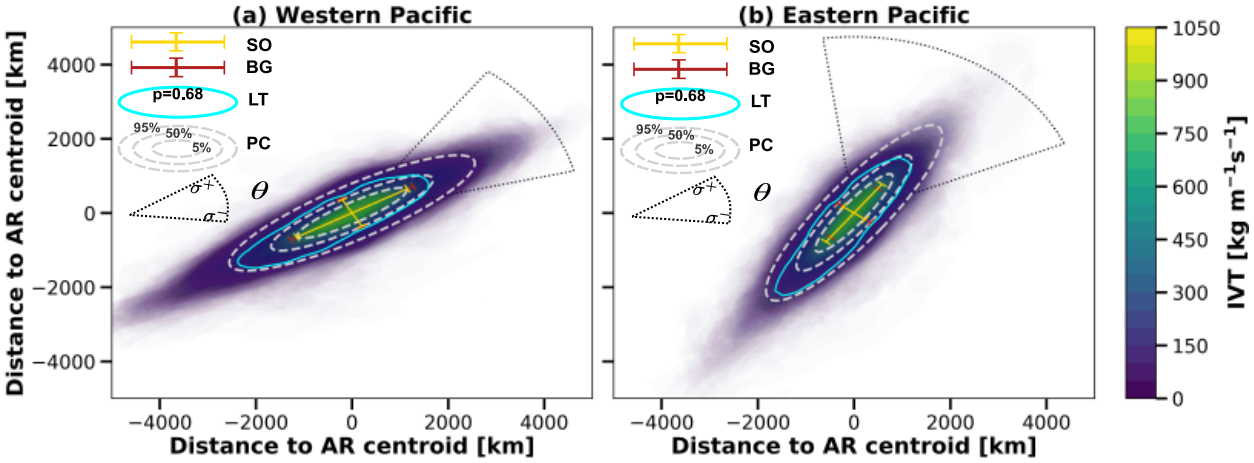

Figure 2.8: Summary of results and graphical comparison for the different size estimation methods. In color contours we superimpose (with transparency of 0.1%) the IVT field of all the AR objects available at 50% life cycle for (a) Western Pacific and (b) Eastern Pacific. Each AR object is rotated to the median angle of orientation, and the distance to the center is calculated to make this plot. The dotted "fan" represents two standard deviations for the AR orientation with respect to the equator. The red and gold lines represent the length and width estimated using the SO and BG methods respectively. gray dashed lines, represent the results of the PC method for the 5th, 50th and 95th percentile. The cyan solid line represents the results of the LT method. It is the 0.68 probability contour of the final position for all the AR cases gathered and rotated to the same frame of reference.

the life cycle might modify the effects of orographic lifting and AR impacts over the coast. Furthermore, the steepening of the AR orientation with life cycle supports the hypothesis that most–if not all–ARs are intrinsically related to midlatitude cyclones. During the growth phase of the AR, the AR would form along the southern portion of a midlatitude cyclone, in the location of the dominant moisture source; the predominantly westerly flow would cause developing ARs to have a more zonal orientation. As the AR matures and its moisture is entrained into the cyclone, more of the vapor transport would occur along the eastern flank of the cyclone, giving the AR a steeper, more meridional orientation. If there is a relationship between size, duration, propagation speeds, and orientation, this could influence the AR landfalling conditions and its impacts, which is a question worthy of further investigation.

It is worth noting that the AR width at the end of life cycle (75%) obtained from SO and BG, (355 and 394 km respectively) is in good agreement with airborne and satellite observations from the 1997/1998 winter ARs, where they find an average width scale based in IWV of 417.3 km (Ralph et al., 2004). Moreover, our result on orientation of EP ARs at the end of the life cycle (53.6°) agrees with the 17-case composite observation from dropsondes, where

Table 2.3: Summary of AR geometry statistics by method.

	Northwest Pacific			**Northeast Pacific**		
	0.25	**0.5**	**0.75**	**0.25**	**0.5**	**0.75**
Method	**Aspect ratio** [width/length]					
PC	4.2	4.5	4.4	3.9	4.2	4.3
5-95%	2.3-7.6	2.3-7.7	2.6-7.3	2.3-7.1	2.3-7.4	2.4-7.5
BG	4.1	3.2	3.6	5.2	1.8	4.9
SO	2.8	3.2	3.2	3.1	3.3	4.0
Method	**Orientation** [deg]					
PC	28.9	29.5	35.7	49.9	53.1	53.6
5-95%	8.1-80.2	7.3-89.2	8.5-111.8	9.5-136.5	12.3-130.1	12.1-149.6
CN	26.5					
5-95%	6.9-157.2					

(Ralph et al., 2004) find an average wind direction of the low-level jet of 216.7° (corresponding to 53.3° from our methodology's frame of reference).

We also observe a monotonic decrease in AR width through the life cycle, which could be associated with a systematic loss of moisture, or it could be associated with frontogenesis and sharpening of the frontal zone. These results could be explored in future studies, especially ones using a tracer technique.

The sensitivity tests suggest that for the statistical size estimation methods (SO and BG), length is more sensitive to the choice of parameters than width. We hypothesize that this is related to the difficulty of statistically distinguishing the AR "tail" (or southwest end or AR) from the high water vapor and IVT in the vicinity of the ITCZ. We observe (in a case by case exploration) that sometimes the IVT field does not have a clear boundary with respect to the ITCZ, resulting in a noisier CPD in the left side of the AR composite for large probability contours ($C > 0.9$). It is possible that this would also have an impact in the detection and tracking algorithms and their ability to objectively determine the AR boundary.

Furthermore, this raises the question about a possible link between AR size and duration, and how the size of AR might be directly related to hydrological impacts over landfalling regions. Do we need to explicitly include size in addition to IVT intensity and duration in the categorization scale for AR (Ralph et al., 2019a) and their impacts? We often assume

ergodicity, but if larger ARs have systematically slower/faster propagation speeds, then the AR size-life cycle (and possibly landfalling duration) relationship would not be ergodic. Our future research will work toward answering these questions.

In Figure 2.1, we can observe a high spread in the size of AR among AR detection methods (white background part). Our results show values with much less spread (colored background part) relative to the current methods. It is important to notice that some of these conclusions could be reached by analysis of existing ARTMIP data, with the caveat that such conclusions would depend on the heuristic AR detection algorithms employed in ARTMIP. The novel analytical contributions introduced in this manuscript –use of PCA of the IVT field, statistical estimation of AR composite size (BG and SO methods), and the use of Lagrangian tracers to determine AR size– allow us to reach these conclusions and can provide a statistical constraint on AR size for other detection methods. This could also allow us to incorporate size into the ARs categorization in coastal regions and their impacts.

We speculate that different algorithms within ARTMIP detect different parts of the AR since each algorithm defines different rules and relatively-unconstrained thresholds, as it has been shown before by Lora et al. (2020). For example, since algorithms 01 to 04 are outside the range of areas estimated in this study, we can confidently argue that these algorithms are not detecting the same part of ARs as our methods or as algorithms 11-28. The AR research community may need to define more than one term, with different definitions depending on what particular meteorological feature of AR is being studied. We acknowledge that different algorithms are created with different objectives and study goals in mind. However, future studies could benefit from the definition of three potential new terms: "AR core" (algorithms 1-4), "dynamical envelope" (LT method and maybe 9-17 methods), and "thermodynamic envelope" (PC, BG, SO, CN and algorithms 18-28). Although the dynamical and thermodynamical envelopes are indistinguishable here, they may not be in studies of future AR size. This could help understanding what is the extent of the consistency in AR detection among different algorithms, particularly with respect to size. The importance of changes in AR statistics in the future has been demonstrated before. Previous studies have shown that

AR frequency will increase by ∼50% globally, AR intensity will increase by ∼25%, and that the ARs will be ∼25% longer and ∼25% wider (Espinoza et al., 2018; Massoud et al., 2019). In future simulations using CMIP5/CMIP6 models, AR detection algorithms project a global increase in AR frequency and sizes, specially along the western coastlines of the Pacific and Atlantic oceans, and it has been demonstrated that the choice of the detection algorithm can have a major impact on the results of the climate change AR studies (O'Brien et al., 2021).

We will continue to examine the relation between AR size and duration. Moreover, the direct relationship we found between AR origin location and size, the life cycle and size, motivates us to apply our methodology to understand how the AR size would change under global warming scenarios. Current detection methods may require adjusting the parameters and thresholds when studying different climate scenarios, making the objective study of change in AR size a challenging problem for future projections. Our approach could provide an objective insight for future works into the possible changes and hydrological impacts due to AR size and climate change.

Acknowledgements

This research was supported by the Director, Office of Science, Office of Biological and Environmental Research of the U.S. Department of Energy Regional and Global Modeling and Analysis (RGMA) and used resources of the National Energy Research Scientific Computing Center (NERSC), also supported by the Office of Science of the U.S. Department of Energy under Contract No. DE-AC02-05CH11231.

We would like to acknowledge the Research Data Archive (RDA), managed by the Data Engineering and Curation Section (DECS) of the Computational and Information Systems Laboratory (CISL) at the National Center for Atmospheric Research for providing the ERA5 dataset at `https://rda.ucar.edu/datasets/ds633.0/`. ERA5 is publicly available at the Copernicus Climate Change Service (C3S) Climate Data Store (CDS) - `https://cds.climate.copernicus.eu/cdsapp#!/dataset/reanalysis-era5-pressure-levels?tab=form`.

We would like to acknowledge the ClimateNet team who facilitated the labeling tool

and data for the ARTMIP workshop AR labeling campaign, in alphabetical order: Karthik Kashinath, Sol Kim, Jiayi Chen, and Kevin Yang.

We would like to acknowledge participants in the ARTMIP workshop ClimateNet AR labeling campaign, in alphabetical order: Alan Rhoades, Allison Michaelis, Ashley Payne, Brian Kawzenuk, Eric Shearer, Huanping Huang, Jonathan Rutz, Paul Ullrich, Sol Kim, Swen Brands, Yang Zhou, and Zhenhai Zhang.

Chapter 3

Change in Size of Atmospheric Rivers Under Future Climate Scenarios

Abstract

There has been a growing interest in atmospheric rivers research over the last few decades. It has been observed that AR detectors (ARDTs) are heavily influenced by how researchers quantitatively define this phenomenon. In particular, AR size depends highly on the numerical definition of AR embedded in the design of ARDTs, producing significant uncertainty in the AR size estimation. We use data from the ARTMIP Tier 2 CMIP5/6 experiment to calculate the AR confidence index and create global composites of AR objects. Then, we estimate the AR composite size using four independent methods to understand how AR size responds to future simulations with strong radiative forcing (CMIP5: RCP-8.5, CMIP6: SSP-858).

Our results show an increase in the background IVT field between 10% and 21% from historical to future simulations, with a broader inter-model variability of $\sim$27%. The mean AR area is 3.15x10^6 ($\pm$0.83x10^6 km^2) and 3.42x10^6 km^2 ($\pm$0.70x10^6 km^2) for historical and future runs, respectively. We find that AR width is more sensitive than AR length and contributes more to the change in the AR area. Increases in AR size dominate across models and methods. However, the methods that compare to the background IVT show both positive and negative changes in AR size. Regardless of the sign in AR size difference, the mean AR cross-section water vapor transport increases between 8% and 37%. We also find that North American landfalling ARs are more likely to penetrate further inland for future simulations.

We provide an objective insight into the change in AR size with climate change from an independent perspective of the ARDTs design and algorithms, which could help as a reference for tuning and constraining existing ARDTs or designing new AR detection algorithms.

3.1 Introduction

Over the last few decades, there has been an increased interest in the study of atmospheric rivers (ARs). They were first described by Newell and Zhu (1994) as high tropospheric water vapor flux with a filamentary structure or "tropospheric rivers". The definition of ARs is still a topic of research and debate. In 2018 a definition was submitted to the AMS Glossary[1]: "A long, narrow, and transient corridor of strong horizontal water vapor transport that is typically associated with a low-level jet stream ahead of the cold front of an extratropical cyclone. The water vapor in atmospheric rivers is supplied by tropical and/or extratropical moisture sources. Atmospheric rivers frequently lead to heavy precipitation where they are forced upward—for example, by mountains or by an ascent in the warm conveyor belt. Horizontal water vapor transport in the midlatitudes occurs primarily in atmospheric rivers and is focused in the lower troposphere. Atmospheric rivers are the largest 'rivers' of fresh water on Earth, transporting on average more than double the flow of the Amazon River" (Ralph et al., 2019a).

AR carry over 90% of moisture from the tropics to higher latitudes (Zhu and Newell, 1998), but cover only between 2 and 10 percent of the earth's surface (O'Brien et al., 2021). Midlatitude continental regions around the world have large amounts of precipitation associated with ARs Ramos et al. (2015); Neiman et al. (2008); Lavers and Villarini (2013b); Waliser and Guan (2017); Viale et al. (2018); Neiman et al. (2002); Ralph et al. (2004, 2005); Leung and Qian (2009); Guan et al. (2010); Warner et al. (2012); Neiman et al. (2013); Ralph et al. (2013); Rutz et al. (2014); Huang et al. (2021); Viale and Nuñez (2011); Gimeno et al. (2016); Blamey et al. (2018); Ramos et al. (2019). ARs can lead to hydrological hazards, and a better understanding of AR can help in the study, forecasting, and communication of flooding (Lavers et al., 2016b,a; Ralph et al., 2019b, 2006; Dettinger, 2011; Ralph and Dettinger, 2011; Lavers and Villarini, 2013a). Moreover, ARs have significant consequences on the hydrological cycle of regions like California and contribute to the accumulation of the snowpack and the reservoir level, and water availability Dirmeyer and Brubaker (2007); Guan et al. (2010);

[1] https://glossary.ametsoc.org/wiki/Atmospheric_river

Kim et al. (2013); Goldenson et al. (2018); Eldardiry et al. (2019); Dettinger et al. (2011); Gershunov et al. (2017).

Detecting and defining the boundaries of AR is a particularly complicated task. The Atmospheric River Tracking Method Intercomparison Project (ARTMIP) is an international effort to understand and quantify uncertainties in atmospheric river science based on the choice of detection/tracking methodology. ARTMIP has (at the time of writing this dissertation) 30 different algorithms or atmospheric river detectors (ARDTs). Different ARTMIP detection and tracking algorithms are designed to answer different scientific questions, and they are heavily influenced by how researchers quantitatively define this phenomenon. As a consequence, it has been observed that they can reproduce differences in AR climatology (Shields et al., 2018; Rutz et al., 2019; Lora et al., 2020). In particular, Inda-Díaz et al. (2021) shows that the quantification of AR size has a significant uncertainty and variability among different ARDTs, with areas varying over several orders of magnitude among different detection methods.

Different studies have analyzed the AR changes in future simulations, with a general agreement that global increases in atmospheric moisture will increase the intensity of ARs (Payne et al., 2020). Aquaplanet simulations with increasing sea surface temperature (SST) show that AR integrated water vapor (IWV) is especially sensitive to SST, with Increases of 6.3–9.7% per degree warming. IWV transport by ARs increases relatively uniformly with temperature and at consistently lower rates than IWV, as modulated by systematically decreasing low-level wind speeds (McClenny et al., 2020). Lavers et al. (2015) found that multimodel mean integrated vapor transport (IVT) increases by 30–40% in the North Pacific and North Atlantic storm tracks, mainly due to higher atmospheric water vapor content. Future climate change AR studies also show differences in AR-related precipitation and hydrological cycle (Gao et al., 2016; Rhoades et al., 2021; Gershunov et al., 2019). O'Brien et al. (2021) show that most ARDTs project a global increase in AR frequency, count, and sizes, especially along the western coastlines of the Pacific and Atlantic oceans, and that the choice of ARDTs is the dominant contributor to the uncertainty in projected AR frequency when compared with

model choice.

Despite the intrinsic differences and the main objectives researchers have in mind when developing ARDTs, there is an important degree of overlapping between ARDTs (Lora et al., 2020; Payne et al., 2020). Inda-Díaz et al. (2021) show that the quantification of AR size has a large uncertainty associated with the ARDTs and their numerical definition of AR, which could affect our understanding of AR size change in future climates. This uncertainty motivates this work, in which we aim to study the changes in AR size under future climate scenarios from a perspective independent of the ARDTs. Following the methodology of Inda-Díaz et al. (2021), we define and calculate the atmospheric river confidence index (ARCI), and use it along three statistical methods from Chapter 2 to estimate the AR size in data from the Coupled Model Intercomparison Project 5 (CMIP 5) (Taylor et al., 2012) and CMIP 6 (Eyring et al., 2016; O'Neill et al., 2016) (referred as CMIP5/6 hereafter).

3.2 Data and Methods

We use data from the ARTMIP Tier 2 CMIP5/6 experiment. This dataset was generated using the outputs from general circulation models associated with the six members from CMIP5 (CCSM4, CSIRO-Mk3-6, CanESM2, IPSL-CM5A-LR, IPSL-CM5B-L, and NorESM1-M) and three members from CMIP6 (BCC-CSM2-MR, PSL-CM6A-LR, MRI-ESM2-0). The model selection was based on data available on the native model vertical grid to reduce the error in calculating the vertical integrals in IVT and IWV and reduce the differences in AR detection over continental regions, where levels below ground are present in isobaric coordinates. Table 3.1 summarizes the models used in the ARTMIP Tier 2 CMIP5/6 experiment.

CMIP5/6 specific humidity q and horizontal wind velocity $\vec{u} = (u, v)$ at 6-hourly intervals are used, with a horizontal resolution varying across models between ∼100km to ∼300 km. The historical runs (his) span over the 1950-2005 (CMIP5) and 1950-2011 (CMIP6) periods. The future runs (fut) span over the 2006-2100 (CMIP5) and 2015-2100 (CMIP6), for which we use the representative concentration pathway 8.5 (RCP8.5, CMIP5) and the shared socioeconomic

Table 3.1: Details of CMIP5/6 models used in the Tier 2 experiment.

Models			
MIP Era	Model Name	Institution	∼Res. [km]
CMIP5	CCSM4	NCAR	120
CMIP5	CSIRO-Mk3-6	CSIRO	207
CMIP5	CanESM2	CCCMA	310
CMIP5	IPSL-CM5A-LR	IPSL	296
CMIP5	IPSL-CM5B-LR	IPSL	296
CMIP5	NorESM1-M	NCC	242
CMIP6	BCC-CSM2-MR	BCC	124
CMIP6	IPSL-CM6A-LR	IPSL	198
CMIP6	MRI-ESM2-0	MRI	124

pathways 5-8.5 experiments (SSP5-8.5, CMIP6).

Vertically integrated water vapor transport (IVT) and vertically integrated water vapor (IWV) are calculated from CMIP5/6 models as:

$$\text{IWV} = -\frac{1}{g}\sum_{k=1}^{N} q_k \Delta p_k \tag{3.1}$$

$$\overrightarrow{\text{IVT}} = -\frac{1}{g}\langle \sum_{k=1}^{N} u_k q_k \Delta p_k, \sum_{k=1}^{N} v_k q_k \Delta p_k \rangle, \tag{3.2}$$

where index k corresponds to model levels going from the surface ($k = 1$) to the top of the model atmosphere ($k = N$), and Δp_k is the difference in level pressures, estimated at level k. IVT is the magnitude of the vapor transport flux vector: $\text{IVT} = \left|\overrightarrow{\text{IVT}}\right|$. More details on the Tier 2 experiment design and the CMIP5/6 data used are described by O'Brien et al. (2021).

We use AR detection data from the six global ARDTs in ARTMIP Tier 2 experiment: `ARCONNECT_v2` (Shearer et al., 2020), `Guan_Waliser_v2` (Guan and Waliser, 2015; Guan et al., 2018), `Lora_v2` (Lora et al., 2017; Skinner et al., 2020), `Mundhenk_v3` (Mundhenk et al., 2016),and `TECA-BARD v1.0.1` (O'Brien et al., 2020b), and `Tempest` (Ullrich and Zarzycki, 2017; McClenny et al., 2020). These six ARDTs are applied to the common CMIP5/6 dataset of IWV and IVT to produce a binary flag that determines whether an AR is present or not present in each grid cell for every time in the study period. Table B.1 summarizes the ARDTs

used in this work, their contributors, and main references. Section B.1.2 briefly describes the classification of these ARDTs based on their treatment of thresholds to detect ARs.

3.2.1 Atmospheric River Confidence Index and AR Tracking

We define and calculate the atmospheric river confidence index (ARCI) as the average of the ARDTs binary detection. We calculate ARCI from the six global ARDTs in Tier 2 experiment. An ARCI=0 means that no ARDT detected an AR, whereas an ARCI=1 means all six algorithms agree on the presence of an AR in a specific grid cell. ARCI gives of a degree of agreement in AR detection between different methods. In this work we use it estimate the presence of ARs in a general area (ARCI Tracking), as well as the first size estimation method (object in the field with ARCI$\pm$2/3). This is described below.

We use the object-based tracking algorithm developed by Zhou et al. (2018) to the track objects with ARCI$\geq$2/3 in the CMIP5/6 dataset (which can also be thought as AR objects). This methodology defines the AR object as enclosed two-dimensional (longitude and latitude) instantaneous area of ARCI$\geq$2/3. The algorithm utilizes the spatial connection between AR objects of consecutive time steps and defines an AR event in three dimensions (longitude, latitude, and time) as a series of spatiotemporally connected AR objects. At the same time, the AR life cycle represents the spatiotemporal evolution of AR objects within an AR event, which allows us to track and study an AR object throughout its life cycle.

We do not directly use the data from the ARDTs to estimate the AR size or shape, instead we use ARCI as an approximation of the general location of AR objects in the field. In this fashion, we reduce the variability in detection between ARTMIP members and study only cases with a high consensus amongh ARDTs.

We define the AR object centroid as the coordinates $(\overline{x}, \overline{y})$ for every AR object as the

ARCI-weighted center of mass:

$$\overline{x} = \frac{\Sigma_{i=1}^{nx}\Sigma_{j=1}^{ny}\mathrm{IVT}_{ij}x_{ij}}{\Sigma_{i=1}^{nx}\Sigma_{j=1}^{ny}\mathrm{ARCI}_{ij}}, \tag{3.3}$$

$$\overline{y} = \frac{\Sigma_{i=1}^{nx}\Sigma_{j=1}^{ny}\mathrm{IVT}_{ij}y_{ij}}{\Sigma_{i=1}^{nx}\Sigma_{j=1}^{ny}\mathrm{ARCI}_{ij}}. \tag{3.4}$$

It is important to notice that for the three size estimation methods from Inda-Díaz et al. (2021) used in this work (Sections 3.2.2 through 3.2.7), we do not use any information on shape or size form the ARDT or ARCI. Instead, we will only use centroid location given by Equations (3.3) and (3.4). We save and use this location as the first guess for the presence of an AR in its vicinity. In order to maintain our analysis independent from the detection methods, shape, size, and other quantities that could be inferred from the ARDTs are not used.

3.2.2 Composite of AR Objects

To study the different characteristics of AR size depending of the life cycle of each AR object, we organize our analysis in two different ways:

- *Mean* composite: all AR objects gathered together (no matter at which life cycle stage they are). We acknowledge that ARs with longer life spans will contribute more to this composite. However, since we want an estimation of the mean AR objects size, this is the way we want to sample.

- *Life cycle* composite: AR objects are composited in different sub-classifications, depending on what part of their life cycle their are at the moment.

We define the AR event life cycle as the total number of time steps that an AR object exists (*i.e.* the duration of the AR event) N. Furthermore, we define the life cycle stage as the ratio of a given time step n in the AR event life cycle to the total duration N:

$$\mathrm{LC} = N/n. \tag{3.5}$$

The ARCI tracking of CMIP5/6 data produces $\sim$3x10^5 (CMIP5) and $\sim$6x10^5 (CMIP6) AR objects with a detection index greater than 2/3 (more or less, depending on the model). Additionally, we organize the AR composites by CMIP5/6 model, and CMIP era (historical *vs* future).

3.2.3 AR Size Estimation

In this work, we estimate the AR size using four different methods: size of objects with ARCI$\geq$2/3, and three methods developed in Chapter 2 (Inda-Díaz et al., 2021): the principal component analysis of IVT, statistical overlapping, and the Kolmogorov–Smirnov test of the AR field with the background IVT (BG). The principal characteristic of these methods is that they are developed independently from the ARDTs' rules and algorithms.

3.2.4 Estimation of AR Size from the Atmospheric River Confidence Index

To estimate the composite AR size from such a large data set as CMIP5/6 is, we take advantage of the Toolkit for Extreme Climate Analysis TECA[2]. TECA is a framework for facilitating parallel analysis of petabyte-scale datasets, and provides generic modular components that implement parallel execution patterns and scalable I/O. These components can easily be composed into analysis pipelines that run efficiently at scale at high-performance computing (HPC) centers (O'Brien et al., 2020b). TECA has the capability to calculate the area of contiguous grid cells with a variable above a certain threshold (blob or patches). Using this capability, we calculate the area of all the AR objects with ARCI$\geq$2/3 in the CMIP5/6 dataset (historical and future simulations). We can interpret this as the mean AR size from the ARTMIP algorithms with a high detection confidence index. More technical details about the implementation and workflow of TECA can be found in O'Brien et al. (2020b) and `https://github.com/lbl-eesa/teca`. For simplicity, this size estimation method will be hereafter referred to as ARCI through this work.

[2] `https://github.com/lbl-eesa/teca`

Principal Component Analysis of the IVT Field (PC)

Following the methodology from Inda-Díaz et al. (2021) (Chapter 2), we apply principal component analysis of the AR composite's IVT field. To do this, we apply a filter to the original CMIP5/6 IVT field to avoid the large contiguous regions of high IVT near the tropics, associated with the intertropical convergence zone (ITCZ):

$$\mathrm{IVT}' = \mathrm{IVT} \cdot \left[1 - \exp\left(\frac{-y^2}{2\Delta y^2}\right)\right], \tag{3.6}$$

$$\tag{3.7}$$

where IVT' is the ITCZ filtered IVT field, x and y are the longitude and latitude, respectively, Δy is half-width at half-maximum of the filter. We use $\Delta y = 15°$, which effectively damps the IVT to zero within the ITCZ (O'Brien et al., 2020b).

The first step in the PC method is to obtain a "first guess" of the location of an AR object. This is provided by the centroid position from the tracking of AR objects (Equations (3.3) and (3.4)). Once we have an approximation of the position of an AR, we filter out the IVT far field from the AR object using a three step iterative method (described in detail in Section A.1). The PC method recognizes that ARs are associated with ridge-like structures in the IVT field. We apply principal component analysis (PCA) to the IVT field and compute the weighted covariance matrix C_w (Price, 1972) of latitude and longitude

$$C_w = \frac{\Sigma_{i=1}^{\mathrm{nx}}\Sigma_{j=1}^{\mathrm{ny}}\mathrm{IVT}_{ij}(x_{ij} - x_0)^T(y_{ij} - y_0)}{\Sigma_{i=1}^{\mathrm{nx}}\Sigma_{j=1}^{\mathrm{ny}}\mathrm{IVT}_{ij}}, \tag{3.8}$$

where x_{ij} and y_{ij} are the longitude and latitude of each CMIP5/6 model grid, and the weight is given by the IVT_{ij} at each grid point. C_w is a 2x2 matrix, such that

$$C_w \begin{pmatrix} \vec{s}_0 \\ \vec{s}_1 \end{pmatrix} = \begin{pmatrix} \lambda_0\,\vec{s}_0 \\ \lambda_1\,\vec{s}_1 \end{pmatrix}, \tag{3.9}$$

where the eigenvectors $\vec{s}_0$,$\vec{s}_1$ are the principal components of the IVT field, and λ_0,λ_1 are

the eigenvalues of the covariance matrix given by Equation (3.9). The principal components represent the directions of maximum variance of the IVT. The largest eigenvalue represents the direction that explains the largest variance, hence the longest AR axis (along AR, $\vec{s}_0$). In contrast, the smallest eigenvector represent the shortest AR axis (across AR, $\vec{s}_1$). We define the AR object length and width as twice the magnitude of $\vec{s}_0$ ($\vec{s}_1$), and its area as the ellipse whose axes are the principal components $\vec{s}_0$ and $\vec{s}_1$ (white solid lines and ellipse in Figure 3.1).

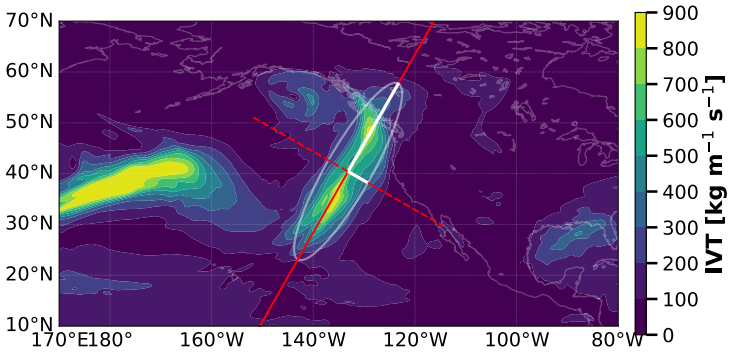

Figure 3.1: Principal component analysis method. White lines represent the PC of the AR, and the white contour is the area estimated from the ellipse whose axes are the PC. The red lines represent directions along and across AR used to sample IVT for SO and BG methods (dashed/solid represent the first/second PC).

3.2.5 Definition of the Background IVT Field

The statistical AR size estimation methods BG and SO compare the AR composite with the background IVT field. Defining this field is not a trivial task. In this work we estimate the background field for each of the CMIP5/6 models using the following methodology.

From every time step in the full period of study, we randomly choose 1000 points from the model domain with ARCI$<$ 2/3, repeating this for the historical and future simulations (each model and era will have their own background IVT field). This allows us to reduce the probability of sampling from inside ARs (also, this effectively reduces the chances to sample IVT from inside ITCZ). A sample number of n=1000 for every time step represents between $\sim$1% and $\sim$13% of the grid points (depending on the model horizontal resolution), and ensures a total sample number N sufficiently large to calculate a smooth probability density

function (PDF) of background IVT field (N$\sim$1.5x10^6 for a single year of data). Sampling with $n > 1000$ produces IVT background fields that are statistically indistinguishable with respect to the $n = 1000$ field, according to a two-tailed Kolmogorov–Smirnov (KS) test, with a confidence level of 99%. Throughout this work, we calculate and use the IVT value at which the background PDF is at +1 standard deviation ($\text{IVT}_{\sigma^{+1}}$) as a proxy for the changes in background IVT, defined in Equation (3.11).

$$F_X(x) = \text{P}(X < x), \tag{3.10}$$

$$\text{IVT}_{\sigma^{+1}} = x \mid \text{P}(IVT < x) = 0.84, \tag{3.11}$$

where $F_X(x)$ is the cumulative distribution function of the background IVT field, and $\text{IVT}_{\sigma^{+1}}$ is such that the probability of the IVT background field is less or equal to $\text{IVT}_{\sigma^{+1}}$ is 0.84.

As we previously discussed in Section 3.2.1, we do not use the ARDTs directly to estimate AR size but only to calculate ARCI. Nevertheless, we can notice some similes between or size estimation methods and the classification of ARDTs regarding their treatment of thresholds (absolute, relative, and fixed relative). This classification is made following the definition of O'Brien et al. (2021), and is explained briefly in Appendix B Section B.1.2. We will explain further this similarities in Section 3.2.7.

3.2.6 Statistical Estimation of AR Size (SO and BG Methods)

SO and BG methods compare the AR composites' with the background IVT field. To do this, we sample the original IVT field from CMIP5/6 data in the directions of the principal components $\vec{s}_0$,$\vec{s}_1$ (this corresponds to the red lines in Figure 3.1). In this fashion, we generate a collection of sampled IVT values and their respective distance to the AR object centroid. Figure3.2(a) shows an example of all the raw IVT sampled for one of the CMIP5/6 model/era case (orange points represent IVT sampled across the AR object and blue points along the AR object). We utilize `fastKDE`[3] (O'Brien et al., 2014, 2016) to calculate the conditional

[3] `https://github.com/LBL-EESA/fastkde/releases/tag/v1.0.18`

probability distribution (CPD) of IVT with respect to the distance to the AR centroid. Figure 3.2(b) shows the CPD of the sampled points from Figure 3.2(a), where the colored contours represent CPD along the AR objects, and the dashed white contours are the 0.16, 0.50 and 0.84 CPD across the ARs composite.

Statistical Overlapping of AR Composite IVT with the Background Field (SO)

SO method defines the statistical boundary of the AR composite as the distance at which the background IVT probability density function (PDF) at $\text{IVT}_{\sigma^{+1}}$ (illustrated by the dotted line in Figure 3.2(b)) intersects the AR composite's CPD at minus one standard deviation σ^{-1} (CPD=0.16) (illustrated by the orange contour in 3.2(b)). Conceptually, this can be interpreted as the distance at which the background $\text{IVT}_{\sigma^{+1}}$ overlaps with the AR composite CPD=0.16. Figure 3.2(c) illustrates this idea, the blue dashed line represents the background PDF, and the orange contour represents the composite's CPD=0.16 contour (obtained from the CPD in Figure 3.2(b). It is important to notice that Figure 3.2(c) is an sketched illustration of the conceptualization of the SO method, which is why the background PDF does not have units.

KS-test Between AR Composite's IVT and the Background Field (BG)

In the BG method, we use a two-tailed KS-test to compare the AR composite's cumulative density function (CDF) to the with the background CDF, for different distances from the AR centroid. CDF of the IVT composite is obtained sampling from the CPD in the IVT dimension at specific distances (illustrated by the dashed vertical line in Figure 3.2(b)). BG is based on the hypothesis that near the AR centroid, the composite's CDF is very different from the background (circle markers in 3.2(d)). Furthermore, the composite's CDF must become more similar to the background CDF as we move away from the AR centroid (triangle markers in 3.2(d)). The KS-test allows us to statistically determine the distance at which the background CDF becomes indistinguishable from the composite's CDF, with a 99% confidence level.

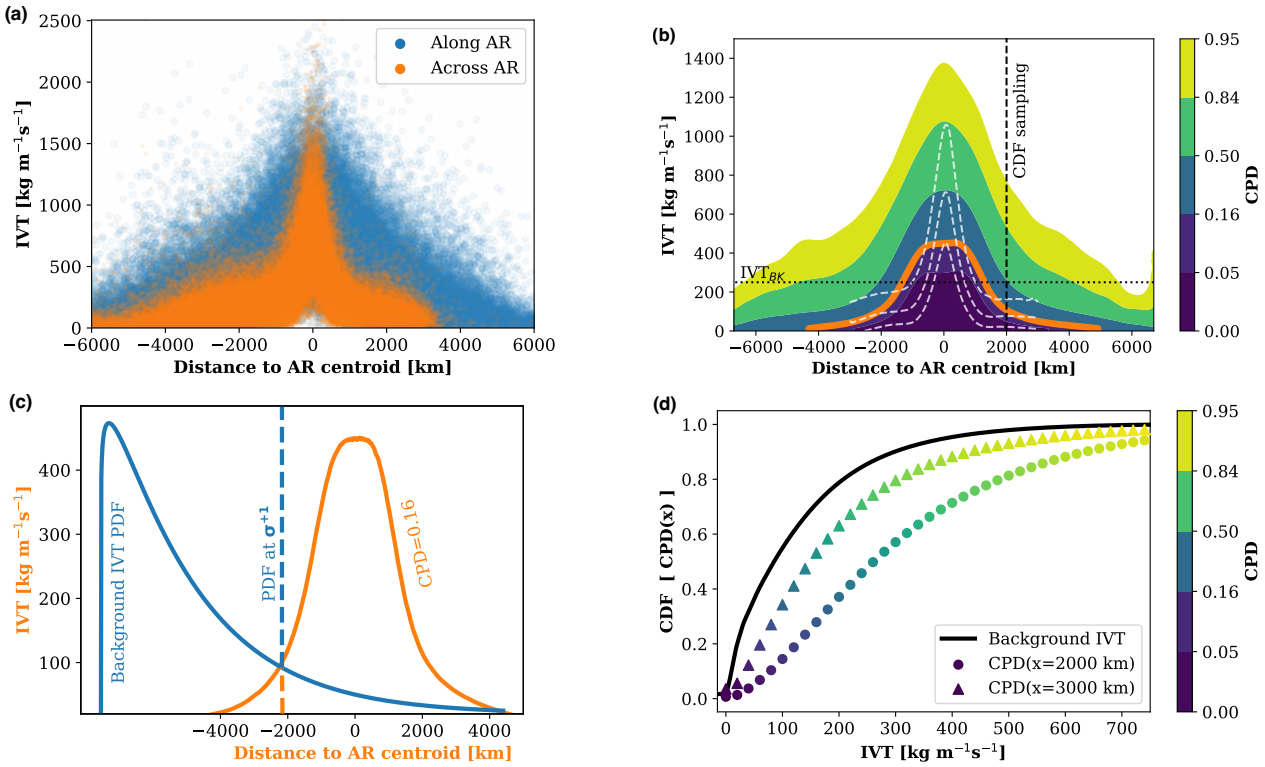

Figure 3.2: (a) Raw sampling of IVT *vs* distance to the AR centroid. (b) Conditional probability distribution of IVT and distance to the AR centroid along the AR composite (white contours show CPD across AR composite). The orange contour represents the 0.16 probability contour. Vertical dashed line shows how we would sample to generate the cumulative density function at a given distance. (c) Illustration of the statistical overlapping method. Blue line shows an sketched background IVT PDF. The orange line is the CPD=0.16 (from panel b). (d) Illustration of two CDF at different distances from the AR composite center. CDF are obtained sampling vertically from the CPD (panel b). Circle markers represent a closer distance to the composite center than the triangle markers.

3.2.7 Implementation of PC, BG, and SO in CMIP5/6 Dataset

In order to analyze the full CMIP5/6 dataset, the calculation of the background IVT, ARCI, and the size estimation methods are implemented as TECA algorithms. This allows an optimized workflow and an easy management of these large datasets. It is worth noticing some analogies between the conceptualization of our size estimation methods and the ARDTs from ARTMIP. PC applies PCA to the absolute IVT field, regardless of the background IVT and can be thought of as analogous to absolute ARDTs. BG and SO statistically compare the AR composite with the background IVT and can be associated with relative ARDTs. We also include a different sub-method SO_{250}, which estimates AR size using the SO method with a fixed $IVT_{\sigma+1}$ of 250 kg m^{-1}s^{-1}, instead of a different value for each model. SO_{250} can be

related to fixed relative ARDTs. ARCI calculates the AR area directly from the are of objects with a detection confidence index $\geq$0.67, a methodology that could be consider analogous to absolute ARDTs, however it is important to notice that ARCI already includes the detection from both absolute and relative methods, so it is a combination of both. We must be careful since this is only a conceptual analogy, and we are not defining new ARDTs or estimating the AR size from the ARDTs data themselves. Nevertheless, this conceptualization is useful when comparing to ARDTs and analyzing changes in AR size under future climates.

3.3 Results

We begin by presenting the results for the background IVT field in Section 3.3.1. Then, in Section 3.3.2, we show the results for the mean AR size, and present an analysis of their change between historical and future simulations. Lastly, in Section 3.3.3, we focus our analysis on the North America landfalling ARs at the end of the life cycle (90%-100% of life cycle). In most of the plots for this Section, the nomenclature will be consistent: each size estimation color is assigned a different color, and each CMIP5/6 model is assigned a different marker. Filled markers represent historical simulations, while empty markers represent future simulations (except for Figure 3.7 where the only markers represent the fractional change in width and length between historical and future runs).

3.3.1 Background IVT Field

This section aims to show the change in the IVT background field across models and between historical and future simulations. Figure 3.3(a) shows a consistent increase in future $\text{IVT}_{\sigma^{+1}}$ between $\sim$10% and $\sim$21% for all CMIP5/6 methods. It is important to notice that despite the increase in $\text{IVT}_{\sigma^{+1}}$ in single models, we find a larger spread in the value $\text{IVT}_{\sigma^{+1}}$ across models ($\sim$28% and $\sim$25% for historical and future simulations, respectively). This suggest that the uncertainty in projected background IVT is dominated by the inter-model variability. Moreover, we find a positive trend in $\text{IVT}_{\sigma^{+1}}$ during the whole 1950-2100 period

of study. Figure 3.3(b) shows a five-year averaged $\text{IVT}_{\sigma+1}$. Although the variability amongh models is large, in general, they agree in the positive trend for the background IVT field from historical to future simulations. This increment in the background IVT field and the inter-

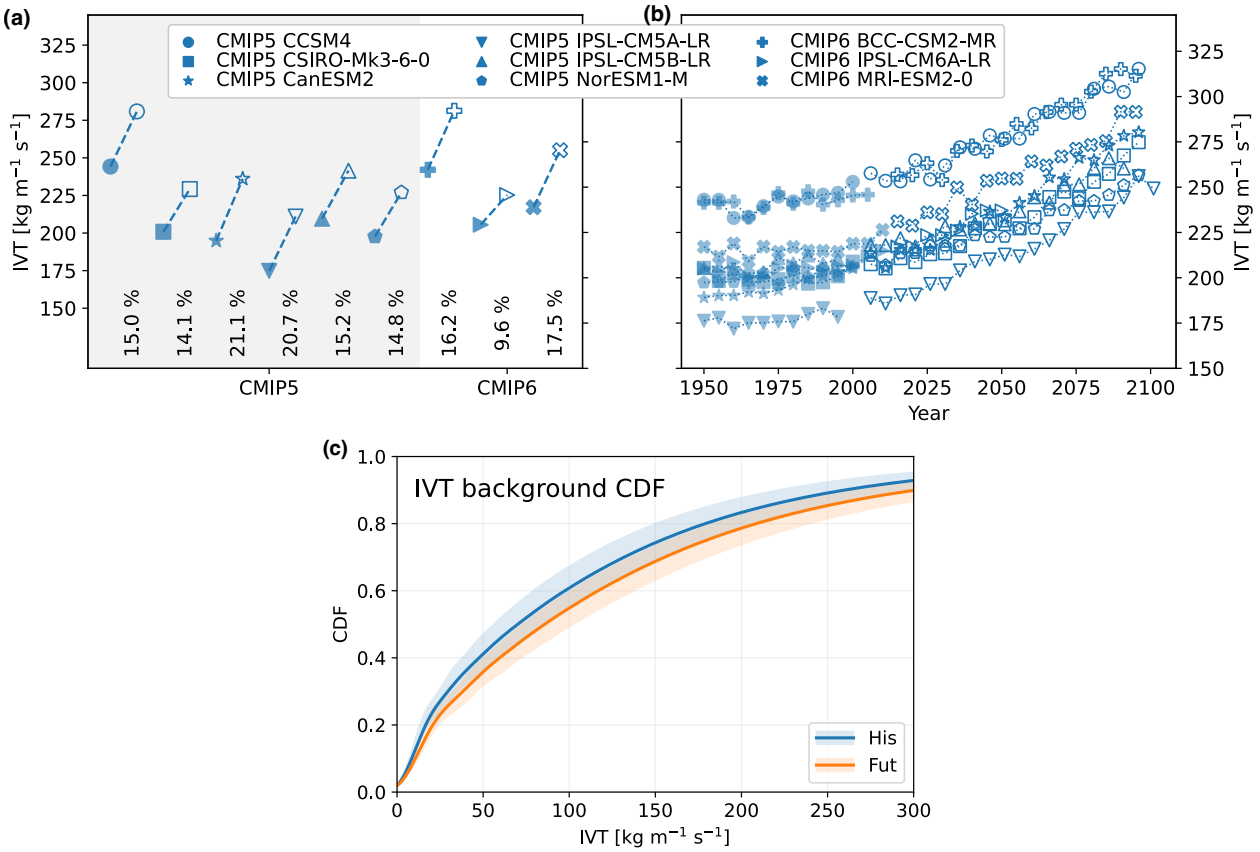

Figure 3.3: (a) Background IVT value of the PDF at +1 standard deviation ($\text{IVT}_{\sigma+1}$) historical and future simulations. Filled markers represent historical simulations, empty markers future simulations. Below the markers, we show the percentage of change in $\text{IVT}_{\sigma+1}$. (b) $\text{IVT}_{\sigma+1}$ calculated every five years for the complete 1950-2100 period. (c) CDF of the background IVT field. Solid lines and shadows represent the mean across CMIP5/6 models and the spread between models.

model variability can he observed in the background CDF. Figure 3.3(c) shows the model mean CDF and spread of the background IVT field. These results gives us confidence that the SO and BG methods capture the change in AR size while accounting for thermodynamical changes in the background IVT.

3.3.2 Mean AR Size

In this section, we present the AR size results for the ensemble mean (length, width, and area). To calculate this mean, we use a random sample from the complete original AR object composite to ensure statistical independence our calculations. Figures 3.4 through 3.6 show the results for AR size across models in historical and future simulations. The gray rectangles represent the change in $IVT_{\sigma^{+1}}$ for each CMIP5/6 models (IVT value is indicated in the right vertical axis). The mean ($\pm$ standard deviation) AR width, length and area for historical simulations are 1167 (991-1344) km, 3407 (3059-3756) km, and 3.15x10^6 (2.32x10^6-3.98x10^6) km^2, respectively. Although for some models we can appreciate a relation between the background IVT changes and AR size and its changes, there is not a consistent pattern that indicates that changes in AR size are dominated by the change in IVT background. It is worth noticing that the size estimation methods that do not take into account the increase in the background IVT (SO_{250}, PC, and ARCI) show a consistent increase in AR size for future scenarios. In contrast, the statistical methods (BG and SO) reflect both positive and negative changes in mean AR size, depending on the CMIP5/6 model.

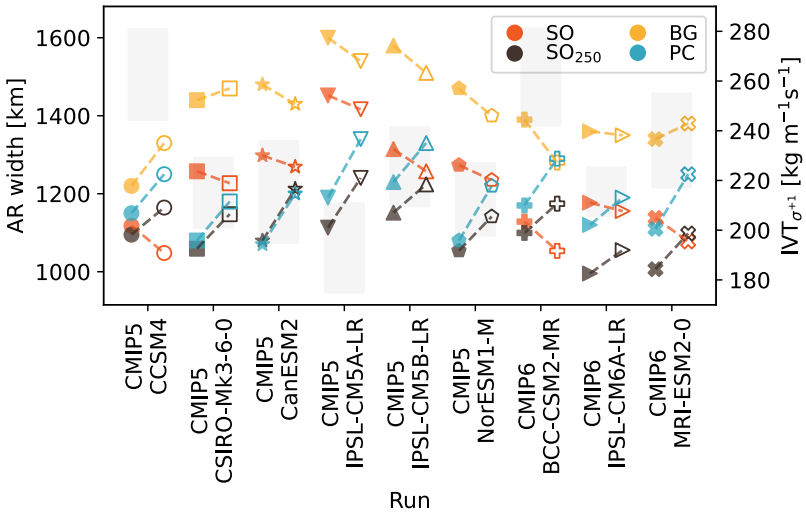

Figure 3.4: AR width from SO, SO_{250}, BG, and PC methods. Historical and future runs are represented by filled and empty markers, respectively. The results from PC represent the median width. Light gray rectangles show the range between the historical and future $IVT_{\sigma^{+1}}$.

Figure 3.7 shows the fractional size change from historical to future simulations. The

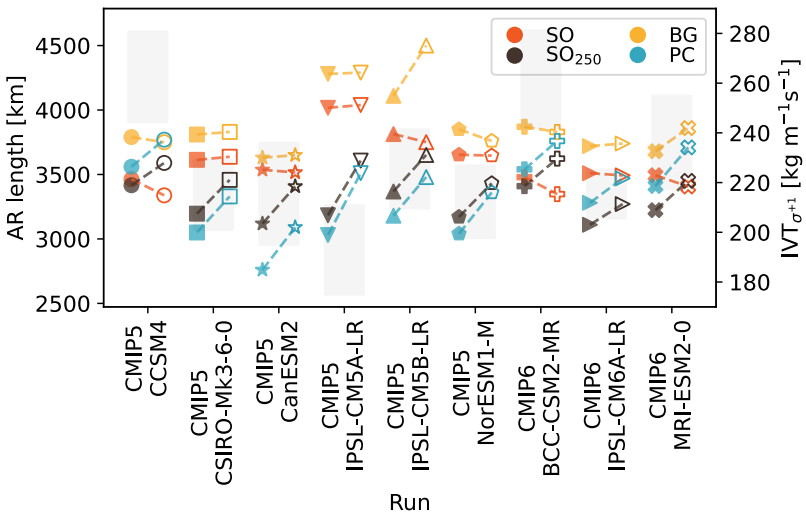

Figure 3.5: AR length from SO, SO_{250}, BG, and PC methods. Historical and future runs are represented by filled and empty markers, respectively. The results from PC represent the median length. Light gray rectangles show the range between the historical and future $IVT_{\sigma^{+1}}$.

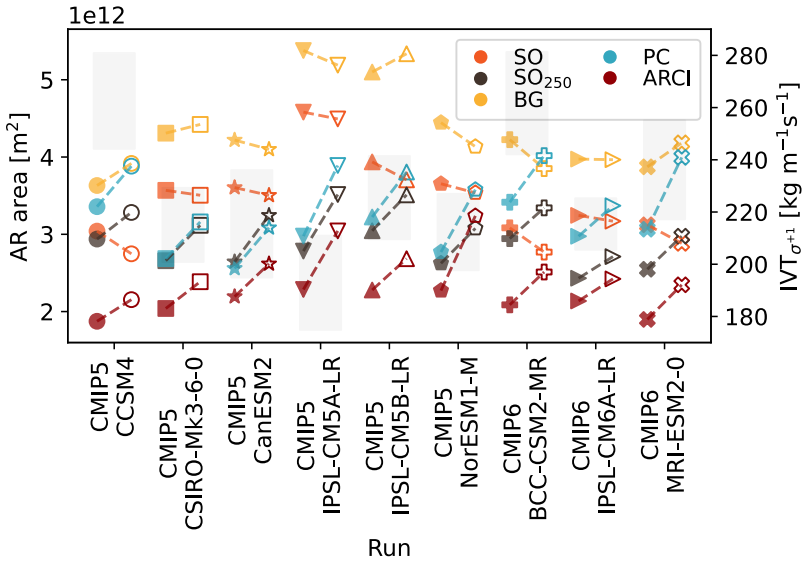

Figure 3.6: AR area from SO, SO_{250}, BG, and PC methods. Historical and future runs are represented by filled and empty markers, respectively. The results from PC represent the median area. Light gray rectangles show the range between the historical and future $IVT_{\sigma^{+1}}$.

gray background denotes positive changes (increase in mean AR size) while white background denotes negative changes (decrease in mean AR size). Solid contours show the fractional area change and the dashed line is the identity line, which represents equal fractional changes in width and length. We show that for SO_{250}, ARCI, PC, and 5 out of 9 models in BG, there is an increment in future AR mean area between 5% and 30%. SO and 4 out of 9 BG cases

show decreases in AR area of less than than ∼10%. It is safe to say that positive changes in future AR size are projected from the CMIP5/6 data. Furthermore, we notice that for the majority of results, AR area change is more sensitive to changes in AR width, regardless of positive or negative area changes.

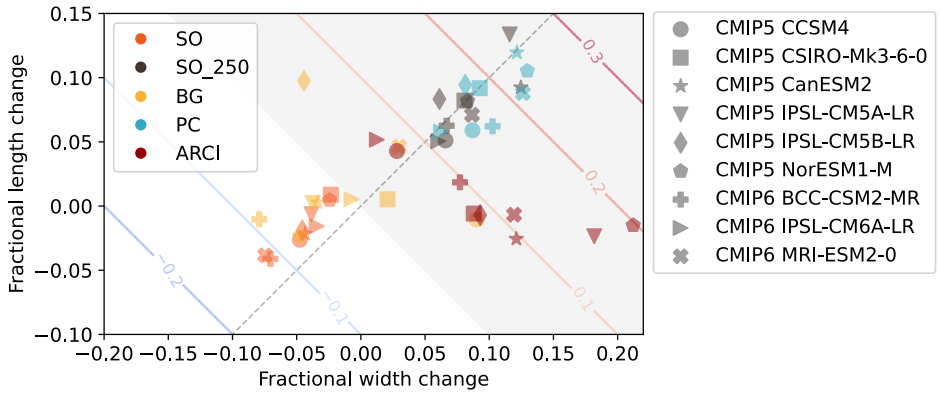

Figure 3.7: Fractional size change between historical and future simulations (area/width/length), calculated with five different methods (SO, SO_{250}, BG, PC, and ARCI). PC and ARCI results represent the median area, length, and width.

It is clear that there is a distinction between the methods that compare the background IVT from those that do not. Both are valid approaches and provide different information. However, to systematically explore the possible changes in landfalling AR impacts, we calculate the mean AR-cross section water vapor transport from the AR width and the mean IVT within the AR composite. In Figure 3.8, we plot the mean IVT within the composite *vs* the mean AR width. Gray solid contours show constant values of AR cross-section water transport with units of 10^3 m^3s^{-1} (to give us a perspective, the Amazon River has a water flux rate of $\sim 209 \times 10^3 m^3 s^{-1}$). We find a consistent increase in AR-cross section moisture transport in the future. Even for the size estimation methods that compare the AR composite to the background IVT field (SO and BG) and have negative changes in AR size, there is either an increase or no change in the mean moisture flux. Table 3.2 summarizes the results for the mean AR change from historical to future simulations and the different size estimation methods.

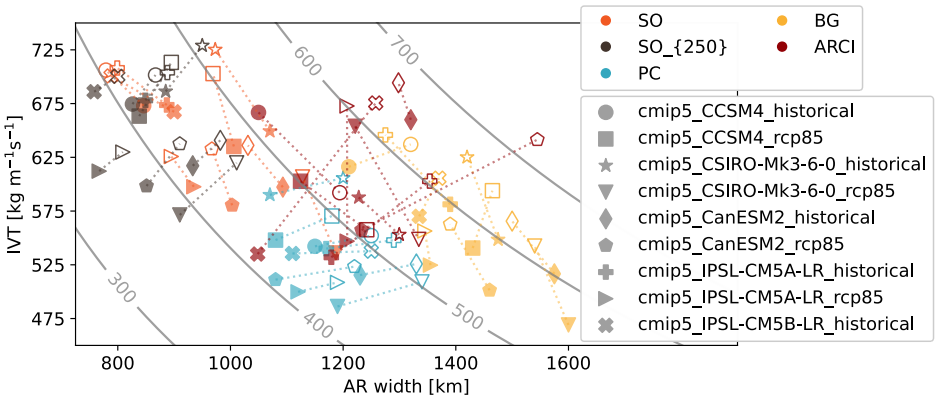

Figure 3.8: AR width and mean IVT from five methods (SO, SO_{250}, BG, PC, and ARCI). Historical and future runs are represented by filled and empty markers, respectively. Results from PC represent the median width. Gray contours show lines of constant AR cross-section water transport in 10^3 m^3s^{-1}.

Table 3.2: Fractional change in AR size from historical to future simulations. Mean (standard deviation) across models.

Mean AR size change

Method	ΔWidth [%]	ΔLength [%]	ΔArea [%]
SO	-6.8 (3.0)	-3.1 (2.8)	-9.7 (5.3)
SO_{250}	6.4 (1.9)	5.3 (2.9)	12.1 (5.0)
BG	-1.2 (4.9)	1.3 (3.5)	0.0 (5.8)
ARCI	8.7 (4.3)	1.8 (2.0)	22.5 (9.0)
PC	10.3 (2.3)	9.3 (3.1)	21.4 (6.4)

3.3.3 North America Landfalling Atmospheric Rivers

The results presented in 3.3.2 represent the change in mean AR size (global AR events during their complete life cycle). This Section analysis focuses on the ARs that make landfall on the North American West Coast (NAWC) at the end of their life cycle (90%-100%). The motivation for this Section arises from Figure 3.9. We find that NAWC landfalling ARs have a higher probability on penetrating further inland for future simulations. Figure 3.9 shows the joint PDF of the final AR centroid longitude and latitude in the CMIP5/6 dataset. The filled/dashed contours represent historical simulations, while thick contours show the PDF of future simulations. NAWC landfalling ARs show increments in mean area of 5%-30% in their area according to SO_{250}, PC, and ARCI methods; and mean area changes between +5% and -15% BG and SO (Figure 3.10). It is worth noticing that despite a decrease in future AR

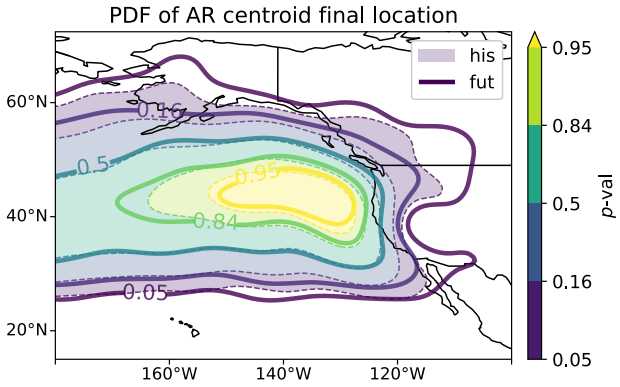

Figure 3.9: Joint PDF of the final AR centroid position (at 90%-100% life cycle), generated using all CMIP5/6 models. Solid thick contours represent future simulations (RCP-8.5 and SSP-8.5). Filled contours represent historical simulations.

areas, some models (CSIRO-Mk3-6-0, IPSL-CM5A-LR, and IPL-CM5B-LR) show an increase in mean AR length, which suggests that width dominates the changes in mean AR area. Furthermore, we find a positive trend in the AR-cross section water transport for NAWC landfalling ARs Figure 3.11 for all CMIP5/6 models and size estimation methods.

For some CMIP5/6 models, SO and BG indicate an increase in AR width. Furthermore, Figure 3.8 shows that for all models/methods, there is a positive trend in the mean AR cross-section water transport. Even for the methods that compare the AR IVT composite with the background field (BG and SO) and predict negative changes in AR size, the thermodynamic effect compensates for the size change in the water flux change.

3.4 Discussion

We have presented evidence that there is an increase in mean AR size for future climate simulations. However, the interpretation of these results must be done carefully. The changes in the background IVT field become relevant when we think of an AR as a signal in a background field. The different ARDTs' sensitivity to thermodynamic changes in IVT will depend on how they treat the IVT or IWV threshold: Absolute ARDTs use fixed thresholds to discriminate AR from the background field; fixed relative ARDTs as those that employ relative thresholds that do not vary with time; and relative ARDTs employ relative thresholds

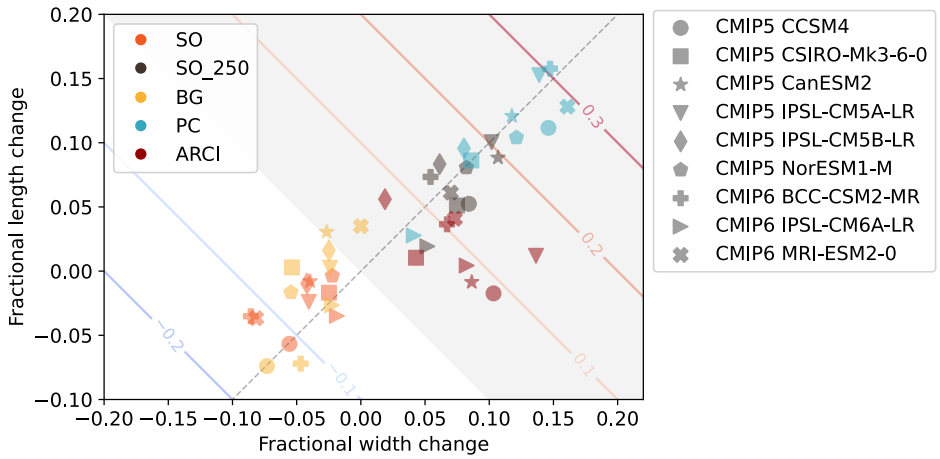

Figure 3.10: Fractional change between historical and future simulations of AR area in width and length at 95% life cycle, calculated with five methods (SO, SO_{250}, BG, PC, and ARCI), for the North America landfalling ARs. Width and length fractional changes are represented by filled and empty markers, respectively. Results from PC and ARCI represent the median length and width.

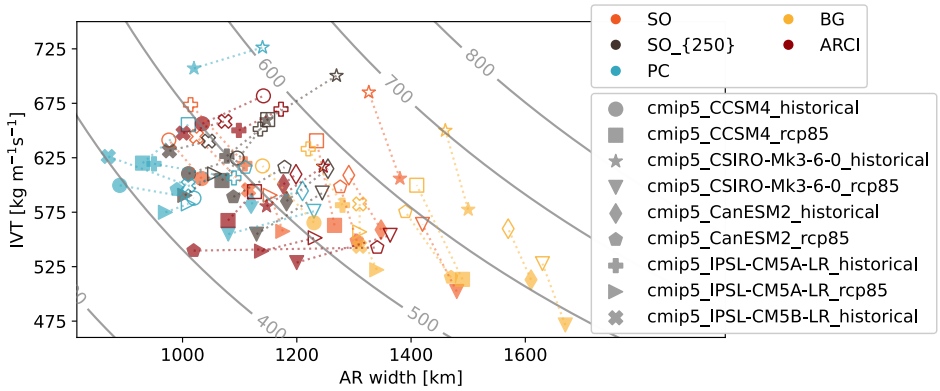

Figure 3.11: Fractional change between historical and future simulations in width/length at 90%-100% life cycle for Northamerica landfalling ARs, calculated with five methods (SO, SO_{250}, BG, PC, and ARCI). Width and length fractional changes are represented by filled and empty markers, respectively. Result from PC and ARCI represent the median length and width.

that vary with time (O'Brien et al., 2021). Moreover, our statistical methods (PC, SO, and BG) estimate AR size in an analogous matter. PC is not exactly equivalent to an absolute ARDT (since it does not impose a fixed IVT threshold). However, PC estimates calculates the covariance matrix of the absolute IVT field without considering the background field. We can relate BG and SO methods to relative ARDTs since both compare the composite IVT to the background IVT field. Additionally, SO_{250} uses a fixed background value throughout historical and future simulations, and we can relate it to the fixed-relative ARDTs. IVT fractional changes are given by the horizontal wind speed magnitude changes and the change

in vertically integrated water vapor due to the Clausius–Clapeyron (CC) scaling (Gao et al., 2015, 2016; Payne et al., 2020). Increments in the background IVT field have been observed in aquaplanet simulations with increased SST, with ∼6% IVT increase per K SST warming McClenny et al. (2020). O'Brien et al. (2021) find a positive trend in global IVT with a rate of 20%-40% per century, with decreases in moisture weighted wind of 5%–15% per century in most of the tropics and midlatitudes, and increases of similar magnitude in the polar regions. $IVT_{\sigma^{+1}}$ results from this work are consistent with these previous studies, projecting that in a global average, the effect that dominates the trend in $IVT_{\sigma^{+1}}$ is the thermodynamic component increases between ∼10% and ∼21% for the RCP8.5 and SSP5-8.5 scenarios (Figure 3.3).

It has been observed that the dynamic contributions to changes in IVT (both ARs and the background field) are smaller than the thermodynamic contributions. However, they may increase in importance in the transition regions between the subtropics and the mid-latitudes (Payne et al., 2020). We can directly observe that regarding AR size, the size estimation methods that take into account the statistics of the background IVT project in fact different changes in AR size than those that do not look at the background. Nevertheless, we must be careful when interpreting these results, since the inter-model spread in the mean $IVT_{\sigma^{+1}}$ is larger than the single models historical to future increases.

One of the main objectives of this work was to provide a narrower range of AR size estimation for future climate scenarios. The range in the median AR area estimation directly from the six global ARDTs (B.1) in the ARTMIP Tier 2 CMIP5/6 experiment is $\sim 10^6$-$6x10^6$ (O'Brien et al., 2021). Although this is considerable narrower than the ARTMIP estimation in Tier 1 (Figure 1.2), our collection of methods still provides a slightly narrower size estimation range of $\sim 2x10^6$-$5x10^6$). O'Brien et al. (2021) sensibly points out that care must be taken when making general statements about the sign of AR frequency/size/count trends, since they are linked to choices that ARDT design. We completely agree with this statement, since our results show different results for future AR sizes depending on the treatment of the background IVT, even when our methods are independent of the ARDTs. It has been shown that different

ARDTs could be detecting different parts of the ARs (Lora et al., 2020), which contributes to the uncertainty in AR size estimation using the ARDTs. Inda-Díaz et al. (2021) raises the question "*could we benefit from the definition of three potential new terms: 'AR core', 'dynamical envelope', and 'thermodynamic envelope'.*" We speculate that if those distinctions were made, each different phenomenon could have different responses to climate change, and affect the definition and estimation of AR size and their impacts in future climates. Our size estimation methods could be adapted to analyze other variables in the filed (for example IWV, wind speed, and precipitation), and they could be used to study the response in size of the different features associated with ARs. This presents an interesting opportunity for future work.

This effect is explicitly exhibited in Figures 3.4-3.7: BG and SO methods take into account the statistics of the background field, giving a different result regarding the change in AR length, width, and area, than SO_{250}, PC, and ARCI.

Regarding AR width, other works have shown systematic increases in AR width with SST warming McClenny (2020). In general, our results agree on the increase in AR mean width with climate change. Only SO shows a consistent decrease in AR width. An interesting finding is that AR width is more sensitive to climate change, and it is the dominant source of variability in AR area, regardless of positive or changes in area. This apparent enhanced response of AR width over length could be related to the previous mentioned different "definitions or parts" of ARs. A future study of these features could help understand this difference. Changes in AR width have underlying implications for continental regions, from the amount of transported water vapor by ARs, to the extent in landfalling impact region from single ARs, since the coastal precipitation due to orographic lifting is directly related to the magnitude of IVT (Neiman et al., 2002; Ralph et al., 2005; Rutz et al., 2019). Wider more intense ARs could mean higher than average precipitation in larger coastal regions, which could have a direct impact in the hydrological hazards of landfalling ARs. Similarly, changes in AR could have direct impacts over continental regions. Assuming ergodicity, longer ARs could more prolonged landfalling AR conditions, that together with the higher IVT magnitudes observed

in our results could derive on increased ARs categories and their impacts over land (Ralph et al., 2019b).

Our results suggests larger ARs with higher cross-section horizontal water vapor transport. These results are particularly relevant for the North American landfalling ARs, since they are a well-studied source of rainfall and hydrological impacts in the region Ralph et al. (2005); Leung and Qian (2009); Guan et al. (2010); Neiman et al. (2013); Ralph et al. (2013); Rutz et al. (2014); Huang et al. (2021). We show that ARs are more likely to penetrate further inland in future simulations. The west coast of North America has been observed to have an increase in precipitation uncertainty in climate change projections, with increases in wet and dry extremes Shields and Kiehl (2016); Payne and Magnusdottir (2015); Polade et al. (2017); Payne et al. (2020). Larger ARs with higher water vapor horizontal transport could affect the characteristics of extreme precipitation in the NAWC. Higher IVT magnitudes in places where historically ARs do not reach that often could affect the hydrodynamic of the water basins and have relevant impacts on flooding hazards in the region (Dettinger, 2013; Lavers and Villarini, 2013a; Lavers et al., 2016b; Dong et al., 2019).

The results presented in this work can help to bring a new perspective for absolute *vs* relative ARDTs in terms of a signal-to-noise problem. Although the absolute ARDTs would not detect the AR dynamical signal *per se*, they are relevant from the AR landfalling impacts point of view since it is the absolute water vapor transport what would produce precipitation. This raises some questions, *if the relative methods better detect the dynamical AR signal, would this mean that the precipitation would be outside the detected relative envelope?*; moreover, *Would absolute methods better represent the precipitation signature under climate change?*. At the moment of the writing of this dissertation, the ARTMIP project has nearly 30 algorithms at the moment. Different ARDTs are generally designed with different objectives in mind. Since there is still an open debate about the definition of an AR and its boundaries, we do not state that one ARDT is better than others, or that the size estimation methods that look into the background IVT field are better. With this work, we expect to provide an objective insight into the study of AR size independently from the design of the AR detection algorithms, and

to encourage future investigation about the different features or weather patterns that right now are being identified as AR. It is possible that these individual features might have different responses under a climate changing and warming world.

3.5 Conclusions

This study analyzed data from the ARTMIP Tier 2 CMIP5/6 experiment to calculate the AR confidence index. Using an object-based tracking method, we estimate the location of ARs based on the AR confidence index for historical and future simulations with strong radiative forcing (CMIP5: RCP-8.5, CMIP6: SSP-858). We create global composites of AR objects and estimate their size (length, width, and area) using four different methods: ARCI, PC, SO, and BG.

We use the value for the IVT background field PDF at +1 standard deviation ($IVT_{\sigma^{+1}}$) as a proxy to analyze the IVT background state across models. Our results show an increase between 10% and 21% in $IVT_{\sigma^{+1}}$ among CMIP5/6 models. However, we need to be careful when applying size estimation methods that compare with the background (also with the use of relative ARDTs) since our results show a spread $\sim$27% in $IVT_{\sigma^{+1}}$ across CMIP5/6 models, which is a larger variation than the mean historical to future $IVT_{\sigma^{+1}}$ increase. Moreover, we find a constant increase in $IVT_{\sigma^{+1}}$ throughout the 1950-2010 period, which suggests that a time-dependent AR size analysis could help understand the response in AR size with climate change.

We find a median AR area of 3.15×10^6 (2.32×10^6-3.98×10^6) km^2 for historical runs, and 3.42×10^6 (2.73×10^6-4.11×10^6) km^2 for future runs. We do not find a clear correlation between the background IVT ($IVT_{\sigma^{+1}}$) and the mean AR area. According to our methods, width is more sensitive to climate change and has a larger contribution than length to the change in AR area. All methods that do not take into account the background IVT (PC, ARCI, and partially SO_{250}) agree on the increment of AR size with climate change. The statistical overlapping method shows a decrease in mean AR size, and the KS–test with the background IVT methods shows increases and decreases in AR size, depending on the CMIP5/6 model.

It is worth emphasizing that regardless of a positive or negative change in AR size for future simulations, the mean AR cross-section water vapor transport increases between 8% and 37% (depending on the model and method). This suggests that the thermodynamical increase in background IVT due to CC scaling dominates over the change in AR size.

Finally, an analysis of AR size for North American West Coast landfalling ARs shows a higher probability for ARs to penetrate further inland in future simulations. Like the global mean results, future North American West Coast landfalling ARs are larger than those in the historical simulations, with higher cross-section mean water vapor transport.

We provide an objective insight into the change in AR size with climate change from an independent perspective of the ARDTs design and algorithms. More research needs to be done to understand these changes better. We recognize that some of our methods are not ideal for more geometrically complicated ARs. We propose exploring the use of non-linear principal component analysis to increment the range of ARs that could be analyzed using our methods. Non-linear PCA could also help in future works estimating the size of less studied AR regions (like the tropics), which are gaining relevance and interest from the scientific community.

Acknowledgment

This study was supported by the Director, Office of Science, Office of Biological and Environmental Research of the U.S. Department of Energy Regional and Global Modeling and Analysis (RGMA) and used resources of the National Energy Research Scientific Computing Center (NERSC), also supported by the Office of Science of the U.S. Department of Energy under Contract no. DE-AC02-05CH11231. We would like to thank the National Council of Science and Technology of Mexico (CONACYT) and UC Mexus for the doctoral fellowship #409048 that partially supported this work. This project was supported by the Environmental Resilience Institute, funded by Indiana University's Prepared for Environmental Change Grand Challenge initiative. We acknowledge the World Climate Research Programme's Working Group on Coupled Modeling, which is responsible for CMIP, and we thank the climate modeling groups (listed in Table 3.1 of this paper) for producing and making available their

model output. For CMIP the U.S. Department of Energy's Program for Climate Model Diagnosis and Intercomparison provides coordinating support and led development of software infrastructure in partnership with the Global Organization for Earth System Science Portals.

Chapter 4

Relationship Between Atmospheric Rivers and the Dry Season Extreme Precipitation in Central-Western Mexico

4.1 Abstract

Atmospheric rivers (AR) are long, narrow jets of moisture transport responsible for over 90% of moisture transport from the tropics to higher latitudes, covering only between 2% and 10% of the earth's surface. ARs have a significant impact on the hydrological cycle of midlatitudes and polar regions. This has developed great interest and community effort to study ARs and their impacts on these regions. It is not until recently that ARs in tropical latitudes are starting to generate interest within the scientific AR community. We use data from the ERA-20C reanalysis and the Bayesian AR detector `TECA-BARD` to show the relationship between extreme precipitation and atmospheric rivers in central-western Mexico (CWM) during the dry-seasons (November-March) in the 1900-2010 period. We find that more than 25% extreme precipitation amount and frequency are associated with ARs, with a maximum of 60%-80% during December and January near the coast of Sinaloa ($\sim$107.5W,$\sim$25N). During these events, composites of the mean meteorological state show "ideal" conditions for orographic precipitation due to landfalling ARs: high plume of horizontal vapor transport perpendicular to the mountain range. We observe high horizontal vapor transport perpendicular to the Sierra Madre mountain range, and a tropospheric wave pattern in vertical velocity, surface pressure, and geopotential height associated with these events. The nature and evolution of these waves need to be further studied in depth. Our results suggest that

TECA-BARD provides a reasonable estimation for AR presence in CWM. Nevertheless, we recommend using more than one ARDT or one tuned explicitly for tropical latitudes. This will allow investigating the response of CWM landfalling ARs to climate change, which could be critical for studying the region's hydroclimatology under future climate scenarios.

4.2 Introduction

Atmospheric rivers (AR) are long, narrow jets of moisture transport typically associated with a low-level jet stream ahead of the cold front of an extratropical cyclone (Ralph et al., 2018). ARs account for over 90% of the water vapor transport from the subtropics to midlatitudes (Zhu and Newell, 1998). Over the last 20 years, there has been an increasing interest in the study and characterization of ARs. There are numerous recent studies that investigate AR and their relationship with extreme wind, precipitation, their impact to the regional hydrological cycles, water mass balance, and extreme hydrological events like flooding and droughts in midlatitude continental regions like North America, Europe, and South America (Neiman et al., 2002; Ralph et al., 2004, 2005, 2006; Dirmeyer and Brubaker, 2007; Neiman et al., 2008; Leung and Qian, 2009; Guan et al., 2010; Viale and Nuñez, 2011; Dettinger, 2011; Ralph and Dettinger, 2011; Warner et al., 2012; Dettinger, 2013; Lavers and Villarini, 2013b,a; Kim et al., 2013; Neiman et al., 2013; Ralph et al., 2013; Rutz et al., 2014; Gimeno et al., 2016; Lavers et al., 2016b,a; Waliser and Guan, 2017; Gershunov et al., 2017; Goldenson et al., 2018; Viale et al., 2018; Eldardiry et al., 2019; Ralph et al., 2019b; Huang et al., 2021). Some works have even investigated the structure of AR using *in situ* data and satellite observations (Ralph et al., 2005; Neiman et al., 2008; Ralph et al., 2010).

The significant impact of ARs on the climatology and hydrology of midlatitudes has generated great interest and community effort in studying ARs and their impacts on these regions. Ralph et al. (2019a) introduced a scale to categorize AR strength based on vapor transport intensity and landfall duration and show that there are beneficial and hazardous impacts associated with AR events. This scale is helpful for the scientific community, and it

is a way of communication with the general public. The AR category scale can be applied to gridded datasets such as reanalysis, forecast, and climate projections. There is also an increasing interest in understanding how ARs and their impact will change in future climates. Payne et al. (2020) concludes that AR response to climate change will have noticeable importance to water balance and regional water resources.

Most of the ARs research focuses on midlatitudes and polar regions. ARs in low latitudes are starting to generate interest within the scientific AR community. This work is motivated by the lack of study of tropical ARs. Moreover, we are also motivated by the personal observation of "unusual non-tropical" precipitation in the Winter of 2019-2020 in Nayarit, Mexico ∼21.5N,104.9W, during the dry season (November-March). We refer to "unusual non-tropical" precipitation as a low magnitude precipitation rate (compared to convective heavy tropical precipitation). During these days, we observed constant rainfall throughout one or two days, very similar to typical California's winter precipitation (Figure 4.1(b) shows the IVT and horizontal wind speed at 700 hPa from one such event). The similarities in the IVT field with the typical characteristics of an AR raised the question: *is this an AR? Are there more events like this, and how are they associated with the extreme precipitation for the dry season in Central-Western Mexico (CWM)?* (thick black contour in Figure 4.1(a)).

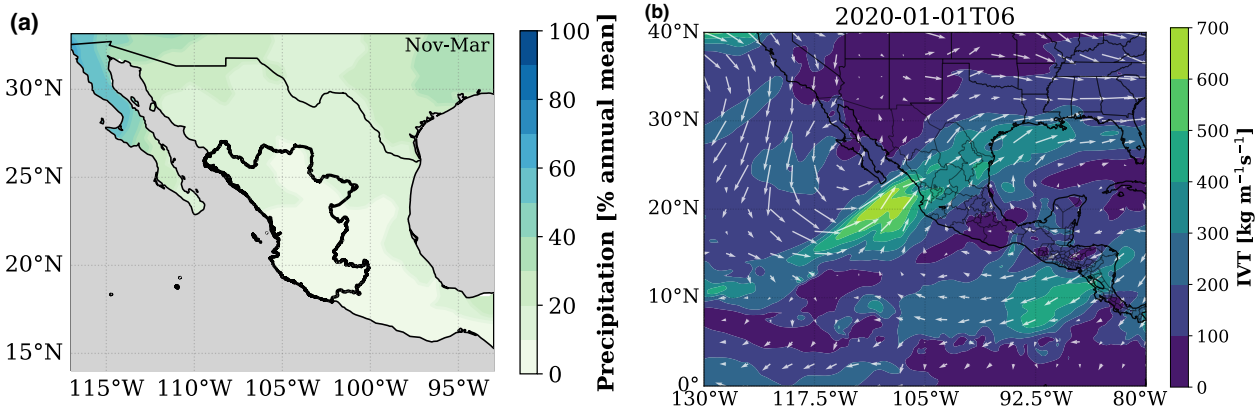

Figure 4.1: (a) Percentage of annual total precipitation from CPC Global Unified Gauge-Based Analysis of Daily Precipitation. Thick black contour used to indicate what is considered as Central-Western Mexico throughout this work. (b) ERA5 reanalysis IVT in color contours. Vectors represent the 750 hPa wind velocity. 2020-01-01 is one of the times when the precipitation in CWM resembled the winter Californian AR-associated rainfall.

CWM is characterized by a dry season from November to March (García Amaro de Miranda, 2003), with a mean monthly accumulated precipitation of less than 10 mm[1] and over 75% of the annual precipitation from July-September, during the spring and summer months. Rainfall in CWM is mainly associated with the North American Monsoon. Less than 10% of the total annual mean rainfall occurs between November and March for most of CWM (Figure 4.1(a)), according to the CPC Global Unified Gauge-Based Analysis of Daily Precipitation[2] (Chen et al., 2008).

From a socio-economic point of view, it is important to study and quantify these events of atypical precipitation. CWM is one of the largest agricultural production regions in Mexico. It is common knowledge among CWM farmers that these rainfall events can be exploited to benefit agriculture; however, we could not find scientific quantification of it. There are even popular beliefs that they can be predicted following a set of heuristic rules (Cruz López, 2011). There is also some evidence that different crops like beans, coffee, and corn, are sensitive to changes in the environmental conditions, like precipitation and humidity (Viguera et al., 2017). Therefore, changes in climate conditions can affect the productivity and quality of the crops (Porter and Semenov, 2005).

Moreover, changes in wind speed and direction, moisture transport, and the location of the intertropical convergence zone (ITCZ) can modify the energy exchange between the atmosphere and the ocean. These changes could generate a displacement northward of the oxygen minimum zone (OMZ), which can affect ocean species distribution and the productivity of regional aquaculture and fisheries (Breitburg, Denise; Grégoire, Marilaure and Isensee, Kirsten, 2018). Furthermore, other studies have observed that dry season rainfall events can change the coastal environment. Coastal water chlorophyll concentration, turbidity, temperature, and salinity, due to increased river discharge, can impact the sustainability of coastal ecosystems and their biological production Domínguez-Hernández et al. (2020); Romero-Rodríguez et al. (2020).

[1] https://smn.conagua.gob.mx/es/climatologia/temperaturas-y-lluvias/resumenes-mensuales-de-temperaturas-y-lluvias

[2] https://psl.noaa.gov/data/gridded/data.cpc.globalprecip.html

Although there are numerous possible effects of anomalous winter precipitation in the CWM region, there is still a lack of documentation about these events and their impacts. Moreover, no existing research links these events with ARs. We investigate the relationship between lower latitudes ARs "dry season" (November-March) rainfall in CWM. We use data from the European Centre for Medium-Range Weather Forecasts (ECMWF) Atmospheric Reanalysis of the Twentieth Century ERA-20C[3] (Poli et al., 2016) and the Bayesian AR Detector `TECA-BARD v1.0.1`. We aim to quantify how much of the CWM winter precipitation is associated with ARs and the meteorological state of the atmosphere during these events.

4.3 Data and Methods

ERA-20C output is 3-hourly with a of ∼125 km on 37 pressure levels. We use data at pressure level: geopotential `z`, wind velocity `u`, `v`, and `w`, specific humidity `q`, temperature `t`, and surface level: mean sea level pressure `mslp`, surface pressure `ps`, total precipitation `tp`, vertical integral of northward water vapor flux `vinwvf`, vertical integral of eastward water vapor flux `viewvf`, and total column water vapor `tcwv`. According to the ERA-20C documentation, the vertically integrated vapor fluxes are calculated in the model coordinates following

$$\text{VIEWVF} = -\frac{1}{g}\int_0^1 qu\frac{\partial p}{\partial \eta}d\eta \approx -\frac{1}{g}\sum_{k=1}^{N} u_k\, q_k \Delta p_k, \tag{4.1}$$

$$\text{VINWVF} = -\frac{1}{g}\int_0^1 qv\frac{\partial p}{\partial \eta}d\eta \approx -\frac{1}{g}\sum_{k=1}^{N} v_k\, q_k \Delta p_k, \tag{4.2}$$

where u and v are the components of the horizontal wind vector, q is the specific humidity, p is pressure, η is the hybrid coordinate (Simmons and Burridge, 1981), index k corresponds to model levels going from the surface ($k = 1$) to the top of the model atmosphere ($k = N$), and Δp_k is the difference in level pressures, estimated at level k. ERA-20C daily forecasted precipitation accumulation has been converted to 3-hourly precipitation rate (with units of mm/d), IWV is used directly from ERA-20C total column water vapor `tcwv`. IVT is calculated

[3] `https://www.ecmwf.int/en/forecasts/datasets/reanalysis-datasets/era-20c`

as the magnitude of the vertically integrated moisture weighted wind (horizontal vapor flux vector) $\vec{u_q}$, directly from ERA-20C eastward and northward water vapor fluxes:

$$\vec{u_q} = (\text{VIEWVF}, \text{VINWVF}), \tag{4.3}$$

$$\text{IVT} = |\vec{u_q}| = \sqrt{\text{VIEWVF}^2 + \text{VINWVF}^2}. \tag{4.4}$$

Additionally, we compare the ERA-20C reanalysis data with observational precipitation, using precipitation data from the Livneh gridded precipitation for the continental US, Mexico, and Southern Canada [4]. The Livneh et al. (2015) dataset is a long-term gridded daily dataset at fine 1/16° (∼6 km) horizontal resolution for the period 1950-2013. We use bilinear interpolation to regrid the AR detection from TECA-BARD in ERA-20C data to the Livneh dataset grid.

4.3.1 AR probability from ERA-20C and TECA-BARD

To calculate the probability of the presence of an atmospheric river (AR probability) we use the Bayesian AR Detector `TECA-BARD v1.0.1`, a probabilistic AR detector implemented in the Toolkit for Extreme Climate Analysis[5] (TECA). TECA-BARD uses a Bayesian framework to sample from the set of AR detector parameters that yield AR counts similar to the expert database of AR counts; this yields a set of "plausible" AR detectors from which we can assess quantitative uncertainty (O'Brien et al., 2020b). We apply TECA-BARD to the ERA-20C data, and asses the plausible presence of an AR at a grid point where where AR probability> 0.05. While 0.05 is a low probability threshold, this indicates a non-zero probability of the existence of an AR in a given grid cell. Since TECA-BARD is inherently designed to detect ARs in mid-latitudes, it filters the IVT field near the tropics, resulting in AR probability that would have lower values in the presence of an AR in tropical latitudes than one in higher latitudes. We hypothesize that AR probability> 0.05 represents a reasonable indication of the presence of an AR in lower latitudes. We test and show this in Sections 4.6 and 4.7.

[4] UCAR: `https://bit.ly/3u8lNts`

[5] `https://github.com/lbl-eesa/teca`

4.3.2 Extreme Precipitation

We calculate the monthly 98th percentile precipitation rate value for ERA-20C and Livneh datasets at each grid cell. We define an *extreme precipitation event* for a given grid cell as the time when the precipitation is above the 98th percentile. We calculate the AR associated extreme precipitation for each grid cell as the precipitation above the 98th percentile when AR probability$>$ 0.05. Since the data record is sufficiently long (1900-2010 for ERA-20C and 1950-2013 for Livneh), we calculate all means and extreme precipitation quantiles monthly. The same holds for the atmospheric state composites described in Section 4.3.3.

4.3.3 Atmospheric State Composites

Following the methodology of Neiman et al. (2008), we create composites of meteorological variables to study the state of the atmosphere at the time of extreme precipitation and AR events at two locations: `Loc1` = 107.5W,25N, and `Loc2` = 105.0W,21N (Figure 4.2, `Loc1` denoted circle marker, `Loc2` by the triangle). `Loc1` is located close to the maximum area of AR-associated precipitation and close to Culiacán Sinaloa, one of the most productive agricultural states of México. `Loc2` is around the most southern region with AR-associated precipitation fraction $\sim$0.5, and in the state of Jalisco, another important agricultural productor in CWM. Both locations are close to the *Sierra Madre Occidental*, a mountain range that extends through Northwestern and Central-Western Mexico, as a part of the North American Cordillera, parallel to the coast. We hypothesize that if there is IVT normal to the *Sierra Madre* during the dry season, it could produce precipitation due to orographic lifting. The methodology to select the time steps to composite is as follows: we find the times when the AR probability is $>$ 0.05 (ar), then we find all the times when the precipitation is above the 98th percentile (pr). We define then AR + extreme precipitation conditions as the times where both conditions ar and pr are met (ar_pr), times when there is ar but no pr (ar_nopr), and times when there is pr but no ar (pr_noar). Finally, the long-term mean is the monthly climatology for 1900-2010 (ltm). We average in time for all the time in each composite, and

create monthly composites. Anomalies are calculated as the specific composite minus the long-term mean. Table 4.1 summarizes the different composite sampling.

Table 4.1: Atmospheric state composites. Composites are created monthly. The number of events at each location is the total number of events for all November-March months.

Atmospheric state composites

Conditions	Name	Anomaly	Events at `Loc1`	Events at `Loc2`
Climatology (long term mean)	*ltm*		134304	134304
AR	*ar*	*ar* - *ltm*	8886	4650
Extreme precipitation	*pr*	*pr* - *ltm*	2690	2688
AR/extreme precipitation	*ar_pr*	*ar_pr* - *ltm*	1549	1003
AR/no extreme precipitation	*ar_nopr*	*ar_nopr* - *ltm*	7337	3647
Extreme precipitation/no AR	*pr_noar*	*pr_noar* - *ltm*	1141	1685

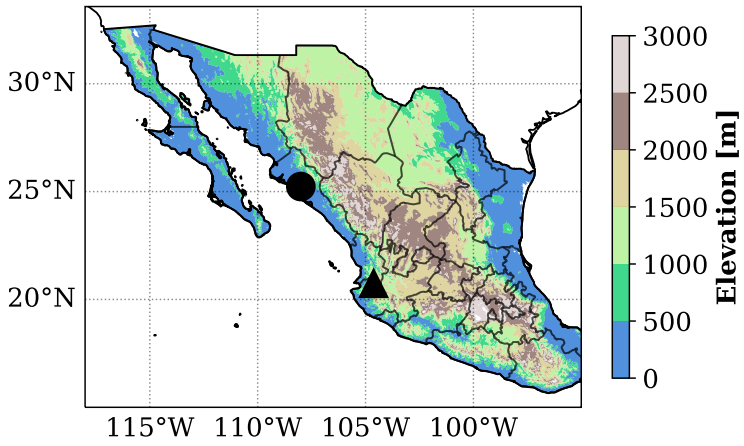

Figure 4.2: Orography of CWM. `Loc1` and `Loc2` are show in circle and triangle markers, respectively. The *Sierra Madre Occidental* is the mountain range that runs through Northwestern and Central-Western Mexico.

4.4 Results

In Section 4.4.1 we present the results of the AR-associated precipitation in CWM during the dry-season (November-March) in the 1900-2010 period. We present the fractional contribution of ARs to the precipitation, using ERA-20C data and the Livneh *et al.* gridded dataset. Sections 4.6 through 4.7 focus on the meteorological state of the atmosphere during extreme precipitation and AR events, and the difference between different composites. In

Appendix C we include additional plots related to the meteorological state of the atmosphere and differences between composites.

4.4.1 AR-associated extreme precipitation

Figures 4.3 and 4.4 show how much of the CWM dry-season precipitation is associated with ARs. Figure 4.3 (a) shows the fraction of ERA-20C total extreme precipitation amount associated with ARs, and (b) shows the same for Livneh precipitation. Figure 4.3 (a) shows the fraction of ERA-20C extreme precipitation frequency associated with ARs, and (b) shows the same for Livneh precipitation. The results are highly condensed in these figures, but they are clear and relevant: The influence of ARs in the dry-season extreme precipitation in CWM extends as far as ∼17N. December has the highest AR-associated precipitation, with ∼75% of the frequency and amount 0.75 near `Loc1`, and between 50% and 60% near `Loc2`. In general, we can say that in the Nov-March, more than half of the extreme rainfall at `Loc1` (more than 30% at `Loc2`) is associated with ARs, both in total amount and frequency.

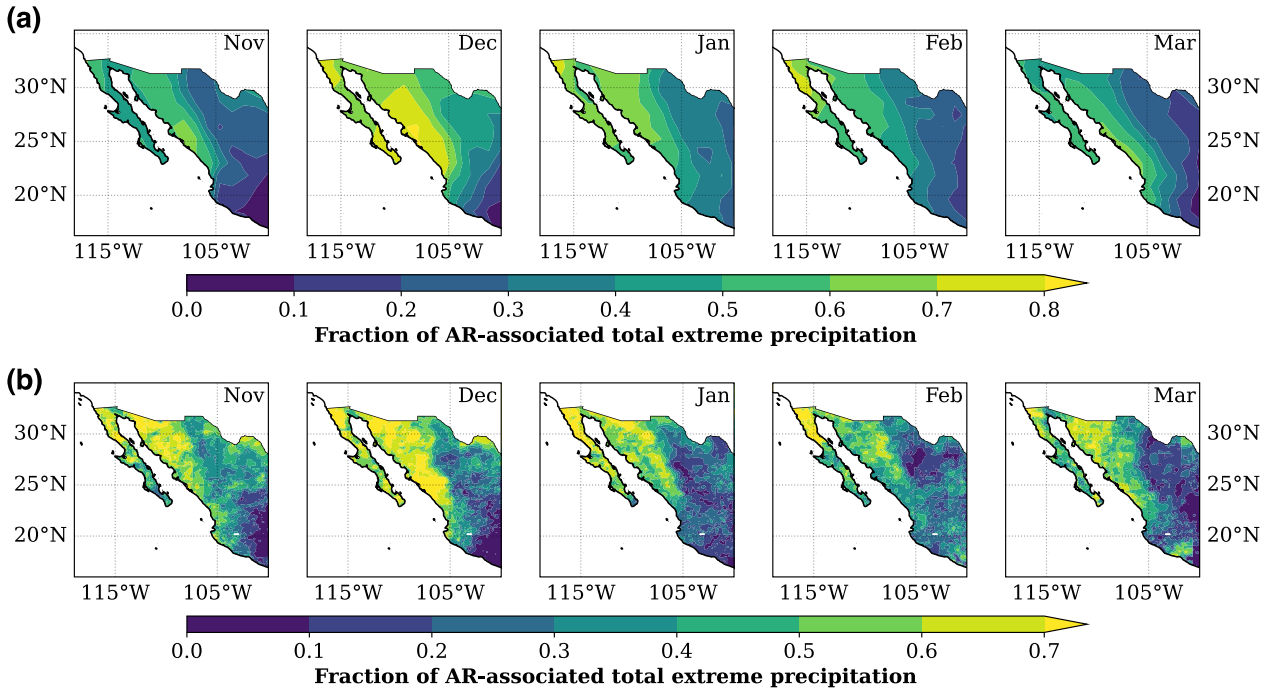

Figure 4.3: Fraction of the total precipitation extreme precipitation (>98th percentile) associated with ARs. (a) ERA-20C 1900-2010. (b) Livneh 1950-2010.

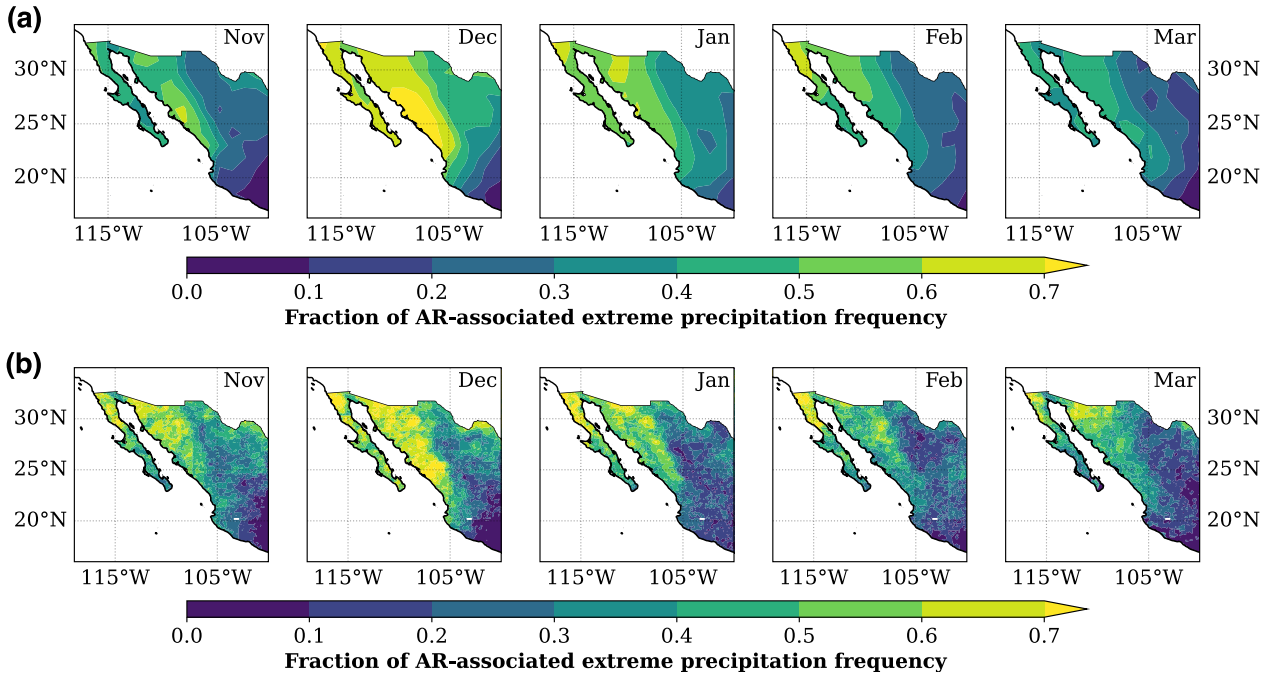

Figure 4.4: Fraction of AR-associated to total extreme (>98th) precipitation frequency. (a) ERA-20C 1900-2010. (b) Livneh 1950-2010.

We have shown the results based on two facts: the total amount of precipitation (and frequency) higher than the monthly 98th percentile for November-March; and the "plausible" presence of an AR in CWM given the `ar_probability`≥0.05. We hypothesize that this precipitation is associated with low latitudes ARs and that `TECA_bard` provides a good insight into the presence of ARs in CWM. This becomes more clear in Section 4.6, where we present composites of the state of the atmosphere during `ar_probability`≥0.05 events at `Loc1` and `Loc2`. For simplicity, in Section 4.5 and 4.6 we show the results for January. Appendix C contains the results for the long-term mean and *ar_pr* composites.

4.5 Long-term Mean

We briefly show the climatological state of the atmosphere (*ltm*) for January. The long-term mean is calculated based using ERA-20C data. Figure 4.5 (a) shows IWV between 10 and 15 kg m^{-2} in CWM, with a maximum of 45 kg m^{-2} near the ITCZ (between 5S and 5N). IVT is shown in Figure 4.5 (b), with values between 0 and 100 kg $m^{-1}s^{-1}$ in CWM (IVT direction

shown with vectors). We note a high IVT plume over the Pacific storm track, and higher IVT values between 5S and 5N associated with the ITCZ. Mean sea level pressure depicts the North Pacific High with its maximum at 130W,30N, shown in Figure 4.5 (c). Geopotential height at 650 hPa, shown in Figure 4.5 (d), has a large gradient between 30N and 60N, associated with the jet stream over midlatitudes, with very little or no spatial patterns over CWM and the central Pacific Ocean. The long-term means for Nov-March are shown in Appendix C (Figures C.1 through C.5). The general structure of the atmosphere is similar to 4.5 (Low IVT and IWV over CWM with the North Pacific High west of the coast of California and Baja California), with slight differences in the locations of the ITCZ, storm track, North Pacific High, etc.

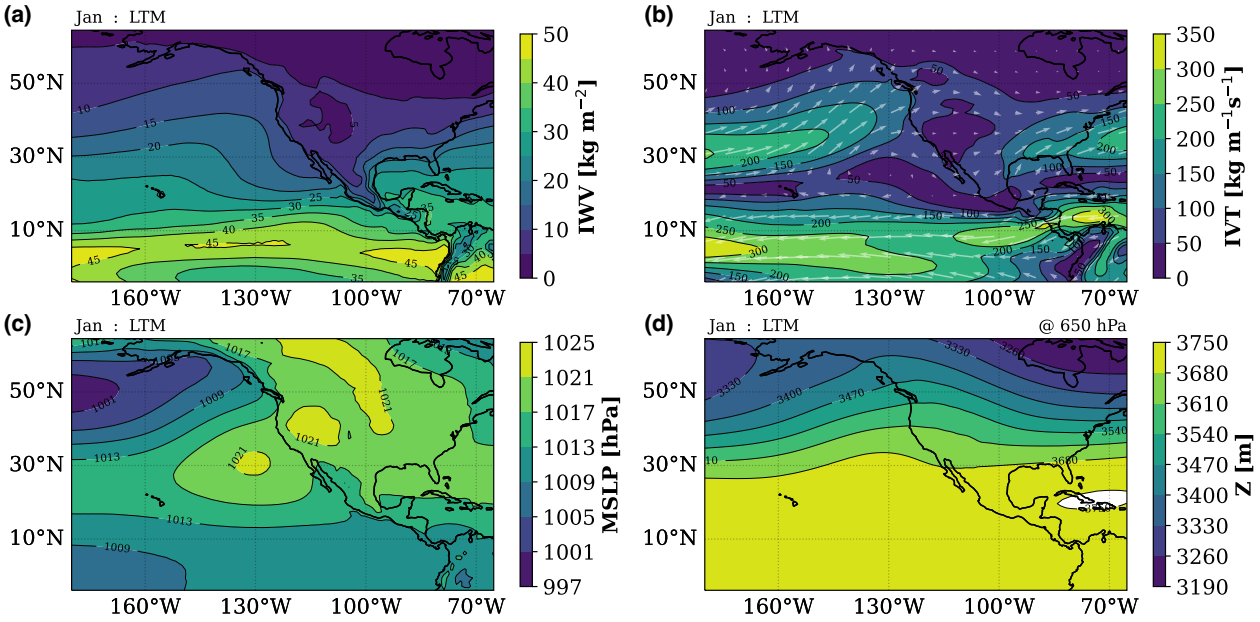

Figure 4.5: Long-term mean for 1900-2010 in December. (a) Integrated water vapor (IWV), (b) integrated vapor transport (IVT), (c) mean sea level pressure (MSLP), (d) geopotential height at 650 hPa. The vectors in panel (b) represent the direction of IVT.

4.6 Extreme Precipitation and AR Events Composite

In this section, we focus on the state of the atmosphere for the *ar_pr* composite (events with extreme precipitation + AR probability ±0.05).

ar_pr composite at Loc1: Sinaloa, (107.5W,25N)

Figure 4.6 (a) shows IVT in colored contours and IWV in dashed white contours. We observe an elongated region of high IWV extending from the ITCZ into CWM, with values up to 30 kg m^{-2} at `Loc1`; as well as a ridge-like structure of high IVT (between 200 and 400 kg $m^{-1}s^{-1}$ centered at `Loc1`, similar to mid-latitude landfalling ARs (Neiman et al., 2008). Figure 4.6 (b) shows IVT anomalies higher than 200 kg $m^{-1}s^{-1}$, and IWV anomalies up to 15 kg m^{-2} near`Loc1`. Mean sea level pressure (grey-filled contours in Figure 4.6 (c)) show the presence of the North Pacific High. Moreover, in 4.6 (d), we observe a low in sea level pressure and geopotential height at 850 hPa anomalies centered near 115W,30N. This wave pattern is more noticeable in Figures 4.6 (e) and (f) (geopotential height at 500 hPa). It is worth noticing that the low-pressure system at the surface is approximately aligned with the mid-troposphere low. This could imply that the wave producing this AR-pattern and anomalous dry-season precipitation is barotropic. However, more analysis is needed to determine the nature and characteristics of these waves. Figures 4.6 (g) and (h) show a mean negative vertical velocity (ascending) over the high IVT plume, ahead of the mid-tropospheric low (with anomalies $\sim$6 hPa s^{-1}). Vectors show the direction of IVT and its anomalies in Figures 4.6 (g) and (h). IVT is normal to the mountain range and `Loc1`, with a weakening of the westward moisture transport near the Equator.

ar_pr composite at Loc2: Jalisco and Nayarit (105.0W,21N)

The *ar_pr* at `Loc2` has a similar general structure to the `Loc1`, with slightly weaker IVT and higher IWV than the `Loc1` composite. Figure 4.7 (a) shows a high IVT ridge near `Loc2` with a maximum value of $\sim$350 kg $m^{-1}s^{-1}$ and IWV $\sim$35 kg m^{-2} near `Loc2`. The mean sea level pressure and geopotential show negative anomalies centered near 26N,110W, with lower magnitude than the `Loc1` composite anomalies (Figures 4.7 (c-f)). An upward 650 hPa wind velocity (and its anomaly) ahead of the tropospheric through, with high IVT normal to the Sierra Madre at `Loc2` (Figures 4.7 (g) and (h)). The genesis and nature of the waves responsible for this weather pattern need to be further explored.

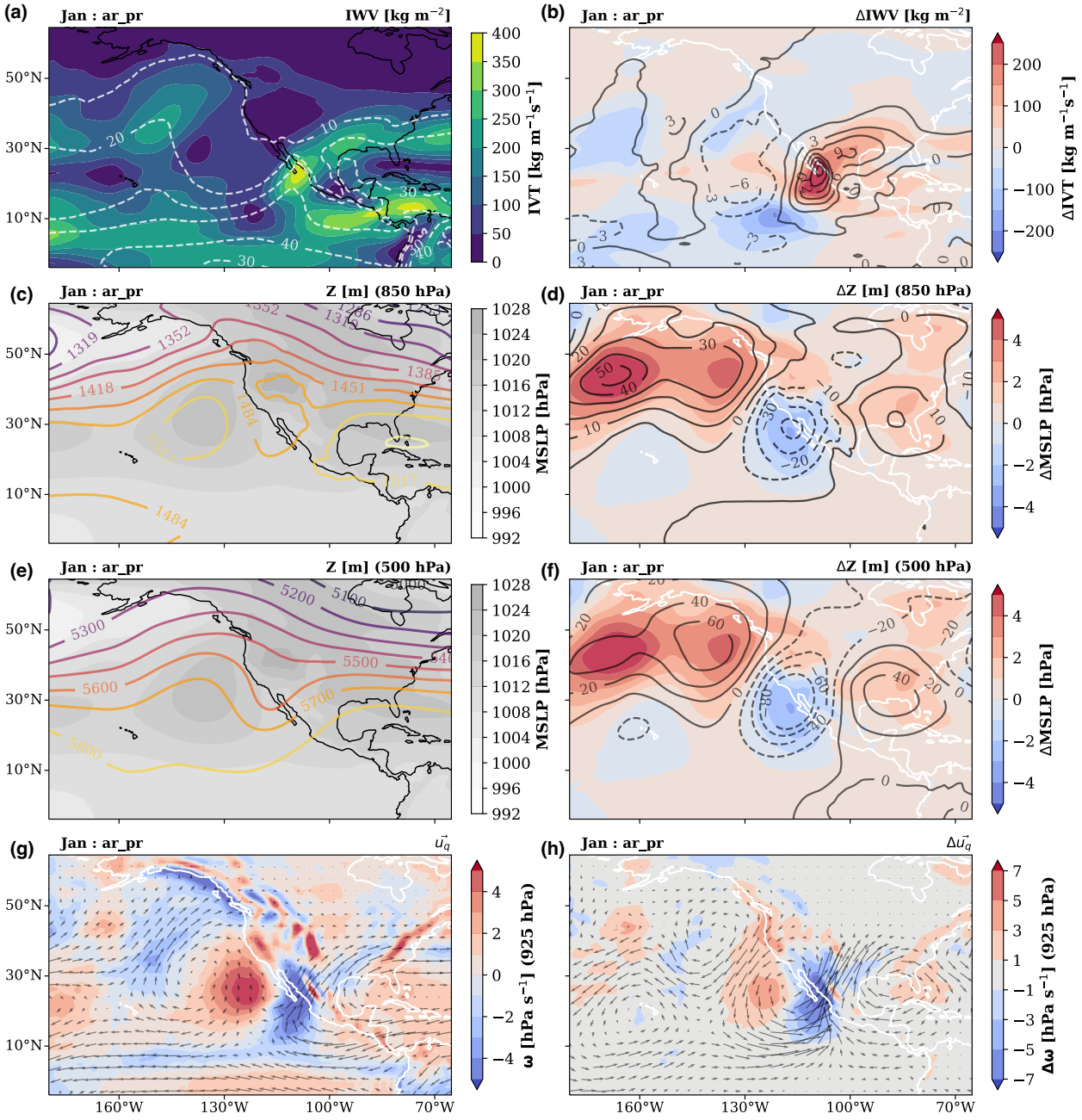

Figure 4.6: State of the atmosphere during AR landfalling and extreme precipitation at `Loc1` in January. Contours variables are specified on the top-right of each plot. Left column: IWV, IVT, mean sea level pressure, geopotential height at 850 and 500 hPA, IVT direction (u_q), and ω at 650 hPa. Right column: anomalies with respect to the long-term mean for the same variables.

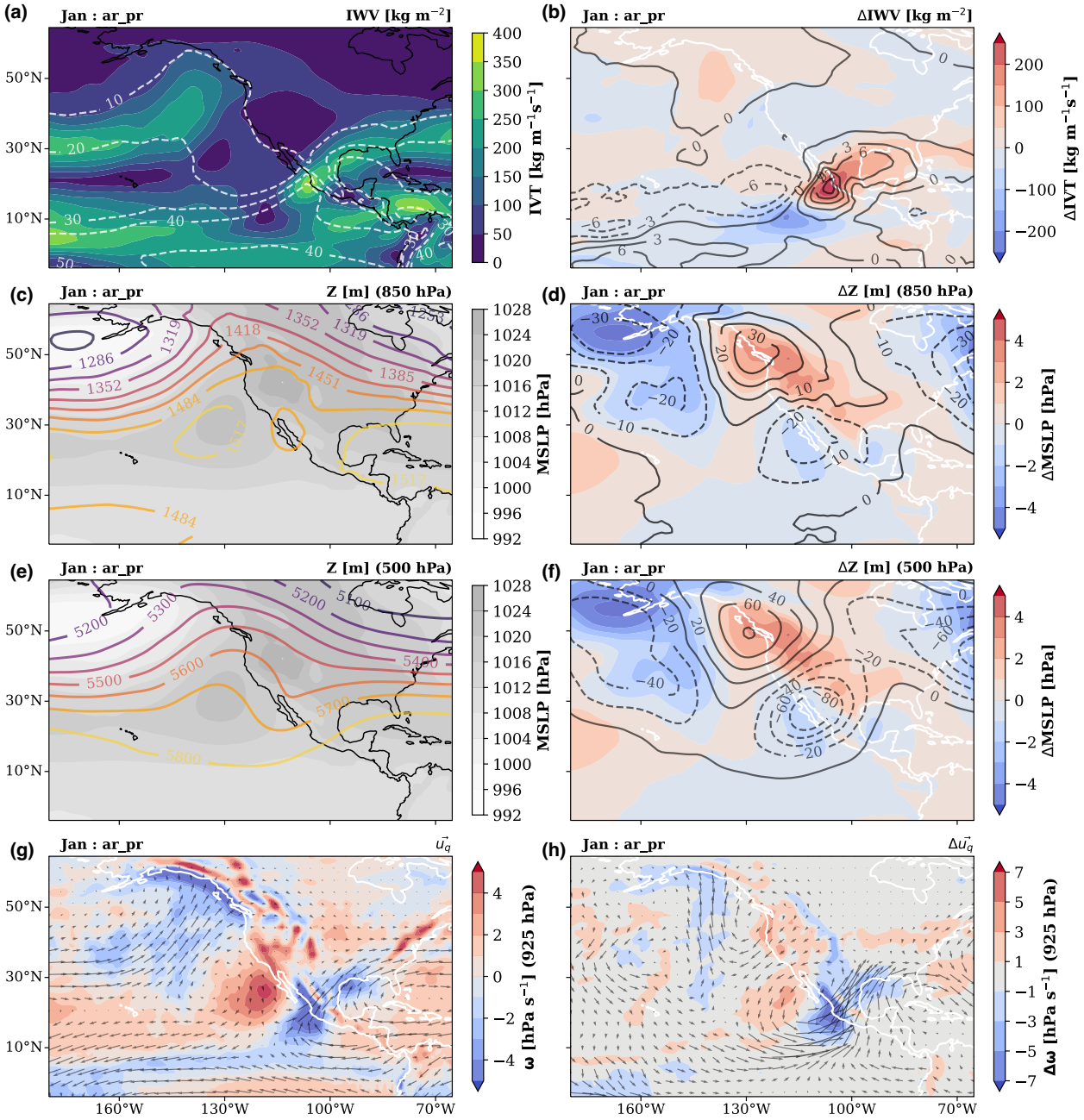

Figure 4.7: State of the atmosphere during AR landfalling and extreme precipitation at `Loc2` in January. Contours variables are specified on the top-right of each plot. Left column: IWV, IVT, mean sea level pressure, geopotential height at 850 and 500 hPA, IVT direction (u_q), and ω at 650 hPa. Right column: anomalies with respect to the long-term mean for the same variables.

4.7 Difference between composites

This work focuses on the relationship between ARs and extreme precipitation during the dry-season in CWM. In Section 4.6 we show the results for the *ar_pr* composite, *i.e.* when extreme precipitation and AR are present. This naturally raises the questions: *what about the other composites?*, *what is the difference between composites?*. For example, what is the difference between the climatology of events with extreme precipitation but no ARs detected (*pr_noar*)? What drives this anomalous rainfall? For simplicity, we focus the results in this section on composites over `Loc1`.

The IWV and IVT for January during extreme precipitation without detection of ARs (*pr_noar*) is shown in Figure 4.8. We observe that the general structure of IVT and IWV are similar to the *ar_pr* composite (surface pressure, geopotential height and vertical velocity plots are shown in Figure C.17). So, how different are they? In Figure 4.9 (b) we observe

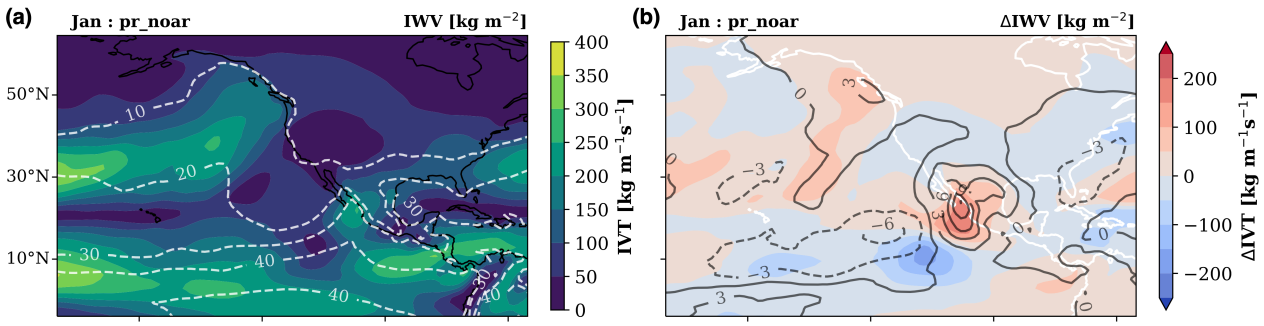

Figure 4.8: (a) IVT and IWV and (b) their anomalies. *pr_noar* composites for January at `Loc1`.

little variation between the two composites for the pressure and 850 hPa geopotential height near CWM. The main difference in the pressure/geopotential fields are in the north part of the domain, where the wave pattern, present in both *ar_pr* and *pr_noar* is stronger for *ar_pr* (positive differences in Figure 4.9 (b)). Nevertheless, the spatial patterns are similar between the two composites. Figure 4.8 shows spatial patterns in moisture fields similar to *ar_pr*, although with weaker magnitudes in IVT and IWV for the *pr_noar* composite (Figure 4.9 (a)), probably due to the weakening of the mid-troposphere wave pattern (Figure 4.9 (b)).

Figure 4.10 shows the IWV and IVT for the *ar_nopr* composite in January, *i.e.* during

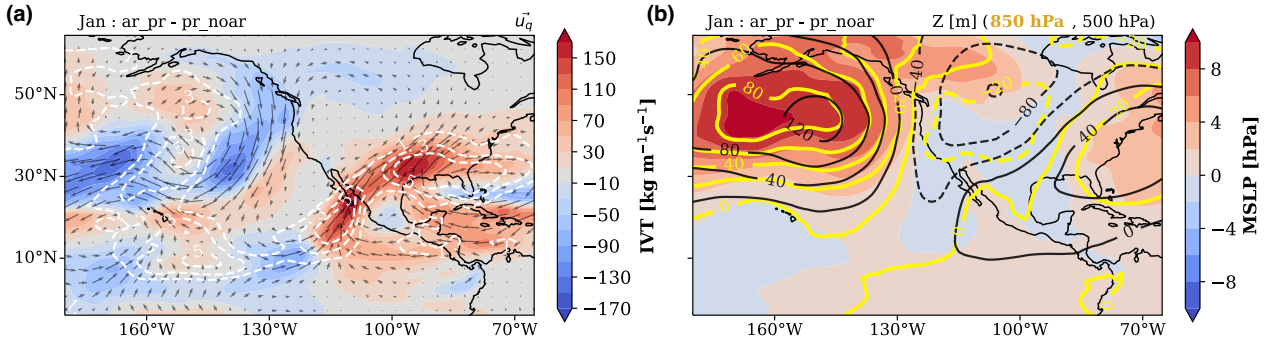

Figure 4.9: Differences in the mean state of the atmosphere between *ar_pr* and *pr_noar* composites for January at `Loc1`. (a) IVT magnitude in filled contours, vectors represent the direction of IVT, and white dashed contours denote changes in IWV. (b) Filled contours show mean sea level pressure differences, thick yellow contours show geopotential height at 850 hPa, and black contours the geopotential height at 500 hPa.

AR detection without extreme precipitation present. We note a moisture transport into `Loc1` (surface pressure, geopotential height and vertical velocity plots are shown in Figure C.16). We notice differences with respect to the *ar_pr* composites in surface pressure. The *ar_nopr*

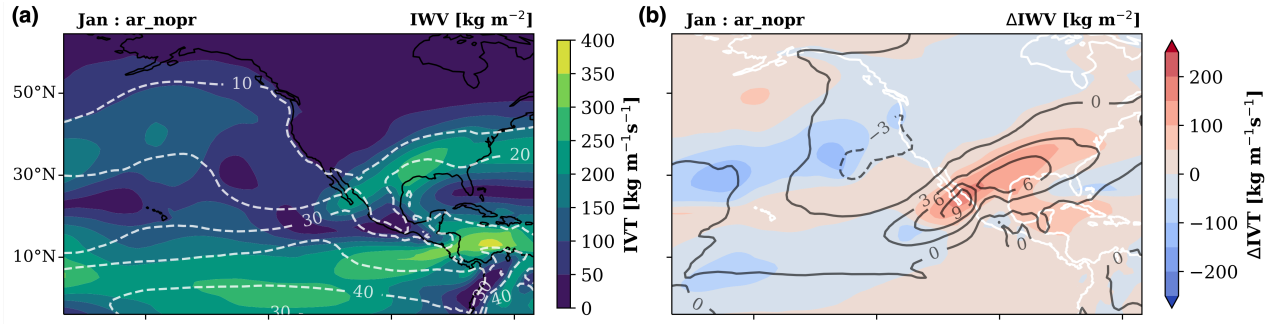

Figure 4.10: (a) IVT and IWV and (b) their anomalies. *ar_nopr* composites for January at `Loc1`.

has a stronger pressure high in the north-west part of the domain, but a weaker low high near CWM (Figure 4.11 (b)). Moreover, a tilting in the geopotential height wave pattern in Figure C.16, and differences in its magnitude create a much weaker IVT magnitude and a difference in IVT direction at `Loc1` (4.11 (a)). This could be due to a stronger mid-troposphere wave associated with the jet stream meandering or the superposition of two or more waves. Again, the nature of the wave producing these weather patterns still needs to be explored and would make an exciting work by itself. Ultimately, the main consequence of these wave differences is that they result in a much weaker IVT magnitude with a different direction, both directly related to orographic precipitation.

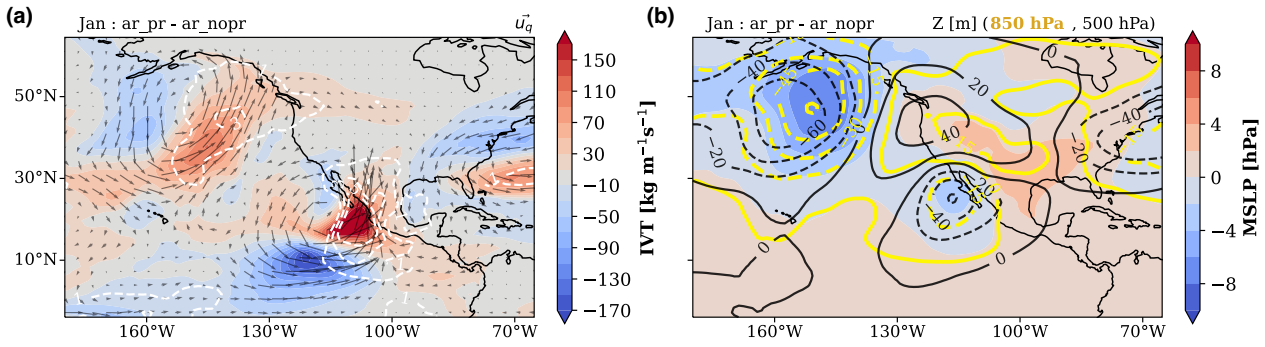

Figure 4.11: Differences in the mean state of the atmosphere between *ar_pr* and *ar_nopr* composites for January at `Loc1`. (a) IVT magnitude in filled contours, vectors represent the direction of IVT, and white dashed contours denote changes in IWV. (b) Filled contours show mean sea level pressure differences, thick yellow contours show geopotential height at 850 hPa, and black contours the geopotential height at 500 hPa.

Figures 4.9 and 4.11 suggest that the different composites might be related to the same or similar weather events or different phases in the same weather event or wave. To explore this, we show the time of the events for each composite in Figure 4.12. There is, in fact, an overlap between composites; in some cases, precipitation events occur before or after ARs but around the same dates in general. This suggests that while we have acceptably identified AR events, an ARDT tuned for tropical latitudes could do improve the AR detection in CWM, which could result in a greater correlation between ARs and dry-season precipitation in CWM. In Appendix C - C.18 we show the full 1900-2010 event composites at `Loc1`.

4.8 Discussion and Conclusions

There is a large amount of literature regarding the impacts of ARs in mid-latitudes and polar regions (Gimeno et al. (2014); Ralph et al. (2017b); Paltan et al. (2017); Rutz et al. (2019); Lora et al. (2020), and references therein) and AR changes with climate change (Lavers et al. (2015); Payne et al. (2020); O'Brien et al. (2021), and references therein). Nonetheless, there is less research about ARs and their effects in lower latitudes (De Luna et al., 2020; De Luna, 2021). It is not until recently that tropical ARs have started to gather scientific interest. Moreover, since the summer precipitation (June-October) dominates the total precipitation of CWM, a significant part of the research has focused on the role of tropical storms and tropical cyclones (Farfán and Fogel, 2007; Díaz et al., 2008; Agustín Breña-Naranjo

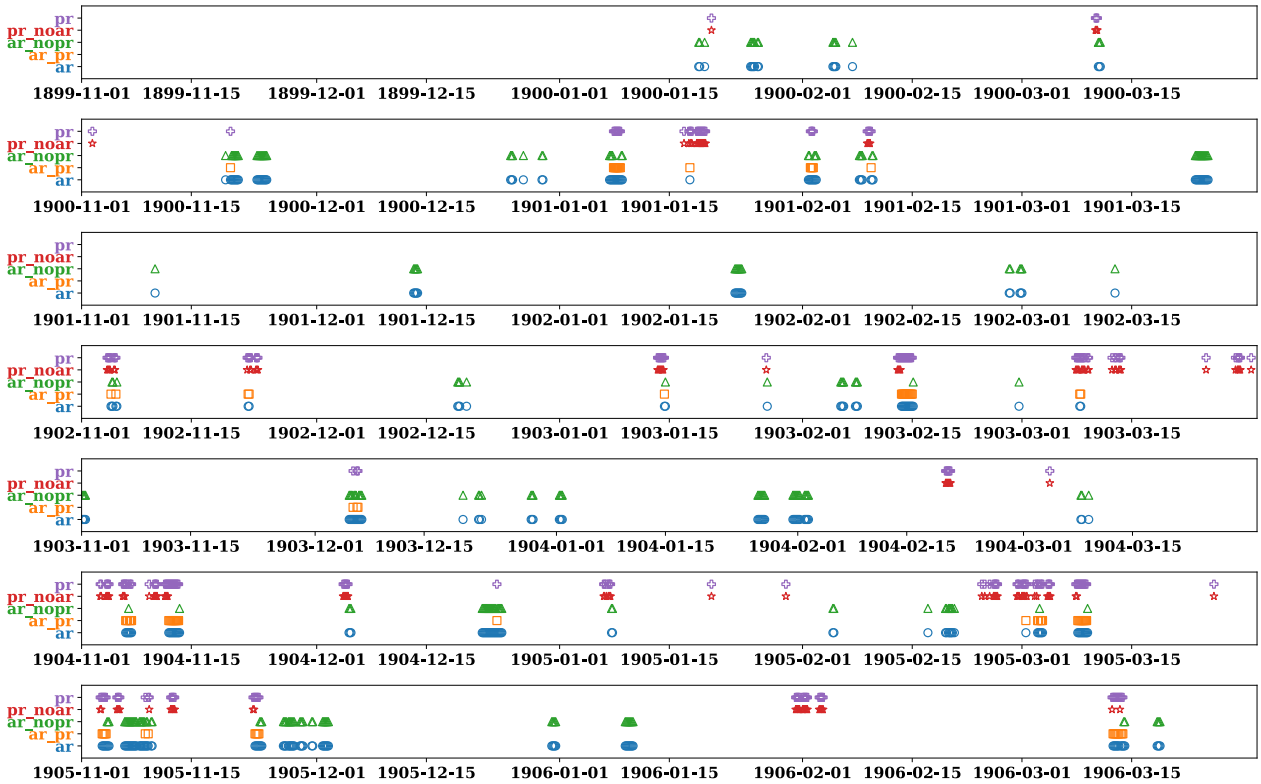

Figure 4.12: Time of events for each composite (*ar*, *ar_pr*, *ar_nopr*, *pr_noar*, and *pr*). Each subfigure shows a year in the 1900-1905 period. Blue circle markers represent *ar*, orange squares *ar_pr*, green triangles *ar_nopr*, red stars *pr_noar*, and purple crosses *pr*.

et al., 2015; Dominguez, Christian and Magaña, Victor, 2018; Dominguez et al., 2020) and the role of the North American Monsoon (Adams and Comrie, 1997; Douglas and Englehart, 2007; Cavazos, Tereza and Arriaga-Ramírez, Sarahí, 2012). Furthermore, some studies associate the fluctuations and trends in precipitation in CWM with large-scale climate features like El Niño Southern Oscillation, Pacific Decadal Oscillation, and the Atlantic Multidecadal Oscillation (Magaña, Víctor and Pérez, Joel and Vázquez, Jorge and Pérez, José, 2003; Matías Méndez and Víctor Magaña, 2010; Curtis, 2007; Arriaga-Ramírez, Sarahí and Cavazos, Tereza, 2010). In particular, CWM appears to be a transition region between the Mediterranean rainfall regime in California and northern Baja California and the summer-dominated tropical rainfall regime and the North American Monsoon. This, together with the relatively developed AR research, has resulted in an overlook of the dry-season (winter) precipitation and its association with tropical ARs.

Here, we present clear evidence of the relationship between CWM dry-season precipi-

tation and ARs. Our composites reflect a high degree of similarity with other compositing studios in higher latitudes (Neiman et al., 2008). Nevertheless, many aspects of these tropical ARs still need to be studied. Investigating the characteristics of the waves that create these anomalous IVT filaments and rainfall is key to understanding these weather patterns and their implications in the CWM dry-season hydrological cycle. Moreover, ARs have been typically associated with mid-latitude baroclinic waves and extratropical cyclones (ETC). However, recently Zhang et al. (2019b) showed that nearly 20% of ARs are not nearby an ETC. Here we have presented evidence that aligned surface amd mid-troposphere weaves are associated with tropical ARs in CWM, and could possibly denote a barotropic nature of these waves. There is no doubt that we still have a lot to learn and explore about ARs, particularly lower latitudes ARs. We still need to determine the genesis of these events. Are they more related to extratropical weather patterns like an amplification of mid-latitude waves? or maybe to tropical dynamics, energy balance, and responses to shifts in the ITCZ (Haffke and Magnusdottir, 2013; Choi et al., 2015; Lintner and Boos, 2019). In other words, *are these events, in fact, atmospheric rivers, or are they another weather phenomenon?*. We show clear evidence that there is a reasonable degree of similarity between winter ARs in CWM and typical mid-latitude ARs, so a more reasonable question may be *how similar or how different are tropical and mid-latitude ARs?*.

Although ARs in CWM do not dominate the total annual precipitation like on the US West Coast, they regulate extreme precipitation during the dry season. The water vapor in ARs frequently leads to heavy precipitation where they are forced upward by mountains (Ralph et al., 2018; Smith et al., 2009; Ralph et al., 2019a). The presence of the *Sierra Madre Occidental* in CWM provides a creates an ideal mechanism for orographic rainfall during high IVT events in CWM. Therefore, it is relevant to quantify and understand these tropical ARs and their influence on the regional hydrological cycle of CWM. We recognize that this study (and future studies) could benefit from an ARDT tuned for tropical latitude, which brings back the question of how similar these ARs are to "traditional" mid-latitude ARs. The uncertainty in AR detection is key to answering this question. It has been discussed the

possibility that there is more than one type of dynamical phenomenon that produces AR-like objects and that different definitions for these processes could help in future studies (Inda-Díaz et al., 2021; O'Brien et al., 2021). This gains particular relevance for the study of future ARs in CWM, because, in general, different "types" of AR-like phenomena (including CWM landfalling tropical ARs) could have different responses to climate change. There is some evidence of future AR frequency increases in lower latitudes (De Luna et al., 2020). Although the frequency increase magnitude is lower than for higher latitudes, there is no assurance on how the local hydrology will be impacted by changes in other AR quantities (intensity, size, orientation, geometry, among others).

In summary, we use data from the Atmospheric Reanalysis of the Twentieth Century ERA-20C and the TECA-BARD AR detector to demonstrate the relationship between extreme precipitation and atmospheric rivers in central-western Mexico during the dry-season (November-March) of 1900-2010. We find that more than 25% of extreme precipitation amount and frequency are associated with ARs, with a maximum of 60%-80% during December and January near the coast of Sinaloa ($\sim$107.5W,$\sim$25N).

We calculate composites of the mean state of the atmosphere during AR and extreme precipitation events. We find that for the AR and precipitation composite (*ar_pr*), there is a positive anomaly in IWV and IVT. Horizontal vapor transport is normal to the coast and the mountain range of the Sierra Madre. Vertical velocity has upward anomalies alongside the high IVT envelope. Besides changes in horizontal moisture transport, sea level pressure and geopotential height anomaly fields show a wave pattern associated with the *ar_pr* composite. A weakening of the surface pressure high and the presence of geopotential lows (above 850 hPa) suggest that the moisture transport occurs at a higher level than typical mid-latitude ARs.

Additionally, we examine the differences between composites. Our results suggest that the AR events without precipitation have a lower IVT magnitude. Furthermore, they show a tilted wave pattern in the geopotential height field with respect to the AR with precipitation composite. Taken together, this translates into lower horizontal vapor transport values

with different orientations with respect to the mountain range, resulting in lower precipitation rates. Furthermore, we show that the main difference between the precipitation events with/and without ARs composite is IVT magnitude. Both composites have similar pressure and geopotential wave patterns near the coast of CWM. The pressure and low atmosphere geopotential main differences are located north of 30N. These results suggest that the precipitation without AR events in fact is related to the AR events. Both composites could be part of the same weather pattern that our ARDT failed to detect due to the lower IVT magnitude and its inherent design to filter out the tropics.

The nature and genesis of these anomalous IVT events and dry-season precipitation –or apparent tropical ARs– still need to be determined, and we plan to explore them in future work. We recommend using more than one ARDT, or one tuned explicitly for tropical latitudes, which could sharpen the correlation between ARs and CWM winter precipitation. This will allow investigating the response of CWM landfalling ARs to climate change, which could be critical for studying the region's hydroclimatology under future climate scenarios.

Acknowledgment

CPC Global Unified Precipitation data provided by the NOAA/OAR/ESRL PSL, Boulder, Colorado, USA, from their Web site at `https://psl.noaa.gov/data/gridded/data.cpc.globalprecip.html`. We would like to acknowledge the European Centre for Medium-Range Weather Forecasts and ERA-20C Project (`https://www.ecmwf.int/en/forecasts/datasets/reanalysis-datasets/era-20c`). ERA-20C was accessed through the Copernicus Climate Change Service (C3S) Climate Data Store (CDS) - `https://apps.ecmwf.int/datasets/data/era20c-ofa/`. We acknowledge Livneh, Ben & National Center for Atmospheric Research Staff (Eds). Last modified 12 Dec 2019. "The Climate Data Guide: Livneh gridded precipitation and other meteorological variables for continental US, Mexico and southern Canada." Retrieved from `https://climatedataguide.ucar.edu/climate-data/livneh-gridded-precipitation-and-other-meteorological-variables-continental-us-mexico`. This study was supported by the Director, Office of Science, Office of Biological

and Environmental Research of the U.S. Department of Energy Regional and Global Modeling and Analysis (RGMA) and used resources of the National Energy Research Scientific Computing Center (NERSC), also supported by the Office of Science of the U.S. Department of Energy under Contract no. DE-AC02-05CH11231. We would like to thank the National Council of Science and Technology of Mexico (CONACYT) and UC Mexus for the doctoral fellowship #409048 that partially supported this work. This project was supported by the Environmental Resilience Institute, funded by Indiana University's Prepared for Environmental Change Grand Challenge initiative.

Chapter 5

Conclusions

This dissertation focuses on two related subjects: AR size and its change with future climate scenarios and the relationship between Central-Western Mexico winter precipitation and ARs. The overarching motivation of the first part is to develop and implement AR size estimation methods that are independent of the design of ARDTs. In this fashion, we aim to provide an objective insight into the AR size and geometric characteristics and their change in future simulations. This could be used as a reference or supplemental aid for tuning existing ARDTs or designing new algorithms. In this matter, we have succeeded and provided a narrower range of size estimation with respect to the ARTMIP collection. The second part of this dissertation is motivated by the lack of study of ARs in lower latitudes and the personal observation of winter precipitation in Mexico and its resemblance to the AR-produced precipitation in California. Although the quantitative definition of AR is still an open research question, the general meteorological state shows that the dry-season extreme precipitation in CWM is associated with AR-like events. This is an interesting result by itself since ARs have been typically associated with higher latitude impacts. Therefore, we aim to provide a comprehensive preliminary inspection of this association to motivate further and more profound research about these meteorological events.

5.1 Summary

In Chapter 2 we develop and implement five independent size estimation methods to characterize the size of ARs that make landfall over the West Coast of North America in the 1980-2017 period and reduce the range of size estimation from the ARTMIP ensemble. Our results show that ARs that originate in the Northwest Pacific (WP) (100°E-180°E) have larger

sizes and are more zonally oriented than those from the Northeast Pacific (EP) (180°E-240°E). ARs become smaller through their life cycle, mainly due to reductions in their width. They also become more meridionally oriented towards the end of their life cycle. Overall, we provide a range of AR areas (between $7\text{x}10^{11}\text{m}^2$ and 10^{13} m^2) that is several orders of magnitude narrower than current methods estimation. In addition, we find a composite AR width (length) between 394-1550 km (1580-3842 km), depending on the size estimation method. North America landfalling ARs originated in the EP (WP) have an orientation with respect to the equator between $\sim 31°$ ($\sim 41°$), with mean aspect ratios (length/width) between 2.8 and 5.2.

In Chapter 3 we expand the use of the methods developed in Chapter 2. We analyze data from the ARTMIP tier 2 CMIP5/6 experiment to calculate the AR confidence index. Using an object-based tracking method, we estimate the location of ARs based on the AR confidence index for historical and future simulations with strong radiative forcing (CMIP5: RCP-8.5, CMIP6: SSP-858). We create global composites of AR objects and estimate their size (length, width, and area) using four different methods: ARCI, PC, SO, and BG. We show an increase between 10% and 21% in the background IVT field among CMIP5/6 models (via the $\text{IVT}_{\sigma^{+1}}$). However, we need to pay special attention to these changes' implications. Our results show a more extensive spread in $\text{IVT}_{\sigma^{+1}}$ across CMIP5/6 models than the individual model increases from historical to future background field. Moreover, a constant $\text{IVT}_{\sigma^{+1}}$ throughout the 1950-2100 period suggests that a time-dependent AR size analysis could help understand the response in AR size to climate change. Our results show a mean AR area of $3.15\text{x}10^6$ ($2.32\text{x}10^6$-$3.98\text{x}10^6$) km^2 for historical runs, and $3.42\text{x}10^6$ ($2.73\text{x}10^6$-$4.11\text{x}10^6$) km^2 for future runs. According to our methods, width is more sensitive to climate change and has a larger contribution than length to the change in the AR area. Most CMIP5/6 models and size estimation methods project an increment in AR size with climate change. Furthermore, regardless of the individual positive or negative change in AR size, the mean AR cross-section water vapor transport increases between 8% and 37% in future simulations. This suggests that the thermodynamical increase in background IVT due to CC scaling dominates over the change in AR size. These results hold for the particular case of North American West Coast

landfalling ARs, with the particular caveat that there is a higher probability of ARs going further inland in the future. Our methodology provides an objective insight into the change in AR size with climate change from an independent perspective of the ARDTs design and algorithms.

In Chapter 4, we look into the relationship between dry-season (November-March) precipitation in Central-Western Mexico and atmospheric rivers. We use ERA-20C reanalysis data and the TECA-BARD Bayesian AR detector. We find that in the 1900-2010 period, more than 25% extreme precipitation amount and frequency are associated with ARs in CW, with a maximum of 60%-80% during December and January near the coast of Sinaloa ($\sim$107.5W,$\sim$25N). We demonstrate that although TECA-BARD is not tuned explicitly for AR detection in the tropics, we can use the probability of AR detection to establish a plausible presence of ARs. An analysis of the state of the atmosphere during extreme precipitation and AR events in CWM shows a high degree of similarity with higher latitude ARs meteorology. We find an enhanced mean IWV (30 kg m^{-2}) and IVT (400 kg $m^{-1}s^{-1}$) pointing perpendicularly to the coast of CWM and the Sierra Madre Occidental. Besides, surface pressure suggests that horizontal vapor transport is above typical AR altitudes. Furthermore, we find a wave pattern in the pressure and geopotential height fields (apparently barotropic). Also, we find ascending vertical velocities (in the absolute and anomaly fields) aligned with the high IVT ridge, which, together with the high IVT, provides the ideal conditions for orographic precipitation over the Sierra Madre. Moreover, we explore the difference between composites of ARs with and without extreme precipitation. We find a weakening of the mid-troposphere wave pattern, with tilting in the geopotential height anomalies. This creates a lower mean IVT magnitude and a shift in the direction of IVT, which could be the reason for the absence of extreme precipitation during these events. Lastly, we analyze the difference between the composite with extreme precipitation, with and without ARs. Our results suggest that the main difference relies on the mean IVT magnitude. We look into the individual time frames of these two composites and observe that they typically occur around the same dates. Together with the similarity in the meteorological state, our results suggest that our ARDT fails to detect those

events. Future studies could benefit from an ARDT specifically tuned for lower latitudes.

5.2 Future Work and Recommendations

We believe that the methodology developed in Chapters 2 and 3 can provide statistical constraints in size and geometry for the AR detection and tracking algorithms. Additionally, we aim to provide an objective insight into the AR size change under climate change. More research needs to be done to understand these changes better. We recognize that some of our methods are not ideal for more geometrically complicated ARs. We propose exploring the use of non-linear principal component analysis to increment the range of ARs that could be analyzed using our methods. We recognize that those different ARDTs are designed with different objectives, and we speculate that they could be detecting different parts of the AR. Our results show that, in fact, we can obtain different estimated sizes depending on the treatment of the IVT background field. We propose to use the results found in this work to aid in the definition of new terms like"AR core", "dynamical envelope', and "thermodynamic envelope". We also propose using these results in the design of a Lagrangian dynamics-based ARDT. The lower AR size range result dissertation could help to reduce the rules and threshold used in the Lagrangian ARDT.

We want to raise special attention to the treatment of the background IVT in climate studies. We observe that the inter-model variance of IVT background is higher than the change between historical and future simulations. Moreover, there is a constant increase in IVT background with time thorough the 1950-2100 period. Therefore, any future work must be aware of these facts to interpret the results correctly.

We propose using the AR size estimation methods in the CWM ARs. This could help answer how similar or different these are from the more studied mid-latitude ARs. Moreover, the use of ARDTs tuned for tropical latitudes could help study the winter precipitation in CWM and other regions around the world. The closer to the equator we are, the higher IVT background noise we encounter, mainly due to the presence of the ITCZ. We understand that this is not an easy task. However, we are sure that the development of more ARDTs capable

of tropical AR detection would help quantify the detection uncertainty, which could help in understanding tropical AR, their impacts, and their relationship with higher latitude ARs.

For future work, we propose to explore the possible link between AR size and duration and how the size of AR might be directly related to hydrological impacts over landfalling regions. We believe that including AR size in the AR categorization scale would provide a broader meaning to the scale. In addition, incorporating size could improve the already helpful AR categorization index in forecasting and preventing AR impacts over land.

Lastly, we need to extend the work of Chapter 4 to other precipitation datasets, reanalysis, and coupled models, such as those in CMIP5/6. We need to understand the nature of the waves creating these AR-like events and extreme precipitation and their relationship with large-scale climate patterns (ENSO, PDO, AMO, MJO). There is still a lot we do not know about ARs in the near-tropics, particularly their non-linear response to climate change. Since dynamical and thermodynamical effects drive IVT changes, it is possible that although ARs' contribution to the CWM (and other tropical regions) total precipitation is low, this might not be the case for a warmer world.

Appendix A

Supporting information for "Constraining and Characterizing the size of Atmospheric Rivers: A perspective independent from the detection algorithm"

In this Appendix, we present a deeper insight into the AR size estimation methods' construction and characteristics. We also present the sensitivity analysis of three of our AR size estimation methods: Statistical Overlapping of IVT With the Background Field PDF (SO), K-S Statistics Between AR Composite and the Background CDF (BG), and Lagrangian tracers method (LT). For reference, Table A.1 shows the labels in Figure 1 from the main text to the respective ARTMIP detection and tracking algorithm used to calculate AR area in Figures 1.2 and 2.1.

A.1 Principal Components Size Estimation Method (PC)

Applying principal components to a complex field such as IVT is a complicated task. As described in section 2.4.1, to isolate the AR object from the IVT far-field, we use a three-step iterative process. First, we filter the ITZC large contiguous regions of high IVT with a two-dimensional Gaussian filter:

$$\mathrm{IVT}' = \mathrm{IVT} \cdot (1 - \mathrm{e}^{\frac{-y^2}{2\Delta y^2}}), \tag{A.1}$$

where IVT'(x, y) is the filtered IVT field, x and y are the longitude and latitude, respectively, and Δy is half-width at half-maximum of the filter. We use $\Delta y = 15°$, which effectively damps the IVT to zero within the ITCZ. Figure A.1 shows an original (a) and filtered (b) IVT field. Then, from the AR object tracking algorithm, we approximate the location of the AR and

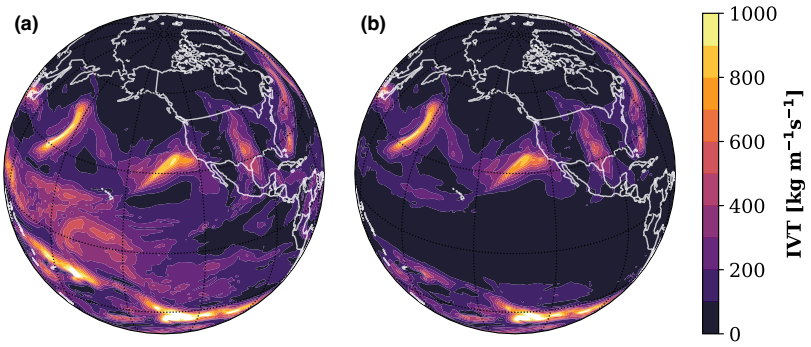

Figure A.1: (a) Original integrated vapor transport (IVT) field; (b) IVT after application of the Gaussian filter in Equation (A.1) with $\Delta y = 15°$ tropical filter (IVT').

determine the AR "core" as the points where IVT is greater than 0.5 times the local maximum IVT. Next, we apply PCA to the AR core and use the eigenvalues and eigenvectors to create a 2D Gaussian function using Equation (11) in Chapter 2. Then, we filter all the points from the original ERA5 IVT field where the core Gaussian function is less than 10^{-3} (we found this value worked well for the ARs objects analyzed in this work). We then apply PCA to the filtered IVT field and use the results to estimate the size of the AR object. Figure A.2 shows three examples of the process. Figure A.2 shows three cases where the process works

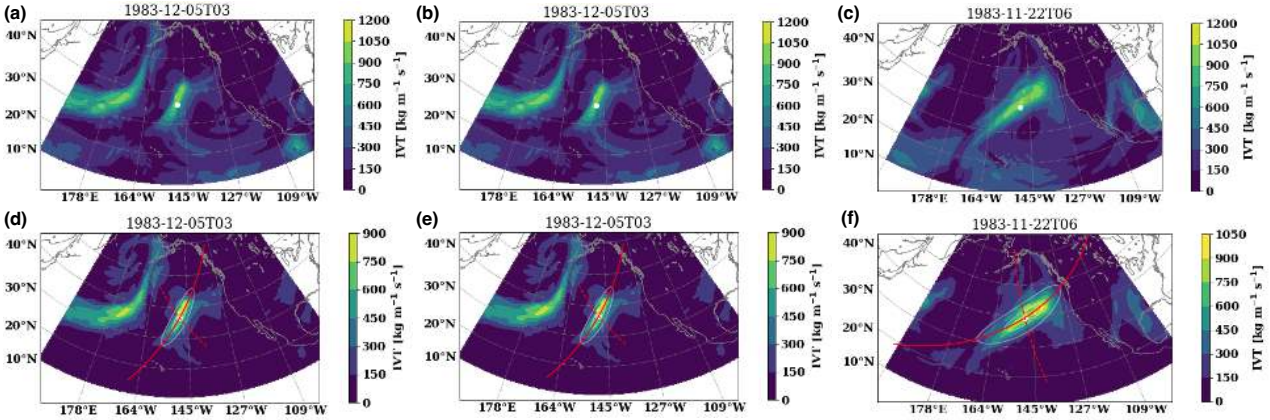

Figure A.2: Illustration of the steps in the PC calculation. The top sub-figures show the original IVT field in filled contours, with a white circle marker as the first guess of AR location (from the tracking algorithm). The bottom sub-plots show the filtered IVT field in color-filled contours, the AR core ellipse and the principal components ellipse in transparent white contours, and the direction of the eigenvectors in red lines.

very well, this is not always the case. For example, merging ARs, or ARs objects with higher curvature in their geometry tend to fail in the PC calculations. We found that for this work, less than 10% of the AR objects failed in the calculation. Those cases were not included in

the composites. Figure A.3 shows three cases with characteristics that are not ideal for the PC analysis. Those three cases in particular did not fail, but the size estimation is not as well performed compared to cases like those in Figure A.2. We hypothesize that using non-linear

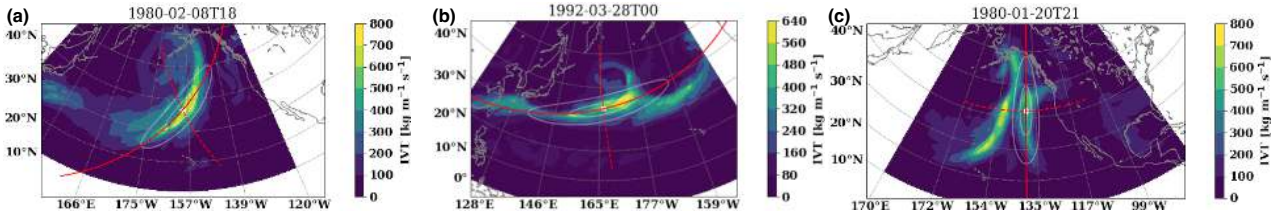

Figure A.3: Illustration of three cases where the PC calculation is more complicated. AR objects with high curvature and merging ARs are particularly challenging. IVT field is shown in color-filled contours and the direction of the eigenvectors in red lines.

principal component analysis could help with the highly curved ARs, but we leave this for future work's exploration.

In the full composite, there are well-behaved and complex cases. Nevertheless, once we leave out the cases where the PC analysis and IVT sampling along the direction of the eigenvectors failed, the obtained composite is quite resembling of the AR structure (Figure A.4). The final composites have 1,150 and 980 AR objects for the WP and EP, respectively.

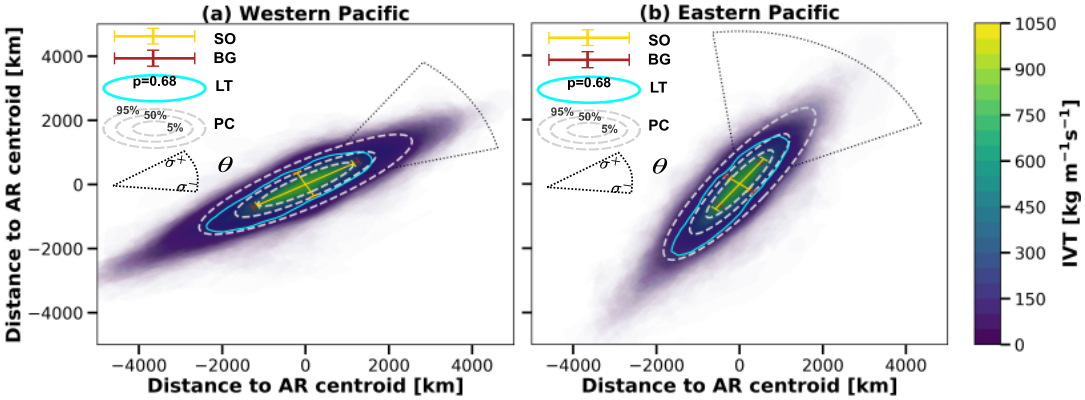

Figure A.4: Summary of the results and graphical illustration of the different size estimation methods. In color contours, we superimpose (with transparency of 0.1%) the IVT field of all the AR objects available at 50% life cycle for (a) Western Pacific and (b) Eastern Pacific.

A.2 Statistical methods (SO and BG)

For each AR object in the composite, we sample IVT in the directions of the principal components and calculate the distance of each point to the AR centroid. One example of this process is illustrated in Figure A.5. We obtain a series of IVT values and their correspondence distance to the AR centroid, along and across the AR object (left and right bottom figures). We apply this sampling technique for all AR objects and get a "raw-sampled" IVT *vs* distance to the AR centroid composite (left panel in Figure A.6) We utilize `fastKDE`[1] (O'Brien et al.,

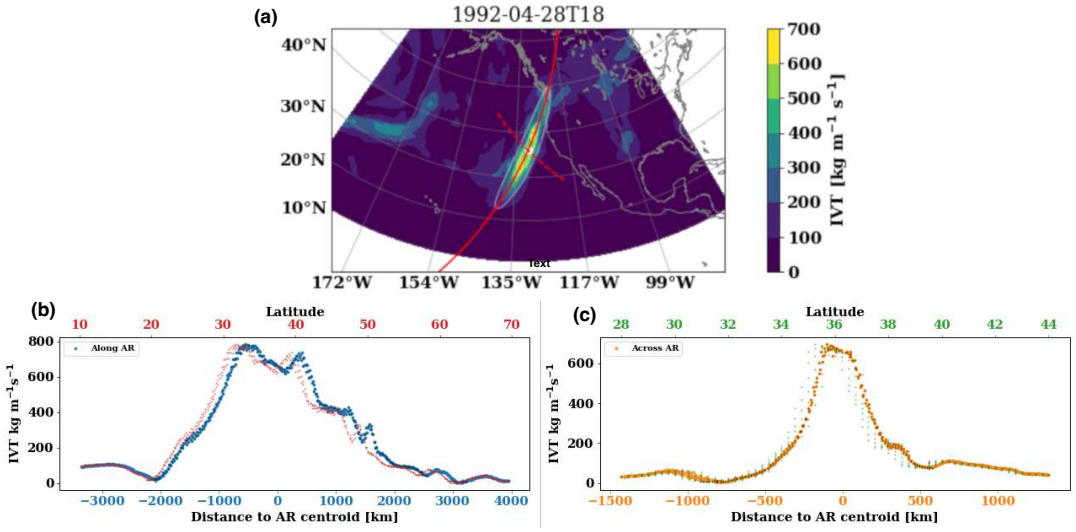

Figure A.5: Illustration of one AR object IVT sampling along the principal components' direction.

2014, 2016) to calculate the conditional probability distribution (CPD) of IVT with respect to the distance to the AR centroid. CPD is the base for the statistical methods the statistical overlapping (SO) and the background KS-test (BG) methods. Figure A.5(a) shows the CPD for one composite. From the calculated CPD, we extract the CPD=0.16 contour (orange line in Figures A.5(b) and A.7(a)). SO method defines the statistical boundary of the AR composite as the distance at which the background IVT probability density function (PDF) IVT_{BK} at plus one standard deviation σ^{+1} (dotted line in Figure 3.2(b)) intersects the composite CPD at minus one standard deviation σ^{-1} (CPD=0.16). We can interpret this point as the distance at which the background IVT PDF at σ^{+1} overlaps with the AR composite

[1] `https://github.com/LBL-EESA/fastkde/releases/tag/v1.0.18`

CPD=0.16, represented by the dashed blue line in Figure A.7(a). The BG method compares

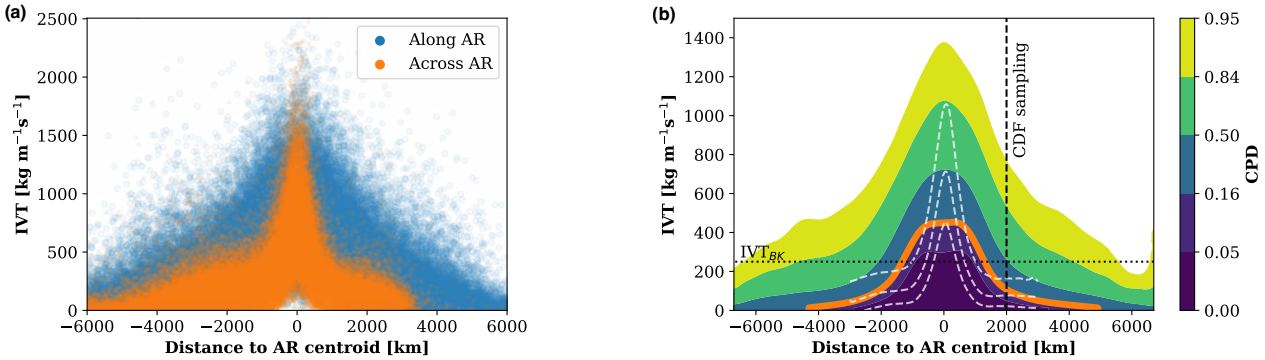

Figure A.6: (a) Raw sampling of IVT *vs* distance to the AR centroid. (b) Conditional probability distribution of IVT and distance to the AR centroid along the AR composite (white contours show CPD across AR composite). The orange contour represents the 0.16 probability contour. Vertical dashed line shows how we would sample to generate the cumulative density function at a given distance.

the AR composite and the background IVT cumulative distribution function (CDF). To calculate the CDF of the composite as a function of the distance to the centroid, we sample the CPD at specific distances, represented by the dashed line in Figure A.5(a). From the CPD, we can calculate the composite CDF at different distances from the AR centroid. BG method is based on the hypothesis that near the AR centroid, the ARs composite CDF is very different from the background (circle markers in A.7). Furthermore, the composite CDF must become more similar to the background CDF as we move away from the AR centroid (triangle markers in Figure A.7(b)). We use a two-tailed Kolmogorov–Smirnov test (KS-test) to determine the distance at which the composite and background IVT fields become indistinguishable.

A.3 Sensitivity analysis: BG and SO methods

We calculate a sensitivity test for the Statistical overlapping of AR composite conditional probability distribution of IVT given the distance to the AR center and the PDF of the background IVT field (SO), and the comparison of the IVT cumulative distribution function (CDF) of AR composite with the CDF of the background IVT field (BG) method.

For the SO method, we vary the overlapping PDF intersection value to define the AR composite size: the background IVT PDF value σ^{-} from 0.05 to 0.5, and the conditional

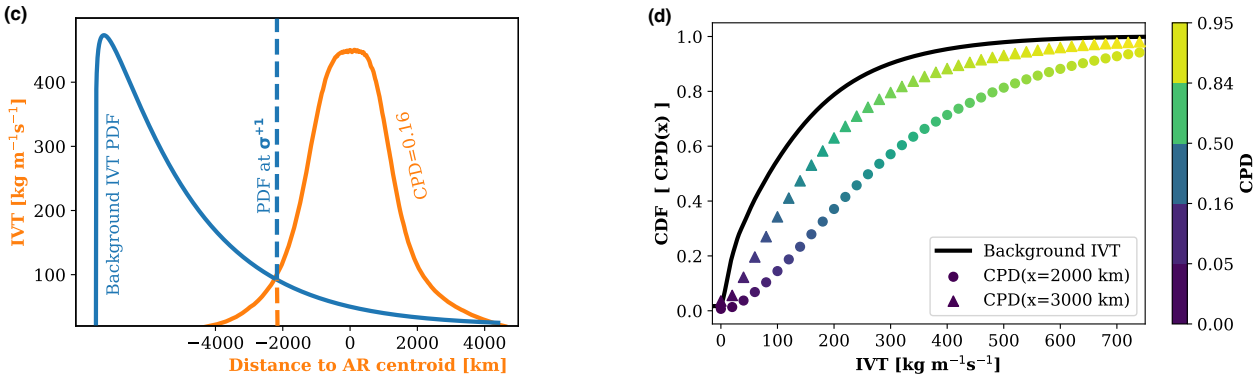

Figure A.7: (a) Illustration of the statistical overlapping method. Blue line shows an sketched background IVT PDF. The orange line is the CPD=0.16 (from panel b). (c) Illustration of two CDF at different distances from the AR composite center. CDF are obtained sampling vertically from the CPD (panel b). Circle markers represent a closer distance to the composite center than the triangle markers.

probability distribution (CPD) value of the AR IVT composite σ^+ from 0.95 to 0.5. The values used to calculate the results shown in the main text are σ^-=0.16 and σ^+=0.84.

For the BG method, we test the sensitivity of the one-tailed Kolmogorov–Smirnov test by varying the p-value used to estimate the size of the AR composite, from $p = 0.80$ to $p = 0.99$.

Figures A.8(a-b) and A.8(c-d) show the results of these sensitivity tests for the Northwest (WP) and Northeast Pacific (EP) ARs at 50% life cycle. Similar results 25% and 75% of the AR life cycle.

It is important to notice that the dependence on the free parameters for the SO and BG methods is as expected. SO dimensions and areas should increase as σ^- decreases and σ^+ increases (so the AR becomes "indistinguishable " from the background). This is shown in Figure A.8(a-b). Moreover, in the BG method areas should decrease as p increases (a more stringent condition), as Figure A.8(c-d) shows.

A.4 Lagrangian tracers method (LT) sensitivity analysis

We explore the sensitivity the LT method to the stochastic component and the scaling of the horizontal-velocity used for the velocity used for tracer advection. We calculate the

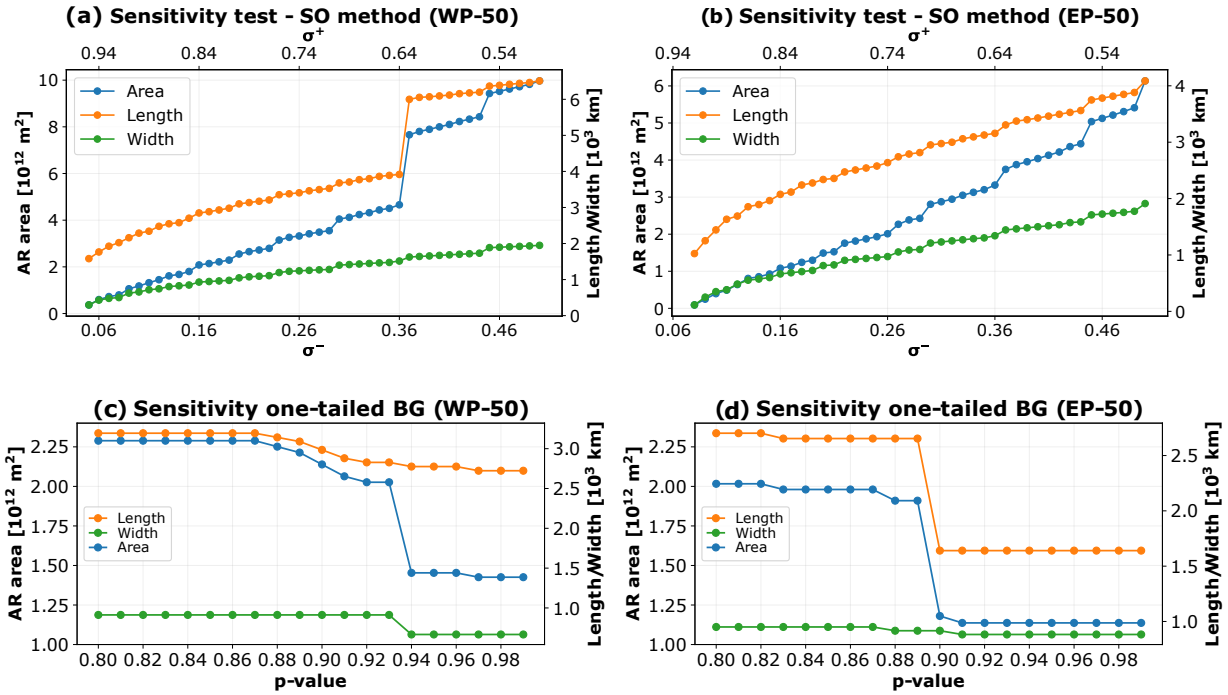

Figure A.8: WP (a) and EP (b) sensitivity background for the one-tailed KS-test method (BG). AR area is shown in blue (left vertical axis). AR length and width are shown in orange and green, respectively (right vertical axis). p is the statistical significance level for the one-tailed KS-test. The results presented in the main text of this work are generated using $p = 0.95$. WP (c) and EP (d) sensitivity test for the statistical overlapping method (SO). σ^- and σ^+, are the PDF value of the IVT background and the CPD value of the IVT composite with distance, respectively. AR area is shown in blue (left vertical axis). AR length and width are shown in orange and green, respectively (right vertical axis). The results presented in the main text of this work are generated using $\sigma^- = 0.16$ and $\sigma^+ = 0.84$.

trajectory of the tracers using a modification of Equation (10) from the main text of this work

$$dx_i = (u_i + \alpha\sqrt{2}\overline{u}_i\, w_i)\, dt, \tag{A.2}$$

where we use the parameter α to modify the magnitude of the scaling velocity, from 1/8 times $\sqrt{2}\overline{u}_i$ to 4 times $\sqrt{2}\overline{u}_i$ ($\alpha = 1$ represents the value used to calculate the results shown in the main text of this work).

Additionally, we vary the PDF threshold value used to define the AR area from $p = 0.4$ to $p = 0.93$, where $p = 0.68$ represents the value used to estimate the AR area for the results of this work.

Figure A.9 shows the sensitivity test results for WP and EP AR composites at 50% life

cycle. Similar results 25% and 75% of the AR life cycle.

Results for the LT sensitivity test are as expected. Increasing p should decrease the area for a given value of alpha, as shown in Figure A.9. The increase in area for a given p value is certainly plausible – in the limit of $\alpha \to \infty$, the sample points from the AR should insteadly spread over the whole globe after the first time step, thereby maximizing the area.

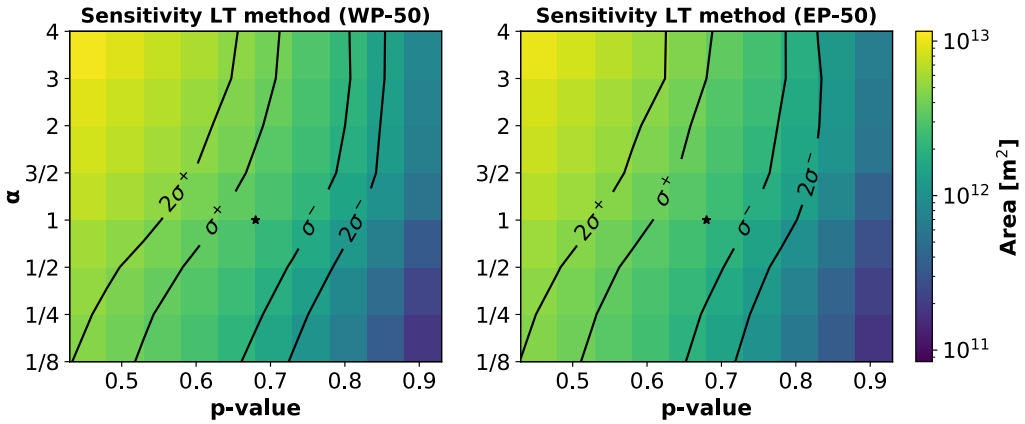

Figure A.9: Sensitivity test for the Lagrangian tracers method (LT). Colored contours show AR area, α is the multiplication factor of the scaling velocity $\sqrt{2\overline{u_i}}$ from equation (A.2), and p-value is the final tracer position PDF value at which we define the AR size. Black contours represent -2, -1, 1, and 2 standard deviations of the AR area calculated using the LT method (from main text Figure 1). The black star represents $\alpha = 1.0$ and $p = 0.68$, which are the values used to calculate the main work results.

A.5 ARTMIP algorithms used in Chapter 1 analysis

For reference, we include table A.1 that describe the algorithms used to generate Figures 1.2 and 2.1.

Table A.1: List of ARTMIP algorithms used to generate Figures 1.2 and 2.1

Label	Algorithm name
01	Lavers
02	PNNL_AR_detection_ALG#2_v1
03	wille_IWV
04	Brands_v3
05	Tempest_T2CNTL
06	CASCADE_IVT
07	tempest_ivt250
08	tempest_ivt700
09	tempest_ivt500
10	CASCADE_IWV
11	Payne_Magnusdottir
12	wille_vIVT
13	Gershunovetal2017_v1
14	PNNL_AR_detection_ALG#1_v1
15	Reid500
16	Mundhenk_v3
17	Guan_Waliser_v2
18	TDA_ML
19	Walton_v1
20	SAIL_v1
21	Rutz
22	Lora_v2
23	Reid250
24	PanLu
25	Viale_SAmerica
26	Goldenson_v1-1
27	cascade_bard_v1
28	ARCONNECT

Appendix B

Supporting information for Chapter 3

B.1 Calculation of ARCI

In this section we asses the ARTMIP algorithms used to calculate the atmospheric river confidence index (ARCI), and their classification based on their treatment of thresholds. Additionally, we briefly review the issues in the process of ARCI calculation, such as missing and corrupt data in the CMIP5/6 and ARTMIP tier 2 catalog.

B.1.1 Global ARTMIP ARDTs

Table B.1 shows the six global ARDTs used in this, their contributors, and references. AR detections are part of the ARTMIP tier 2 CMIP5/6 experiment. ARTMIP Tier 2 CMIP5/6 catalogs can be found on the Climate Data Gateway[1]. We thank all the contributors to the ARTMIP tier 2 experiment.

Table B.1: Global ARTMIP Tier 2 CMIP5/6 experiment ARDT algorithms used to calculate the atmospheric river confidence index (ARCI).

ARDTs		
Algorithm ID	Contributor	DOI/Reference
ARCONNECT_v2	Shearer et al.	doi.org/10.1029/2020JD033425
GuanWaliser_v2	Guan and Waliser	doi.org/10.1002/2015JD024257 doi.org/10.1175/JHM-D-17-0114.1
Lora_v2	Lora et al.	doi.org/10.1016/j.epsl.2020.116293
Mundhenk_v3	Mundhenk	10.1175/JCLI-D-15-0655.1
Tempest	McClenny et al.	doi.org/10.5194/gmd-10-1069-2017 doi.org/10.1029/2020JD033421
TECA_BARD_v1.01	O'Brien et al.	10.5194/gmd-13-6131-2020

[1] https://doi.org/10.26024/s4p7tt9f13

B.1.2 Classification of ARDTs

We follow O'Brien et al. (2021) classification of ARDTs based on their treatment of thresholds:

Absolute ARDTs use any fixed thresholds (for example, in IVT) for discriminating ARs from the background. `ARCONNECT_v2` uses an absolute threshold in IVT to detect ARs. `Lora_v2` uses an IVT 250 kg $m^{-1}s^{-1}$ above time/latitude dependent threshold using 30-day running mean and zonal average of IWV. Although this threshold varies with latitude and time, it imposes an absolute threshold of 250 kg $m^{-1}s^{-1}$, which is why O'Brien et al. (2021) classifies it as an absolute method.

Fixed relative ARDTs employ relative thresholds that do not vary with time. `Guan_Waliser_v2` discriminates ARs from the background where the IVT is greater than the local, historical 85^{th} IVT percentile. `Mundhenk_v3` identifies ARs in which their IVT anomalies are above the 94^{th} percentile of the historical simulation.

Relative ARDTs employ relative thresholds that vary with time. `TECA_BARD_v1.01` identifies IVT above a fixed percentile of IVT, where the percentile is calculated in space. `Tempest` uses an absolute threshold applied to the Laplacian (which removes the mean of the IVT field) of the IVT field, identifying regions of high IVT relative to nearby IVT at the same timestep.

B.1.3 CMIP5/6 and ARDTs Missing Data

The outputs for historical/future CMIP5/6 simulations were for the 1951-2099 period. CMIP6 IPSL-CM6A-LR SSP5-8.5 simulation are only available through 2049, and there are data corruption issues for the year 2006 in the CMIP5 CSIRO-Mk3-6-0 simulation. Corrupt and missing data are not used in the calculation of ARCI. For most of the CMIP5/6 cases, ARCI is the mean of the six ARDTs, except for NorESM1-M and BCC-CSM2-MR simulations, where `Guan_Waliser_v2` algorithm did not supply ARDT catalogs due to technical issues at the time. The ARCI calculation was challenging. Different ARDTs and models had different

time units, calendars, and different output file frequency. First, we unified time units and calendars, identifying and marking corrupt and missing data. All ARDTs results were saved into new netCDF files, with unified time, calendar, and output frequency. Then, we calculate the mean across ARDTs (ARCI) and apply the Zhou et al. (2018) tracking algorithm to the ARCI for each CMIP5/6. Additional details on the ARDTs and tier 2 experiment design is available in ARTMIP's website[2] and *Increases in Future AR Count and Size: Overview of the ARTMIP Tier 2 CMIP5/6 Experiment* (O'Brien et al., 2021)[3].

B.2 AR Size Supplementary Plots

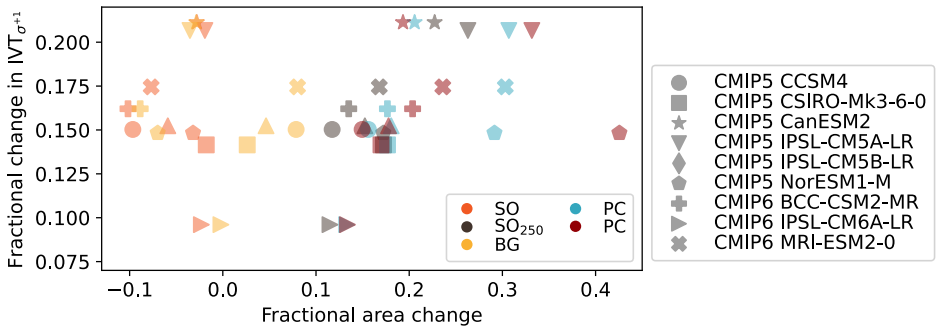

Figure B.1: Fractional change between historical and future simulations in background IVT$_{\sigma^{+1}}$ *vs* fractional change in median AR area. Each CMIP5/6 model is represented by a different marker, colors represent the size estimation method.

[2] https://www.cgd.ucar.edu/projects/artmip/
[3] https://doi.org/10.1029/2021JD036013

Appendix C

Additional Plots for Chapter 4

C.1 Long-term Means

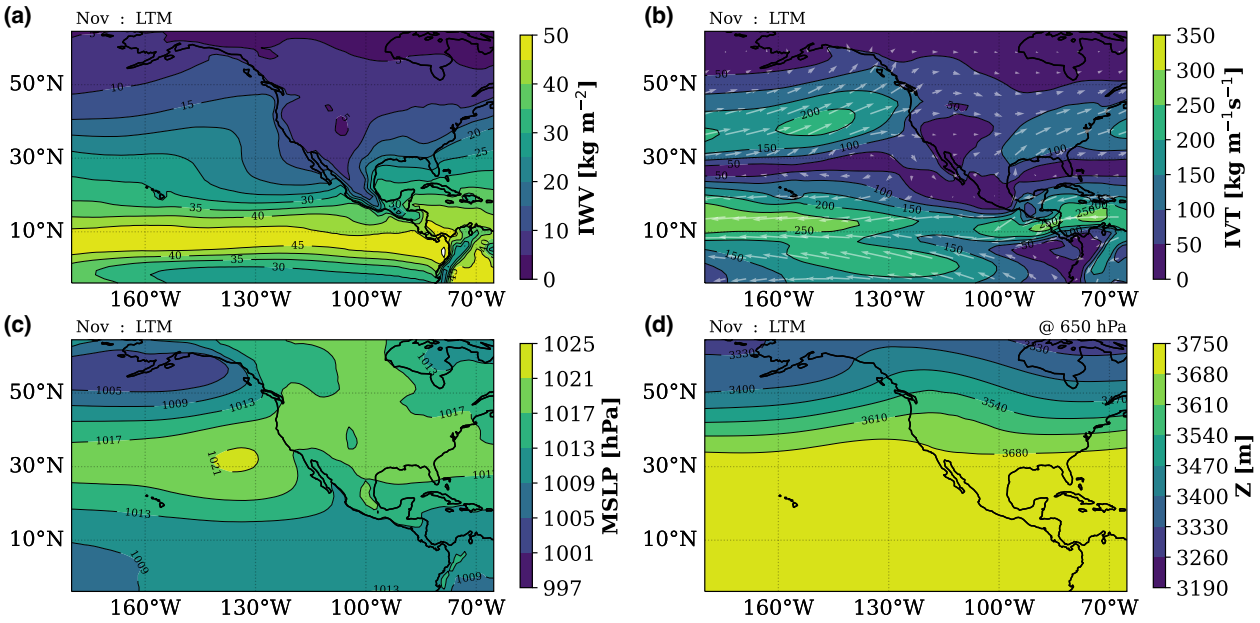

Figure C.1: Long-term mean for 1900-2010. (a) Integrated water vapor (IWV), (b) integrated vapor transport (IVT), (c) mean sea level pressure (MSLP), (d) geopotential height at 650 hPa

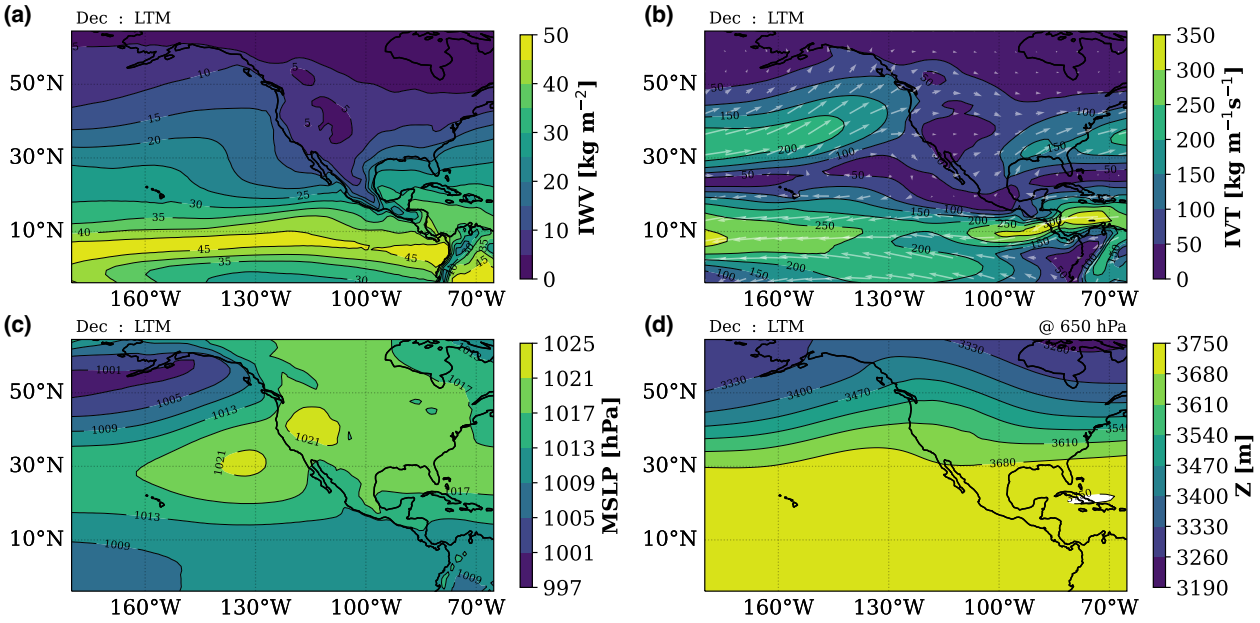

Figure C.2: Long-term mean for 1900-2010. (a) Integrated water vapor (IWV), (b) integrated vapor transport (IVT), (c) mean sea level pressure (MSLP), (d) geopotential height at 650 hPa

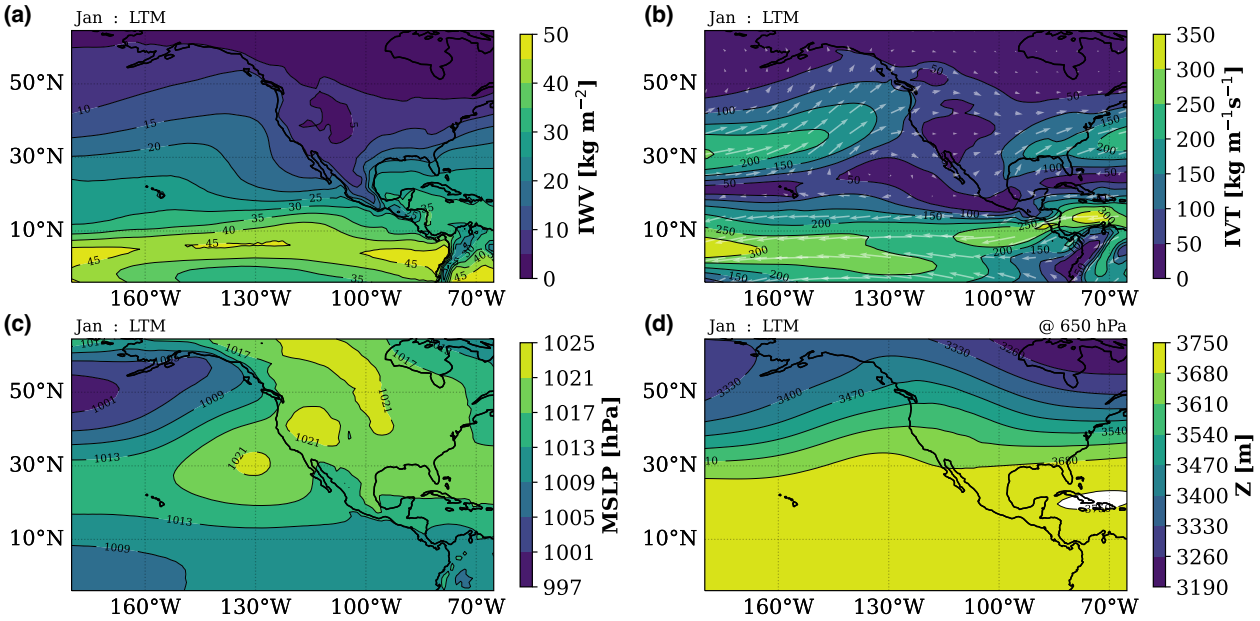

Figure C.3: Long-term mean for 1900-2010. (a) Integrated water vapor (IWV), (b) integrated vapor transport (IVT), (c) mean sea level pressure (MSLP), (d) geopotential height at 650 hPa

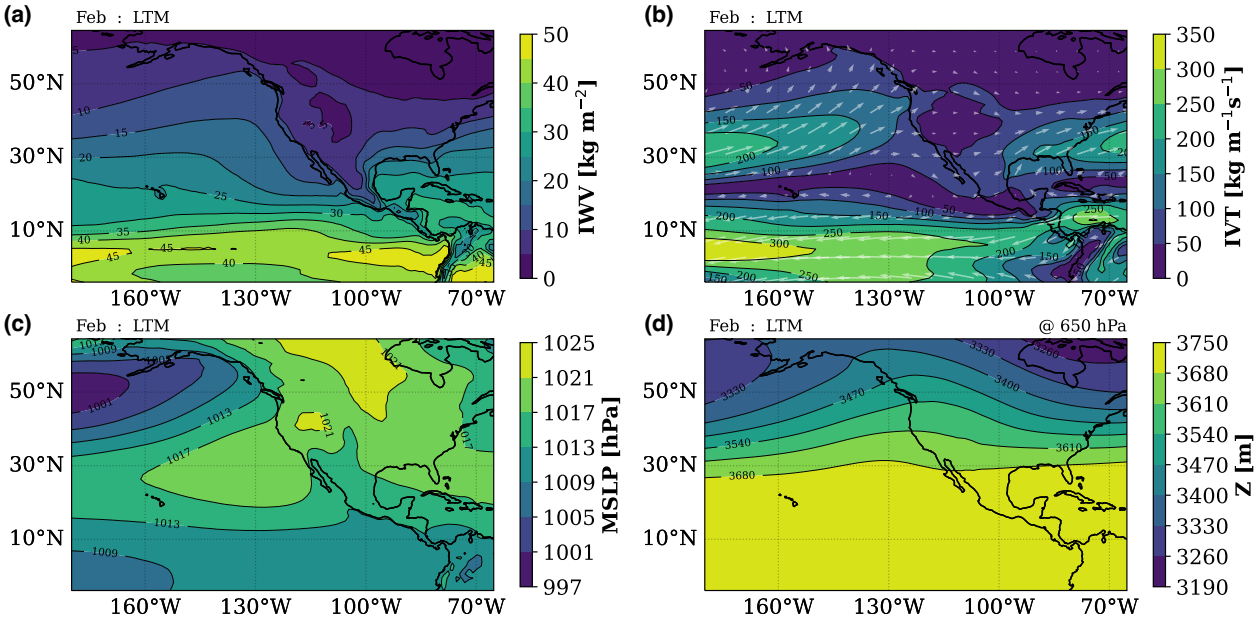

Figure C.4: Long-term mean for 1900-2010. (a) Integrated water vapor (IWV), (b) integrated vapor transport (IVT), (c) mean sea level pressure (MSLP), (d) geopotential height at 650 hPa

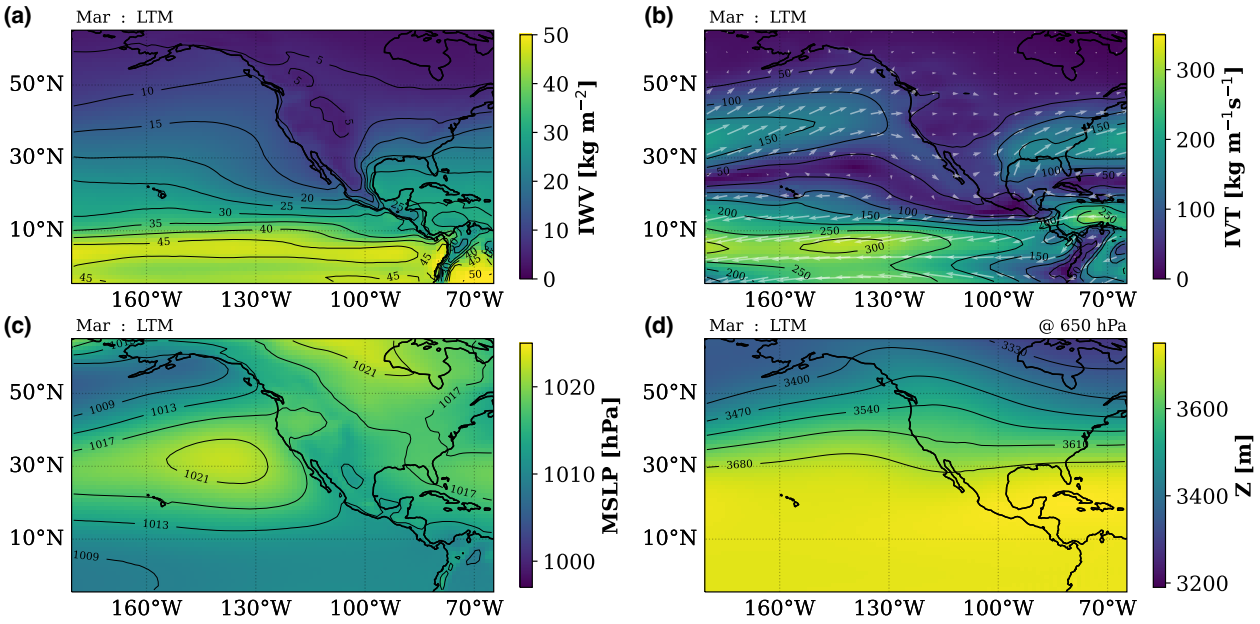

Figure C.5: Long-term mean for 1900-2010. (a) Integrated water vapor (IWV), (b) integrated vapor transport (IVT), (c) mean sea level pressure (MSLP), (d) geopotential height at 650 hPa

C.2 AR-Precipitation Composite

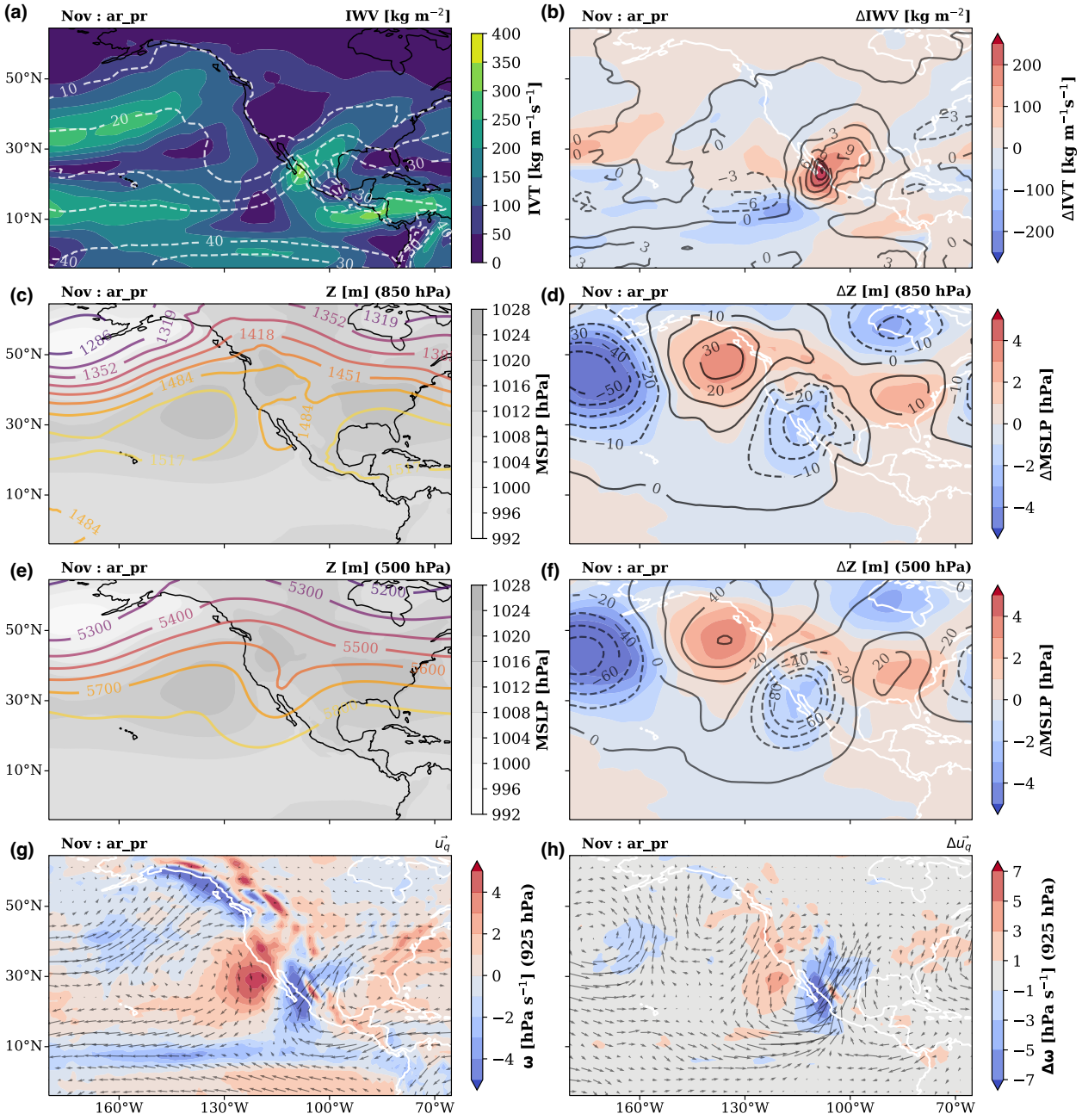

Figure C.6: State of the atmosphere during AR landfalling and extreme precipitation at `Loc1` in November. Black contours variables are specified on the top-right of each plot. Left column: IWV, IVT, mean sea level pressure, geopotential height at 850 and 500 hPA, IVT direction (u_q), and ω at 650 hPa. Right column: anomalies with respect to the long-term mean for the same variables.

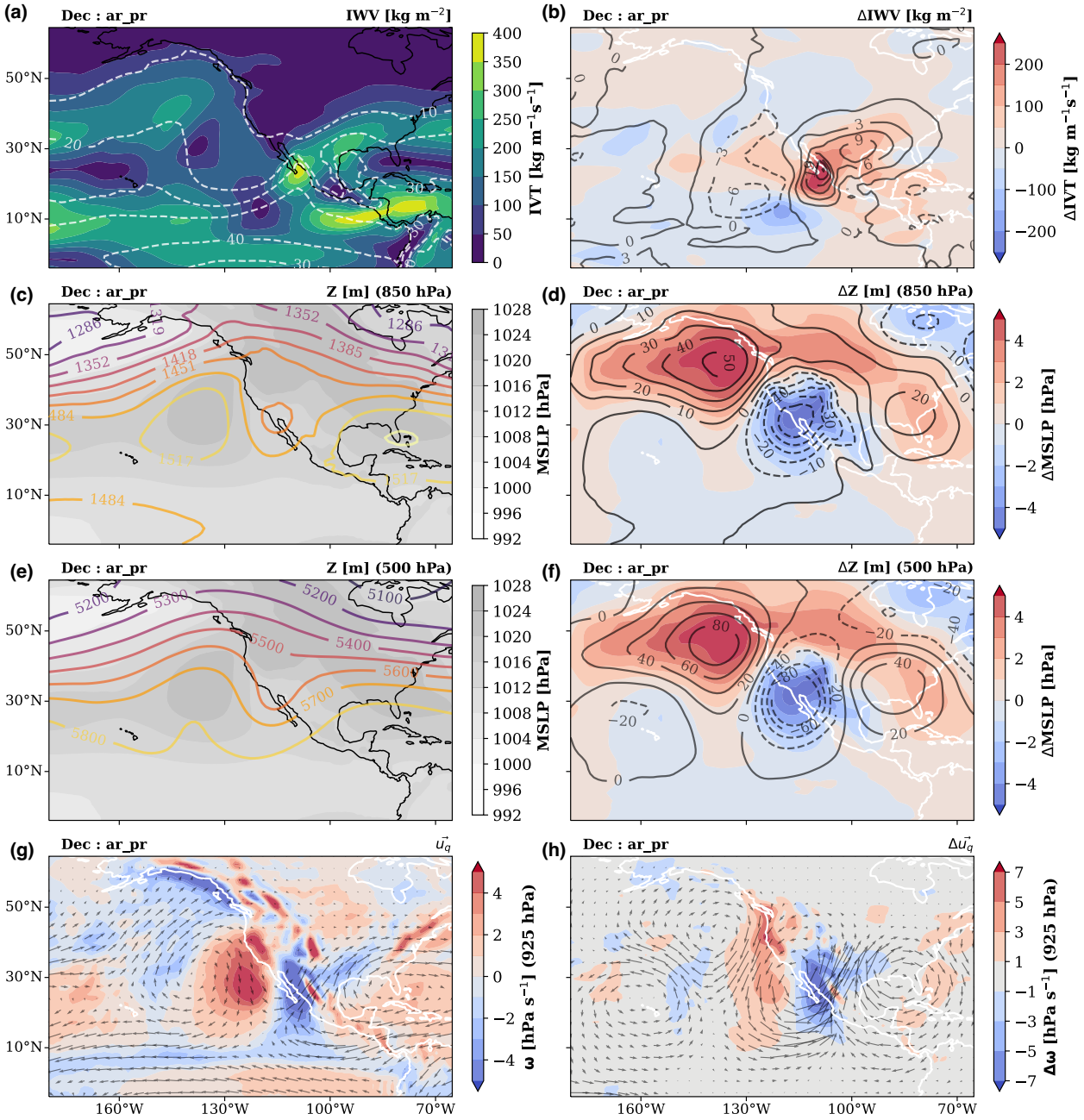

Figure C.7: State of the atmosphere during AR landfalling and extreme precipitation at `Loc1` in December. Black contours variables are specified on the top-right of each plot. Left column: IWV, IVT, mean sea level pressure, geopotential height at 850 and 500 hPA, IVT direction (u_q), and ω at 650 hPa. Right column: anomalies with respect to the long-term mean for the same variables.

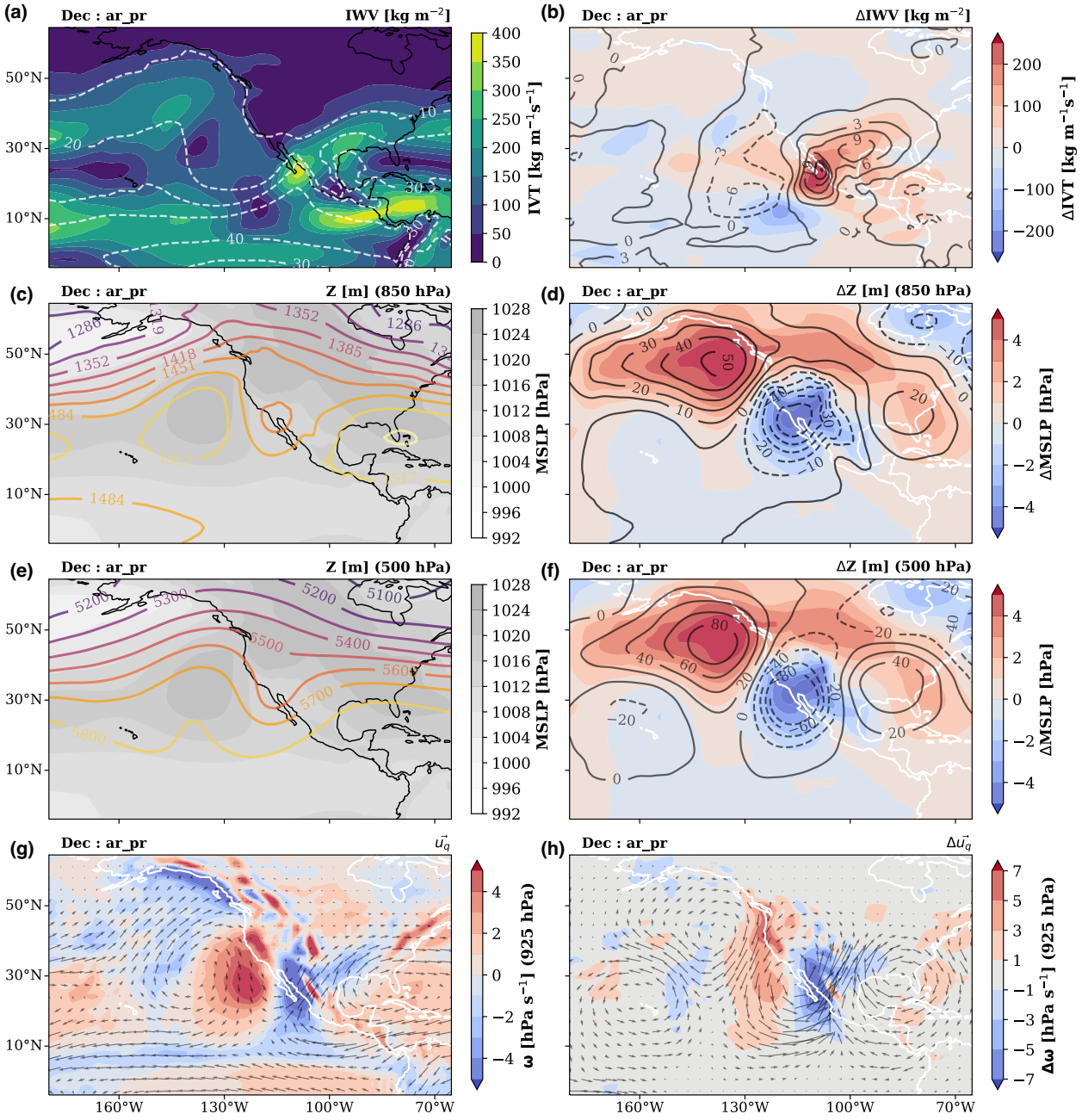

Figure C.8: State of the atmosphere during AR landfalling and extreme precipitation at `Loc1` in January. Black contours variables are specified on the top-right of each plot. Left column: IWV, IVT, mean sea level pressure, geopotential height at 850 and 500 hPA, IVT direction (u_q), and ω at 650 hPa. Right column: anomalies with respect to the long-term mean for the same variables.

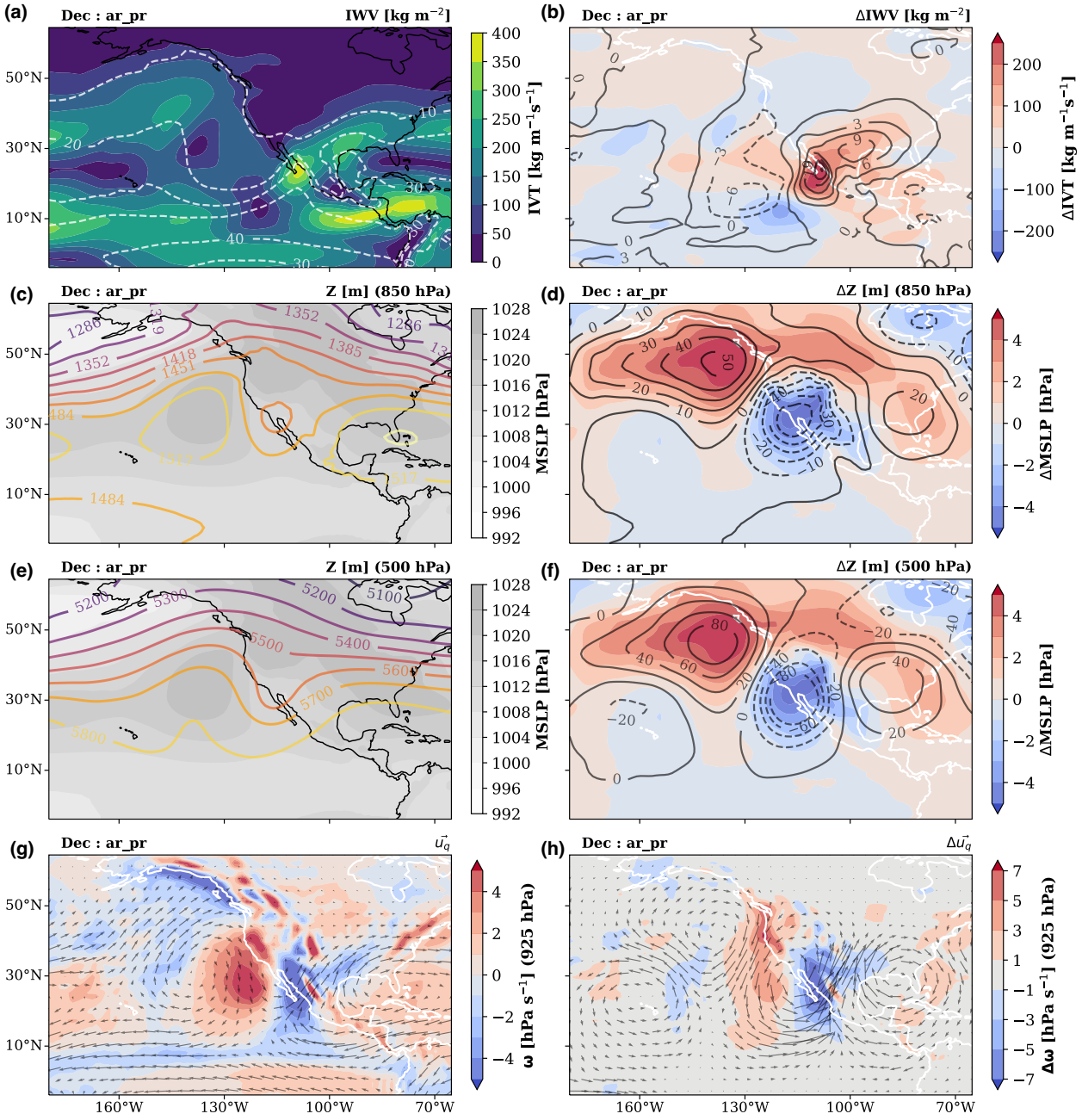

Figure C.9: State of the atmosphere during AR landfalling and extreme precipitation at `Loc1` in February. Black contours variables are specified on the top-right of each plot. Left column: IWV, IVT, mean sea level pressure, geopotential height at 850 and 500 hPA, IVT direction (u_q), and ω at 650 hPa. Right column: anomalies with respect to the long-term mean for the same variables.

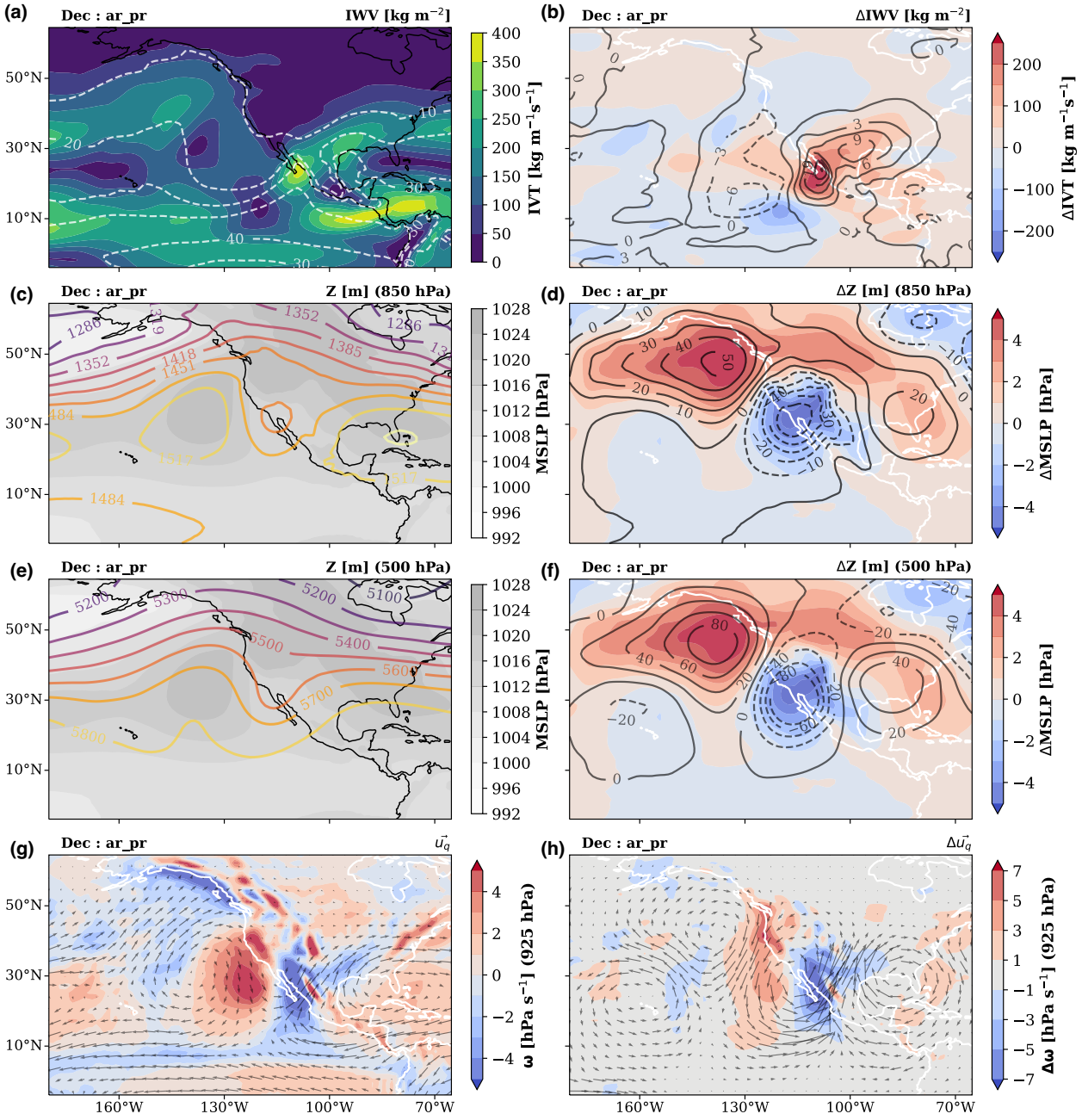

Figure C.10: State of the atmosphere during AR landfalling and extreme precipitation at `Loc1` in March. Black contours variables are specified on the top-right of each plot. Left column: IWV, IVT, mean sea level pressure, geopotential height at 850 and 500 hPA, IVT direction (u_q), and ω at 650 hPa. Right column: anomalies with respect to the long-term mean for the same variables.

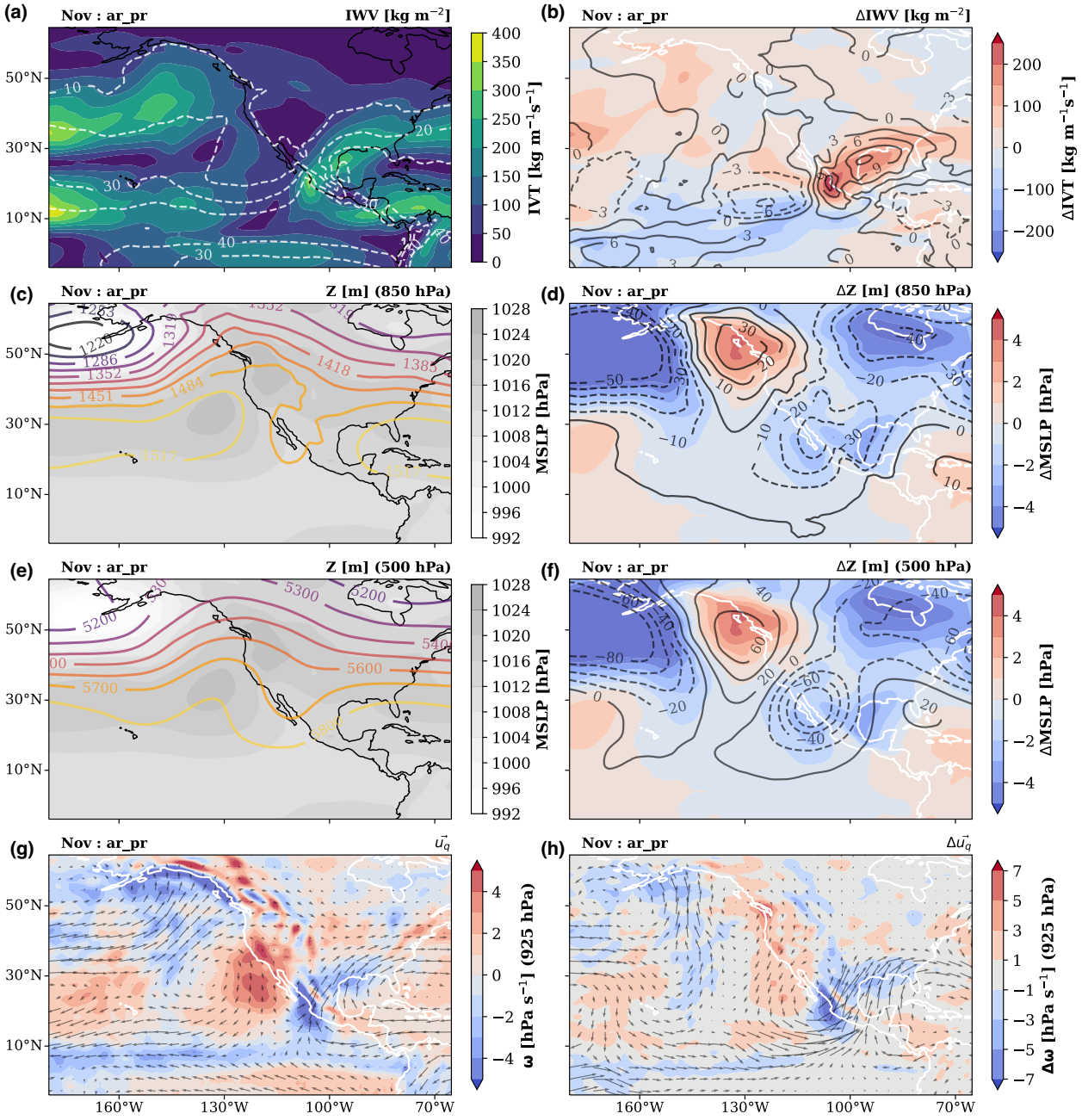

Figure C.11: State of the atmosphere during AR landfalling and extreme precipitation at `Loc2` in November. Black contours variables are specified on the top-right of each plot. Left column: IWV, IVT, mean sea level pressure, geopotential height at 850 and 500 hPA, IVT direction (u_q), and ω at 650 hPa. Right column: anomalies with respect to the long-term mean for the same variables.

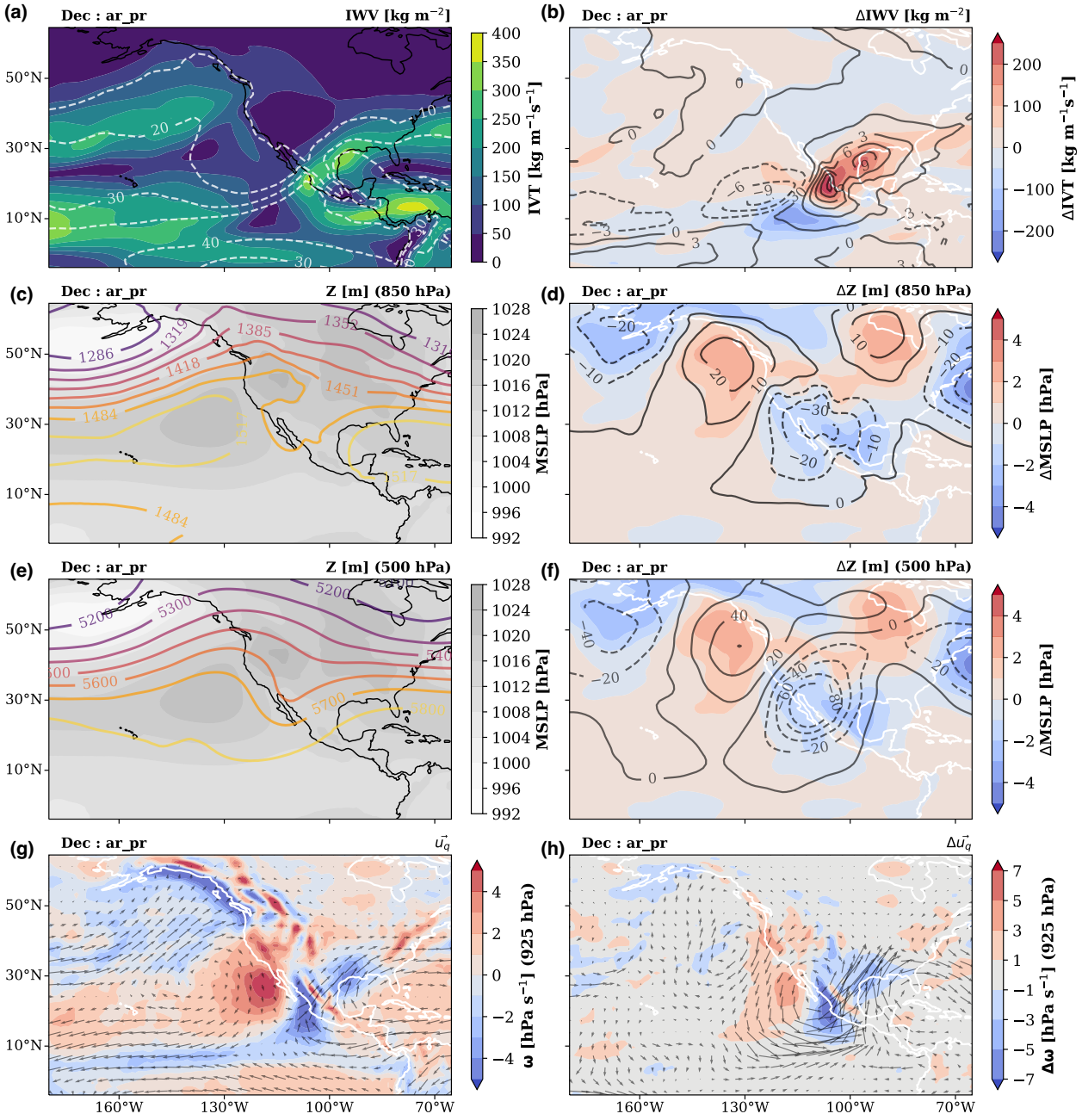

Figure C.12: State of the atmosphere during AR landfalling and extreme precipitation at `Loc2` in December. Black contours variables are specified on the top-right of each plot. Left column: IWV, IVT, mean sea level pressure, geopotential height at 850 and 500 hPA, IVT direction (u_q), and ω at 650 hPa. Right column: anomalies with respect to the long-term mean for the same variables.

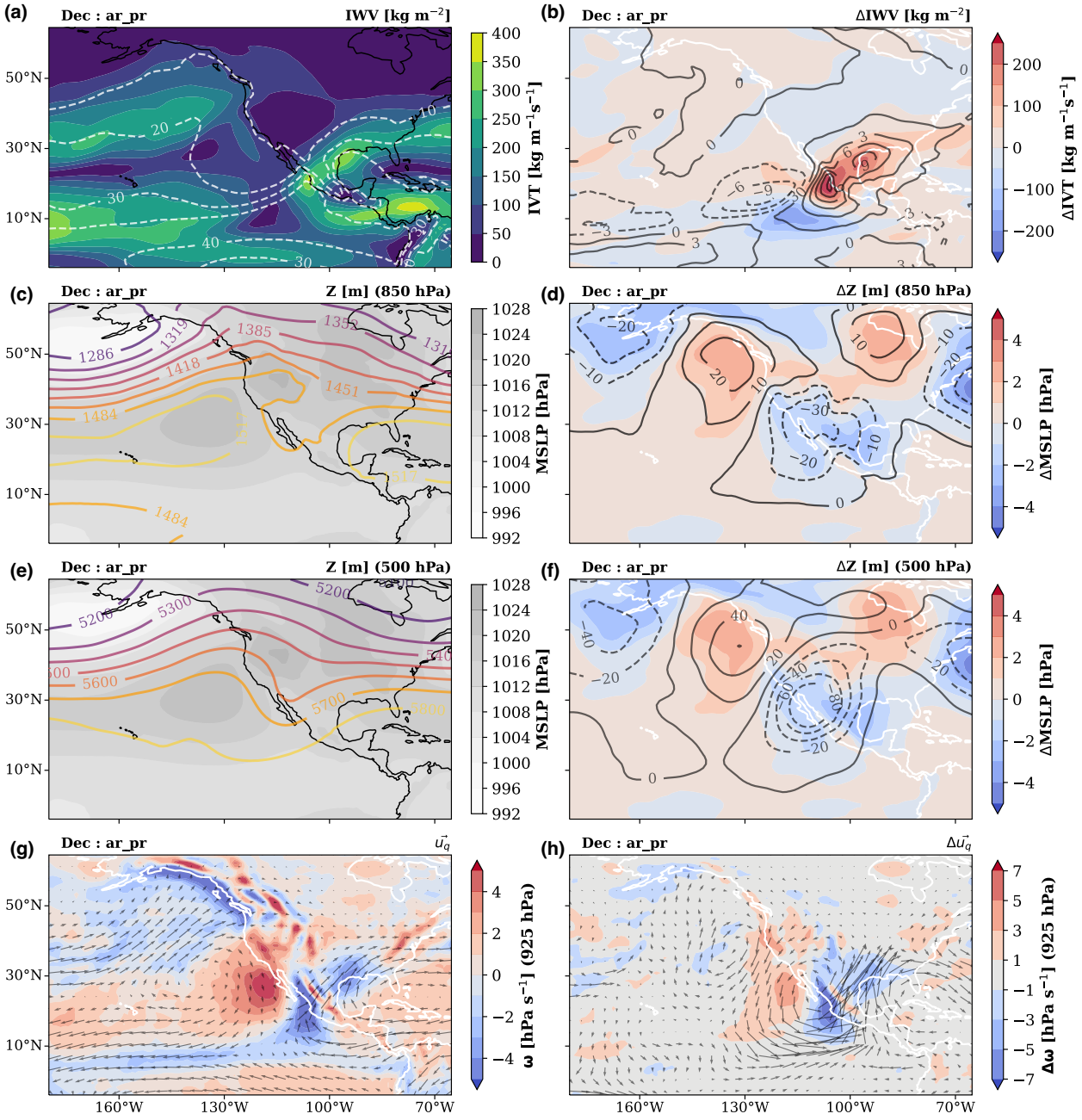

Figure C.13: State of the atmosphere during AR landfalling and extreme precipitation at `Loc2` in January. Black contours variables are specified on the top-right of each plot. Left column: IWV, IVT, mean sea level pressure, geopotential height at 850 and 500 hPA, IVT direction (u_q), and ω at 650 hPa. Right column: anomalies with respect to the long-term mean for the same variables.

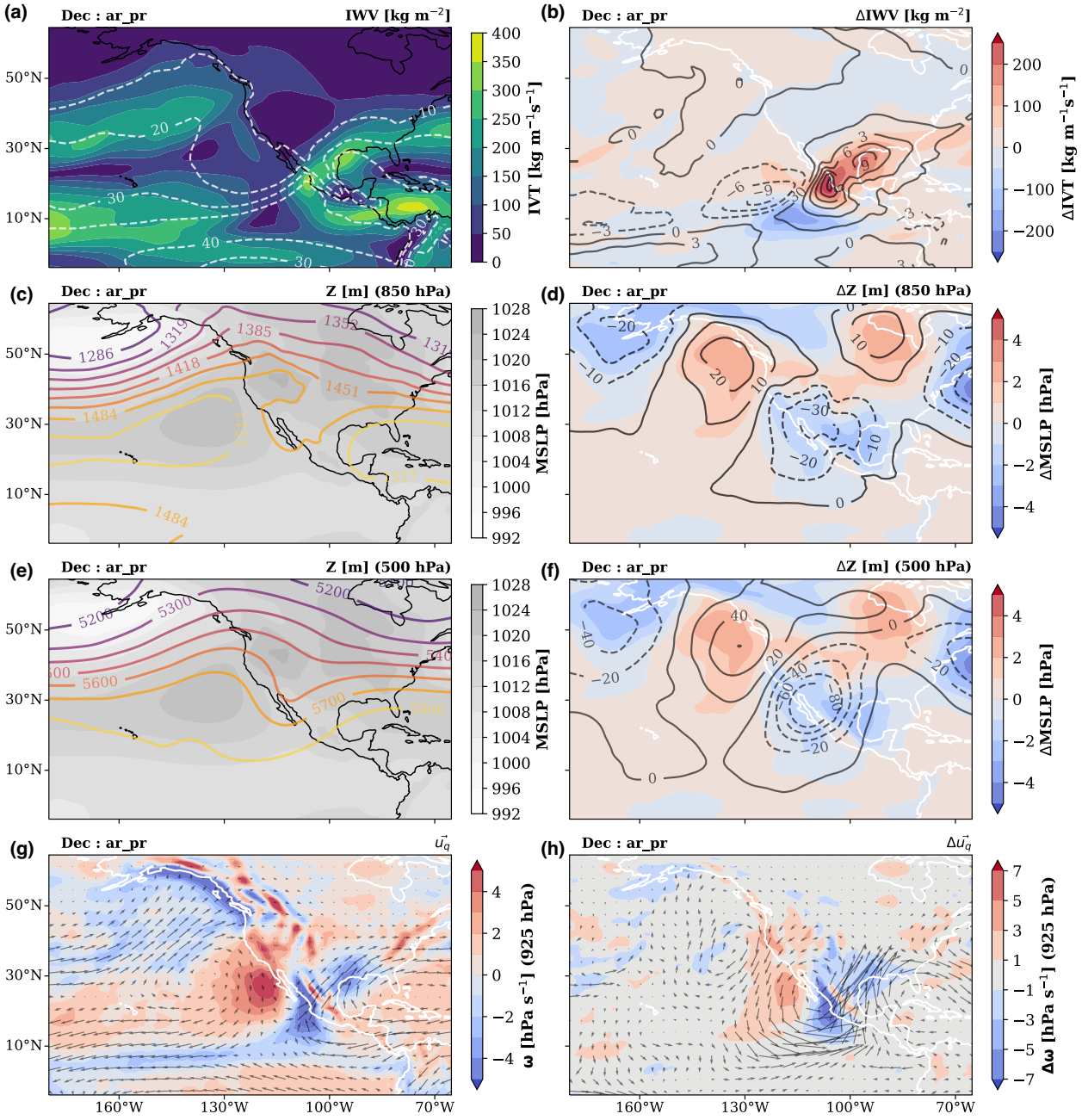

Figure C.14: State of the atmosphere during AR landfalling and extreme precipitation at `Loc2` in February. Black contours variables are specified on the top-right of each plot. Left column: IWV, IVT, mean sea level pressure, geopotential height at 850 and 500 hPA, IVT direction (u_q), and ω at 650 hPa. Right column: anomalies with respect to the long-term mean for the same variables.

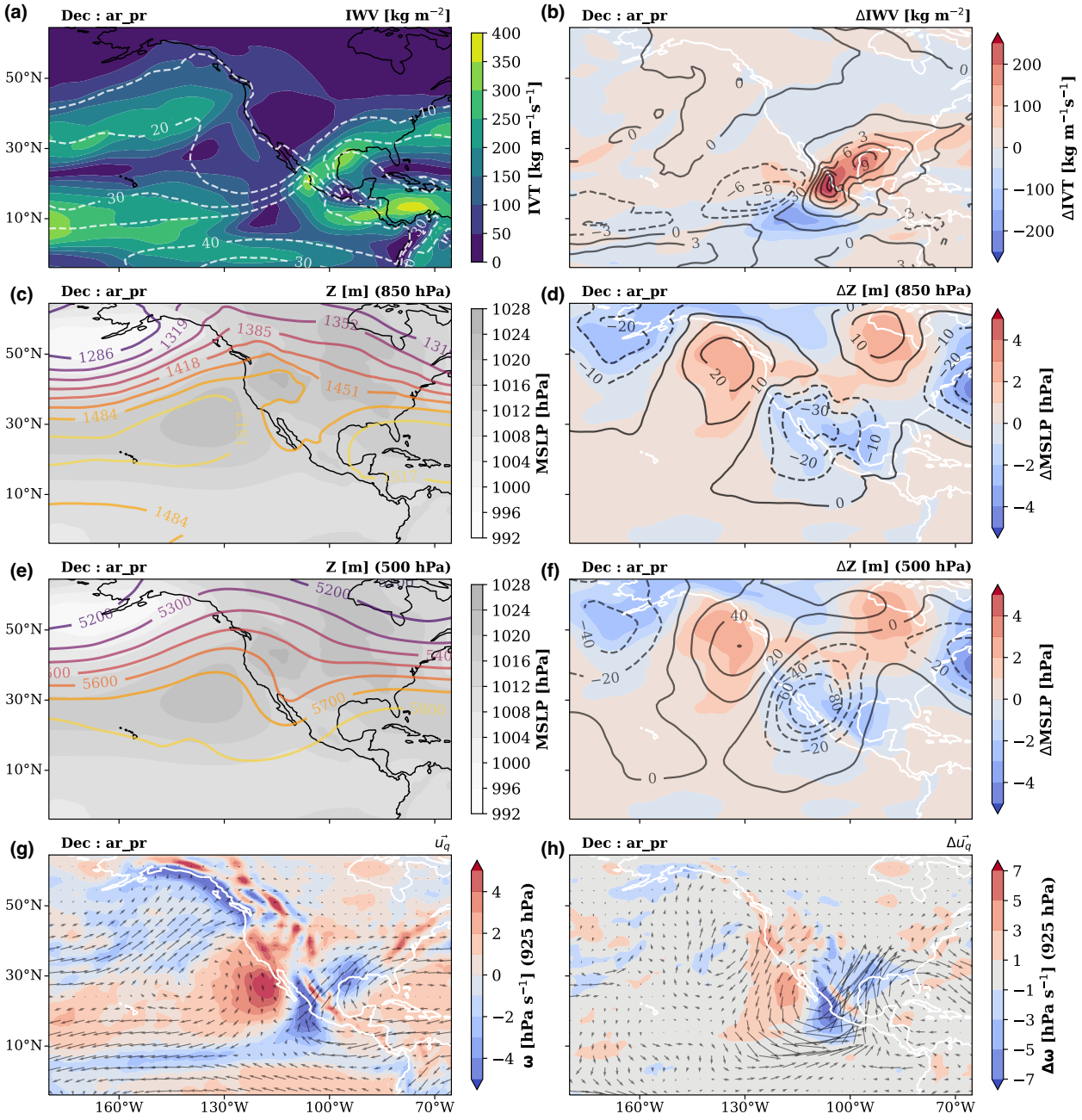

Figure C.15: State of the atmosphere during AR landfalling and extreme precipitation at `Loc2` in March. Black contours variables are specified on the top-right of each plot. Left column: IWV, IVT, mean sea level pressure, geopotential height at 850 and 500 hPA, IVT direction (u_q), and ω at 650 hPa. Right column: anomalies with respect to the long-term mean for the same variables.

C.3 AR+No Precipitation Composite

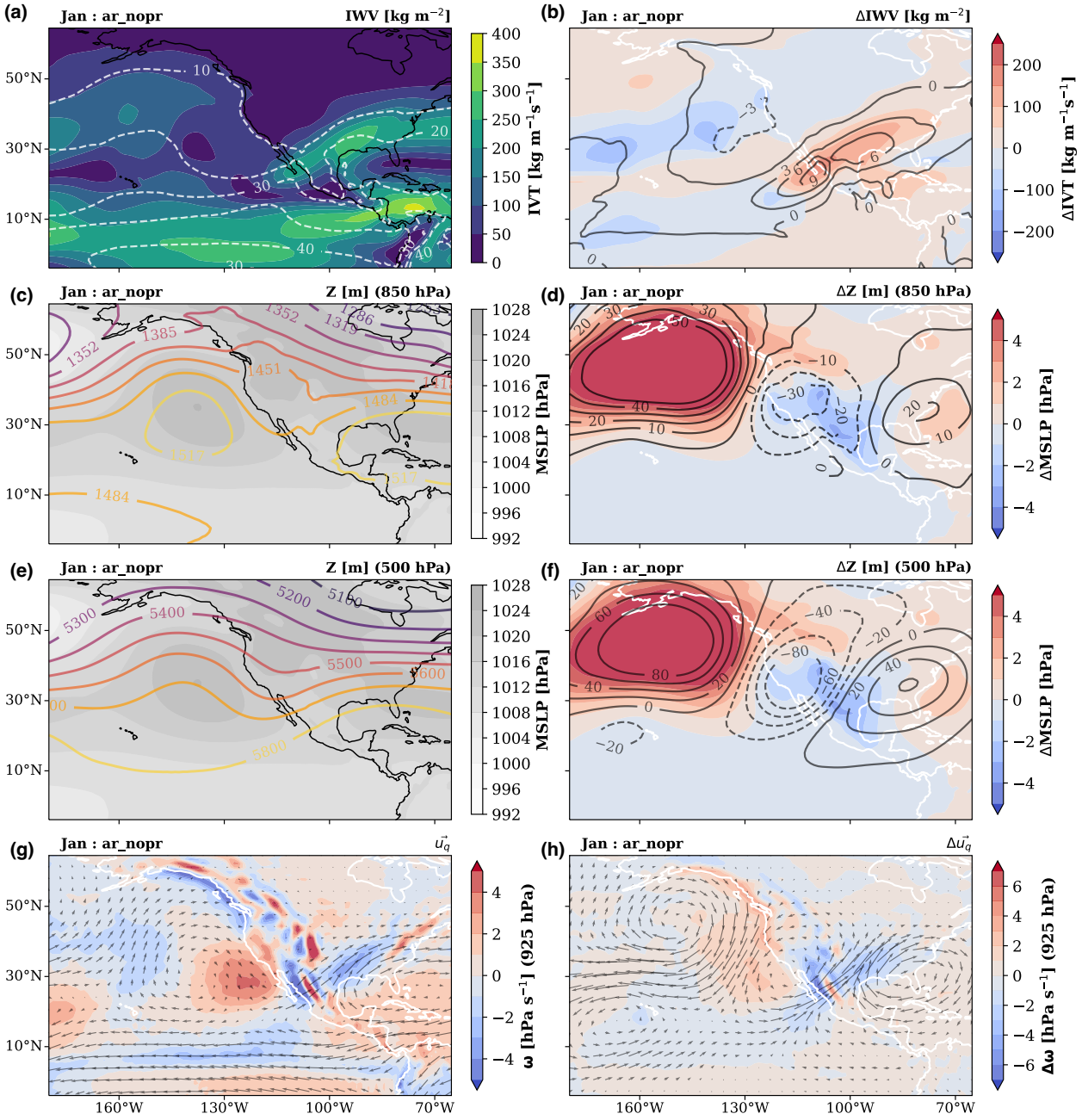

Figure C.16: State of the atmosphere during AR landfalling and without extreme precipitation at `Loc1` in January. Black contours variables are specified on the top-right of each plot. Left column: IWV, IVT, mean sea level pressure, geopotential height at 850 and 500 hPA, IVT direction (u_q), and ω at 650 hPa. Right column: anomalies with respect to the long-term mean for the same variables.

C.4 Precipitation+no AR Composite

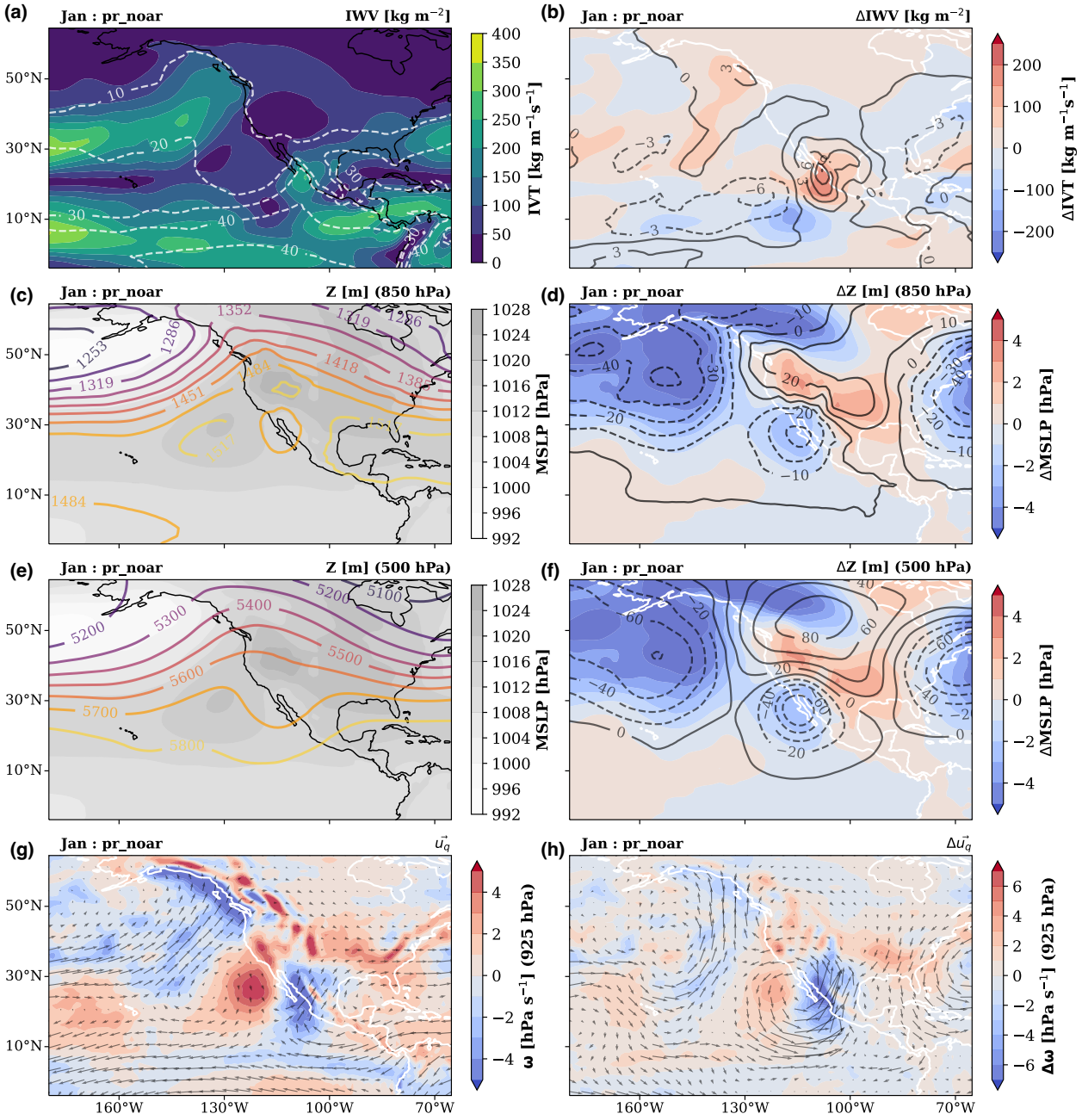

Figure C.17: State of the atmosphere during extreme precipitation without AR landfalling conditions at `Loc1` in December. Black contours variables are specified on the top-right of each plot. Left column: IWV, IVT, mean sea level pressure, geopotential height at 850 and 500 hPA, IVT direction (u_q), and ω at 650 hPa. Right column: anomalies with respect to the long-term mean for the same variables.

C.5 Time Correlation between AR and Extreme Precipitation Events

In this section, we present the times where each of the composites is present at `Loc1` for the entire 1900-2010 period. We notice that AR detection (blue circle markers in C.18 are in general around the same dates that the extreme precipitation events (purple cross markers), in some cases before or after, but around each other. It is possible that an ARDTs tuned for tropical ARs would better detect ARs near CWM. Moreover, in future works, we could explore different reanalysis or precipitation data that, together with a tropical ARDT, could mean an even more significant correlation between extreme dry-season precipitation and ARs in CWM. The following seven pages show each composite's 1906-2010 events; we do not add a caption for simplicity.

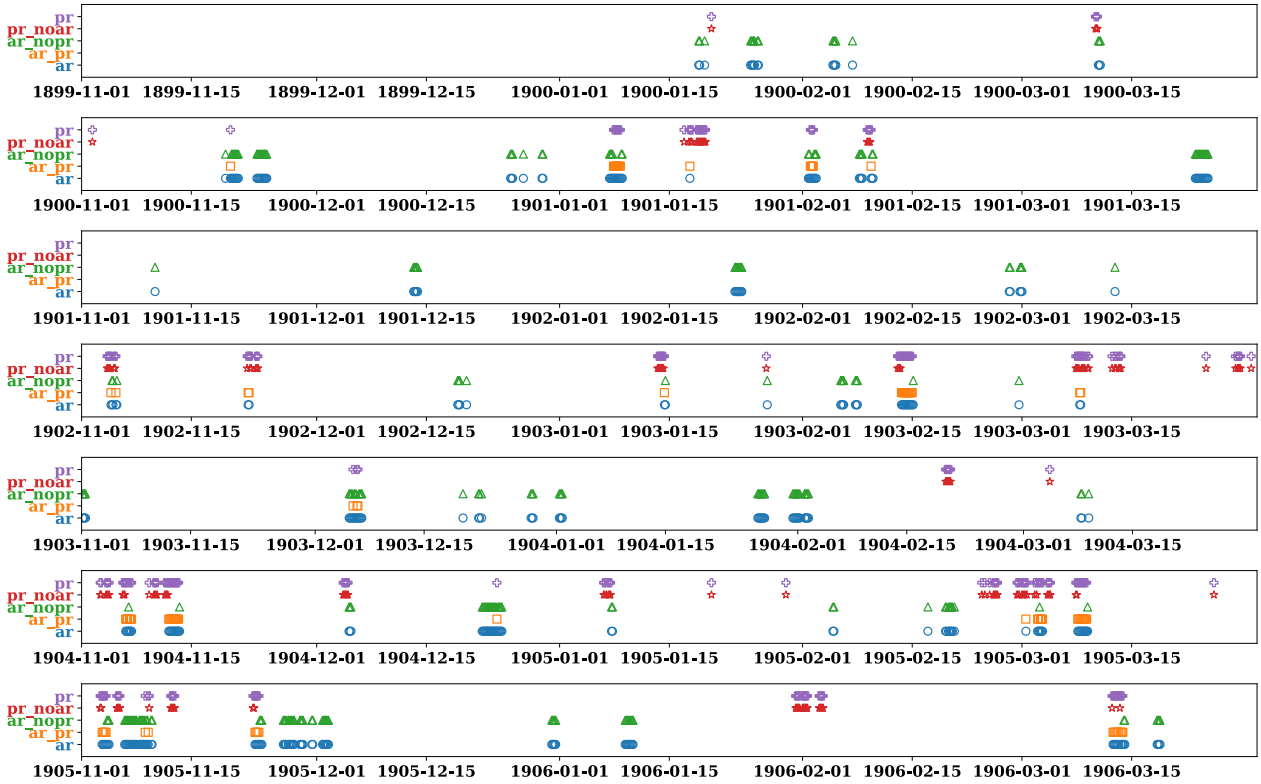

Figure C.18: Time of event for each composite (*ar*, *ar_pr*, *ar_nopr*, *pr_noar*, and *pr*). Each subfigure shows a year in the 1900-2010 period to be able to clearly look at the overlap of events across composites. Blue circle markers represent *ar*, orange squares *ar_pr*, green triangles *ar_nopr*, red stars *pr_noar*, and purple crosses *pr*.


pr
pr_noar
ar_nopr
ar_pr
ar
1906-11-01 1906-11-15 1906-12-01 1906-12-15 1907-01-01 1907-01-15 1907-02-01 1907-02-15 1907-03-01 1907-03-15
1907-11-01 1907-11-15 1907-12-01 1907-12-15 1908-01-01 1908-01-15 1908-02-01 1908-02-15 1908-03-01 1908-03-15
1908-11-01 1908-11-15 1908-12-01 1908-12-15 1909-01-01 1909-01-15 1909-02-01 1909-02-15 1909-03-01 1909-03-15
1909-11-01 1909-11-15 1909-12-01 1909-12-15 1910-01-01 1910-01-15 1910-02-01 1910-02-15 1910-03-01 1910-03-15
1910-11-01 1910-11-15 1910-12-01 1910-12-15 1911-01-01 1911-01-15 1911-02-01 1911-02-15 1911-03-01 1911-03-15
1911-11-01 1911-11-15 1911-12-01 1911-12-15 1912-01-01 1912-01-15 1912-02-01 1912-02-15 1912-03-01 1912-03-15
1912-11-01 1912-11-15 1912-12-01 1912-12-15 1913-01-01 1913-01-15 1913-02-01 1913-02-15 1913-03-01 1913-03-15
1913-11-01 1913-11-15 1913-12-01 1913-12-15 1914-01-01 1914-01-15 1914-02-01 1914-02-15 1914-03-01 1914-03-15
1914-11-01 1914-11-15 1914-12-01 1914-12-15 1915-01-01 1915-01-15 1915-02-01 1915-02-15 1915-03-01 1915-03-15
1915-11-01 1915-11-15 1915-12-01 1915-12-15 1916-01-01 1916-01-15 1916-02-01 1916-02-15 1916-03-01 1916-03-15
1916-11-01 1916-11-15 1916-12-01 1916-12-15 1917-01-01 1917-01-15 1917-02-01 1917-02-15 1917-03-01 1917-03-15
1917-11-01 1917-11-15 1917-12-01 1917-12-15 1918-01-01 1918-01-15 1918-02-01 1918-02-15 1918-03-01 1918-03-15
1918-11-01 1918-11-15 1918-12-01 1918-12-15 1919-01-01 1919-01-15 1919-02-01 1919-02-15 1919-03-01 1919-03-15
1919-11-01 1919-11-15 1919-12-01 1919-12-15 1920-01-01 1920-01-15 1920-02-01 1920-02-15 1920-03-01 1920-03-15
1920-11-01 1920-11-15 1920-12-01 1920-12-15 1921-01-01 1921-01-15 1921-02-01 1921-02-15 1921-03-01 1921-03-15


pr
pr_noar
ar_nopr
ar_pr
ar
1921-11-01 1921-11-15 1921-12-01 1921-12-15 1922-01-01 1922-01-15 1922-02-01 1922-02-15 1922-03-01 1922-03-15
1922-11-01 1922-11-15 1922-12-01 1922-12-15 1923-01-01 1923-01-15 1923-02-01 1923-02-15 1923-03-01 1923-03-15
1923-11-01 1923-11-15 1923-12-01 1923-12-15 1924-01-01 1924-01-15 1924-02-01 1924-02-15 1924-03-01 1924-03-15
1924-11-01 1924-11-15 1924-12-01 1924-12-15 1925-01-01 1925-01-15 1925-02-01 1925-02-15 1925-03-01 1925-03-15
1925-11-01 1925-11-15 1925-12-01 1925-12-15 1926-01-01 1926-01-15 1926-02-01 1926-02-15 1926-03-01 1926-03-15
1926-11-01 1926-11-15 1926-12-01 1926-12-15 1927-01-01 1927-01-15 1927-02-01 1927-02-15 1927-03-01 1927-03-15
1927-11-01 1927-11-15 1927-12-01 1927-12-15 1928-01-01 1928-01-15 1928-02-01 1928-02-15 1928-03-01 1928-03-15
1928-11-01 1928-11-15 1928-12-01 1928-12-15 1929-01-01 1929-01-15 1929-02-01 1929-02-15 1929-03-01 1929-03-15
1929-11-01 1929-11-15 1929-12-01 1929-12-15 1930-01-01 1930-01-15 1930-02-01 1930-02-15 1930-03-01 1930-03-15
1930-11-01 1930-11-15 1930-12-01 1930-12-15 1931-01-01 1931-01-15 1931-02-01 1931-02-15 1931-03-01 1931-03-15
1931-11-01 1931-11-15 1931-12-01 1931-12-15 1932-01-01 1932-01-15 1932-02-01 1932-02-15 1932-03-01 1932-03-15
1932-11-01 1932-11-15 1932-12-01 1932-12-15 1933-01-01 1933-01-15 1933-02-01 1933-02-15 1933-03-01 1933-03-15
1933-11-01 1933-11-15 1933-12-01 1933-12-15 1934-01-01 1934-01-15 1934-02-01 1934-02-15 1934-03-01 1934-03-15
1934-11-01 1934-11-15 1934-12-01 1934-12-15 1935-01-01 1935-01-15 1935-02-01 1935-02-15 1935-03-01 1935-03-15
1935-11-01 1935-11-15 1935-12-01 1935-12-15 1936-01-01 1936-01-15 1936-02-01 1936-02-15 1936-03-01 1936-03-15


pr
pr_noar
ar_nopr
ar_pr
ar
1936-11-01 1936-11-15 1936-12-01 1936-12-15 1937-01-01 1937-01-15 1937-02-01 1937-02-15 1937-03-01 1937-03-15
1937-11-01 1937-11-15 1937-12-01 1937-12-15 1938-01-01 1938-01-15 1938-02-01 1938-02-15 1938-03-01 1938-03-15
1938-11-01 1938-11-15 1938-12-01 1938-12-15 1939-01-01 1939-01-15 1939-02-01 1939-02-15 1939-03-01 1939-03-15
1939-11-01 1939-11-15 1939-12-01 1939-12-15 1940-01-01 1940-01-15 1940-02-01 1940-02-15 1940-03-01 1940-03-15
1940-11-01 1940-11-15 1940-12-01 1940-12-15 1941-01-01 1941-01-15 1941-02-01 1941-02-15 1941-03-01 1941-03-15
1941-11-01 1941-11-15 1941-12-01 1941-12-15 1942-01-01 1942-01-15 1942-02-01 1942-02-15 1942-03-01 1942-03-15
1942-11-01 1942-11-15 1942-12-01 1942-12-15 1943-01-01 1943-01-15 1943-02-01 1943-02-15 1943-03-01 1943-03-15
1943-11-01 1943-11-15 1943-12-01 1943-12-15 1944-01-01 1944-01-15 1944-02-01 1944-02-15 1944-03-01 1944-03-15
1944-11-01 1944-11-15 1944-12-01 1944-12-15 1945-01-01 1945-01-15 1945-02-01 1945-02-15 1945-03-01 1945-03-15
1945-11-01 1945-11-15 1945-12-01 1945-12-15 1946-01-01 1946-01-15 1946-02-01 1946-02-15 1946-03-01 1946-03-15
1946-11-01 1946-11-15 1946-12-01 1946-12-15 1947-01-01 1947-01-15 1947-02-01 1947-02-15 1947-03-01 1947-03-15
1947-11-01 1947-11-15 1947-12-01 1947-12-15 1948-01-01 1948-01-15 1948-02-01 1948-02-15 1948-03-01 1948-03-15
1948-11-01 1948-11-15 1948-12-01 1948-12-15 1949-01-01 1949-01-15 1949-02-01 1949-02-15 1949-03-01 1949-03-15
1949-11-01 1949-11-15 1949-12-01 1949-12-15 1950-01-01 1950-01-15 1950-02-01 1950-02-15 1950-03-01 1950-03-15
1950-11-01 1950-11-15 1950-12-01 1950-12-15 1951-01-01 1951-01-15 1951-02-01 1951-02-15 1951-03-01 1951-03-15


pr
pr_noar
ar_nopr
ar_pr
ar
1951-11-01 1951-11-15 1951-12-01 1951-12-15 1952-01-01 1952-01-15 1952-02-01 1952-02-15 1952-03-01 1952-03-15
1952-11-01 1952-11-15 1952-12-01 1952-12-15 1953-01-01 1953-01-15 1953-02-01 1953-02-15 1953-03-01 1953-03-15
1953-11-01 1953-11-15 1953-12-01 1953-12-15 1954-01-01 1954-01-15 1954-02-01 1954-02-15 1954-03-01 1954-03-15
1954-11-01 1954-11-15 1954-12-01 1954-12-15 1955-01-01 1955-01-15 1955-02-01 1955-02-15 1955-03-01 1955-03-15
1955-11-01 1955-11-15 1955-12-01 1955-12-15 1956-01-01 1956-01-15 1956-02-01 1956-02-15 1956-03-01 1956-03-15
1956-11-01 1956-11-15 1956-12-01 1956-12-15 1957-01-01 1957-01-15 1957-02-01 1957-02-15 1957-03-01 1957-03-15
1957-11-01 1957-11-15 1957-12-01 1957-12-15 1958-01-01 1958-01-15 1958-02-01 1958-02-15 1958-03-01 1958-03-15
1958-11-01 1958-11-15 1958-12-01 1958-12-15 1959-01-01 1959-01-15 1959-02-01 1959-02-15 1959-03-01 1959-03-15
1959-11-01 1959-11-15 1959-12-01 1959-12-15 1960-01-01 1960-01-15 1960-02-01 1960-02-15 1960-03-01 1960-03-15
1960-11-01 1960-11-15 1960-12-01 1960-12-15 1961-01-01 1961-01-15 1961-02-01 1961-02-15 1961-03-01 1961-03-15
1961-11-01 1961-11-15 1961-12-01 1961-12-15 1962-01-01 1962-01-15 1962-02-01 1962-02-15 1962-03-01 1962-03-15
1962-11-01 1962-11-15 1962-12-01 1962-12-15 1963-01-01 1963-01-15 1963-02-01 1963-02-15 1963-03-01 1963-03-15
1963-11-01 1963-11-15 1963-12-01 1963-12-15 1964-01-01 1964-01-15 1964-02-01 1964-02-15 1964-03-01 1964-03-15
1964-11-01 1964-11-15 1964-12-01 1964-12-15 1965-01-01 1965-01-15 1965-02-01 1965-02-15 1965-03-01 1965-03-15
1965-11-01 1965-11-15 1965-12-01 1965-12-15 1966-01-01 1966-01-15 1966-02-01 1966-02-15 1966-03-01 1966-03-15


pr
pr_noar
ar_nopr
ar_pr
ar
1966-11-01 1966-11-15 1966-12-01 1966-12-15 1967-01-01 1967-01-15 1967-02-01 1967-02-15 1967-03-01 1967-03-15
1967-11-01 1967-11-15 1967-12-01 1967-12-15 1968-01-01 1968-01-15 1968-02-01 1968-02-15 1968-03-01 1968-03-15
1968-11-01 1968-11-15 1968-12-01 1968-12-15 1969-01-01 1969-01-15 1969-02-01 1969-02-15 1969-03-01 1969-03-15
1969-11-01 1969-11-15 1969-12-01 1969-12-15 1970-01-01 1970-01-15 1970-02-01 1970-02-15 1970-03-01 1970-03-15
1970-11-01 1970-11-15 1970-12-01 1970-12-15 1971-01-01 1971-01-15 1971-02-01 1971-02-15 1971-03-01 1971-03-15
1971-11-01 1971-11-15 1971-12-01 1971-12-15 1972-01-01 1972-01-15 1972-02-01 1972-02-15 1972-03-01 1972-03-15
1972-11-01 1972-11-15 1972-12-01 1972-12-15 1973-01-01 1973-01-15 1973-02-01 1973-02-15 1973-03-01 1973-03-15
1973-11-01 1973-11-15 1973-12-01 1973-12-15 1974-01-01 1974-01-15 1974-02-01 1974-02-15 1974-03-01 1974-03-15
1974-11-01 1974-11-15 1974-12-01 1974-12-15 1975-01-01 1975-01-15 1975-02-01 1975-02-15 1975-03-01 1975-03-15
1975-11-01 1975-11-15 1975-12-01 1975-12-15 1976-01-01 1976-01-15 1976-02-01 1976-02-15 1976-03-01 1976-03-15
1976-11-01 1976-11-15 1976-12-01 1976-12-15 1977-01-01 1977-01-15 1977-02-01 1977-02-15 1977-03-01 1977-03-15
1977-11-01 1977-11-15 1977-12-01 1977-12-15 1978-01-01 1978-01-15 1978-02-01 1978-02-15 1978-03-01 1978-03-15
1978-11-01 1978-11-15 1978-12-01 1978-12-15 1979-01-01 1979-01-15 1979-02-01 1979-02-15 1979-03-01 1979-03-15
1979-11-01 1979-11-15 1979-12-01 1979-12-15 1980-01-01 1980-01-15 1980-02-01 1980-02-15 1980-03-01 1980-03-15
1980-11-01 1980-11-15 1980-12-01 1980-12-15 1981-01-01 1981-01-15 1981-02-01 1981-02-15 1981-03-01 1981-03-15

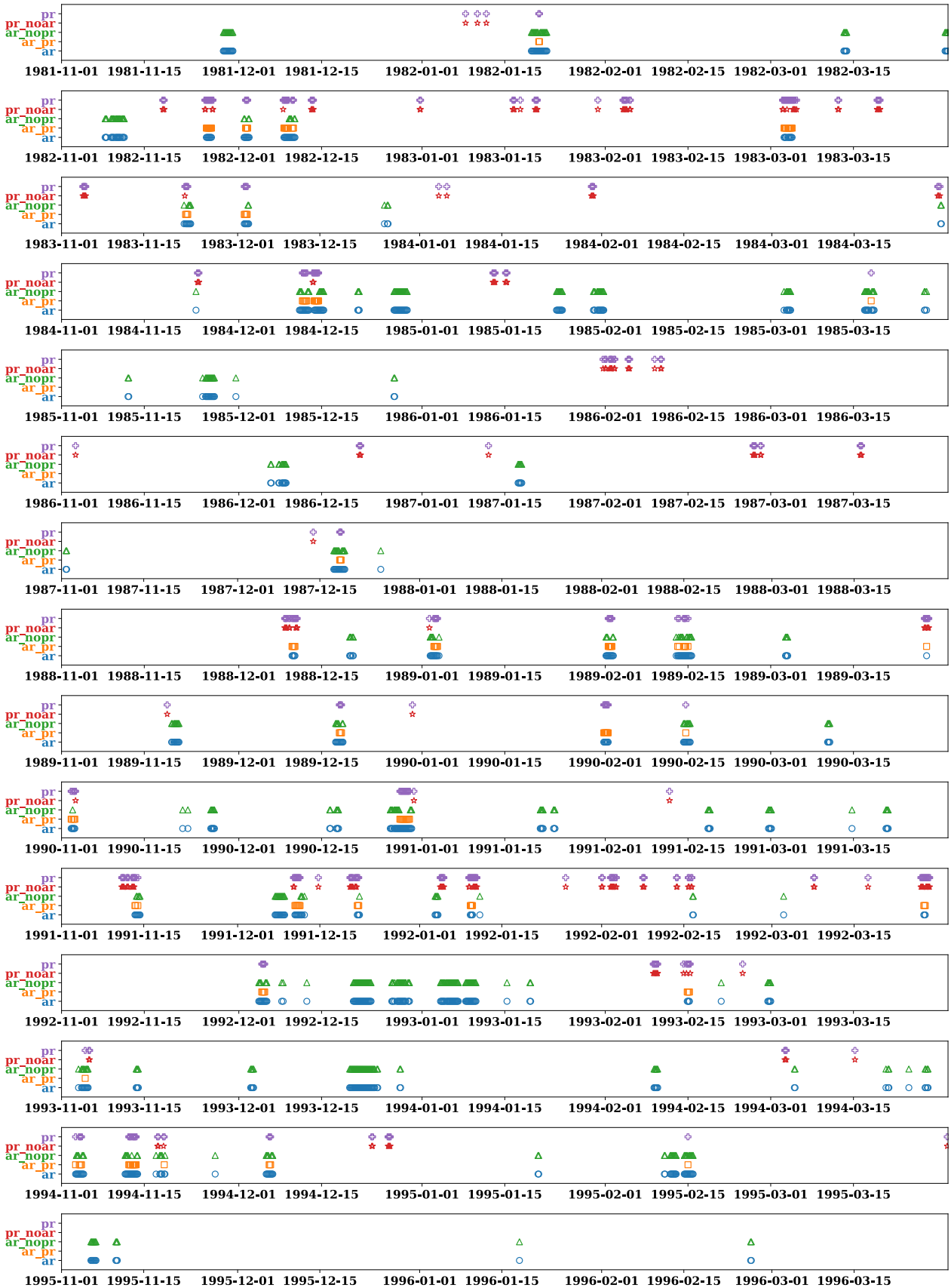
pr
pr_noar
ar_nopr
ar_pr
ar
1981-11-01 1981-11-15 1981-12-01 1981-12-15 1982-01-01 1982-01-15 1982-02-01 1982-02-15 1982-03-01 1982-03-15
1982-11-01 1982-11-15 1982-12-01 1982-12-15 1983-01-01 1983-01-15 1983-02-01 1983-02-15 1983-03-01 1983-03-15
1983-11-01 1983-11-15 1983-12-01 1983-12-15 1984-01-01 1984-01-15 1984-02-01 1984-02-15 1984-03-01 1984-03-15
1984-11-01 1984-11-15 1984-12-01 1984-12-15 1985-01-01 1985-01-15 1985-02-01 1985-02-15 1985-03-01 1985-03-15
1985-11-01 1985-11-15 1985-12-01 1985-12-15 1986-01-01 1986-01-15 1986-02-01 1986-02-15 1986-03-01 1986-03-15
1986-11-01 1986-11-15 1986-12-01 1986-12-15 1987-01-01 1987-01-15 1987-02-01 1987-02-15 1987-03-01 1987-03-15
1987-11-01 1987-11-15 1987-12-01 1987-12-15 1988-01-01 1988-01-15 1988-02-01 1988-02-15 1988-03-01 1988-03-15
1988-11-01 1988-11-15 1988-12-01 1988-12-15 1989-01-01 1989-01-15 1989-02-01 1989-02-15 1989-03-01 1989-03-15
1989-11-01 1989-11-15 1989-12-01 1989-12-15 1990-01-01 1990-01-15 1990-02-01 1990-02-15 1990-03-01 1990-03-15
1990-11-01 1990-11-15 1990-12-01 1990-12-15 1991-01-01 1991-01-15 1991-02-01 1991-02-15 1991-03-01 1991-03-15
1991-11-01 1991-11-15 1991-12-01 1991-12-15 1992-01-01 1992-01-15 1992-02-01 1992-02-15 1992-03-01 1992-03-15
1992-11-01 1992-11-15 1992-12-01 1992-12-15 1993-01-01 1993-01-15 1993-02-01 1993-02-15 1993-03-01 1993-03-15
1993-11-01 1993-11-15 1993-12-01 1993-12-15 1994-01-01 1994-01-15 1994-02-01 1994-02-15 1994-03-01 1994-03-15
1994-11-01 1994-11-15 1994-12-01 1994-12-15 1995-01-01 1995-01-15 1995-02-01 1995-02-15 1995-03-01 1995-03-15
1995-11-01 1995-11-15 1995-12-01 1995-12-15 1996-01-01 1996-01-15 1996-02-01 1996-02-15 1996-03-01 1996-03-15


pr
pr_noar
ar_nopr
ar_pr
ar
1996-11-01 1996-11-15 1996-12-01 1996-12-15 1997-01-01 1997-01-15 1997-02-01 1997-02-15 1997-03-01 1997-03-15
1997-11-01 1997-11-15 1997-12-01 1997-12-15 1998-01-01 1998-01-15 1998-02-01 1998-02-15 1998-03-01 1998-03-15
1998-11-01 1998-11-15 1998-12-01 1998-12-15 1999-01-01 1999-01-15 1999-02-01 1999-02-15 1999-03-01 1999-03-15
1999-11-01 1999-11-15 1999-12-01 1999-12-15 2000-01-01 2000-01-15 2000-02-01 2000-02-15 2000-03-01 2000-03-15
2000-11-01 2000-11-15 2000-12-01 2000-12-15 2001-01-01 2001-01-15 2001-02-01 2001-02-15 2001-03-01 2001-03-15
2001-11-01 2001-11-15 2001-12-01 2001-12-15 2002-01-01 2002-01-15 2002-02-01 2002-02-15 2002-03-01 2002-03-15
2002-11-01 2002-11-15 2002-12-01 2002-12-15 2003-01-01 2003-01-15 2003-02-01 2003-02-15 2003-03-01 2003-03-15
2003-11-01 2003-11-15 2003-12-01 2003-12-15 2004-01-01 2004-01-15 2004-02-01 2004-02-15 2004-03-01 2004-03-15
2004-11-01 2004-11-15 2004-12-01 2004-12-15 2005-01-01 2005-01-15 2005-02-01 2005-02-15 2005-03-01 2005-03-15
2005-11-01 2005-11-15 2005-12-01 2005-12-15 2006-01-01 2006-01-15 2006-02-01 2006-02-15 2006-03-01 2006-03-15
2006-11-01 2006-11-15 2006-12-01 2006-12-15 2007-01-01 2007-01-15 2007-02-01 2007-02-15 2007-03-01 2007-03-15
2007-11-01 2007-11-15 2007-12-01 2007-12-15 2008-01-01 2008-01-15 2008-02-01 2008-02-15 2008-03-01 2008-03-15
2008-11-01 2008-11-15 2008-12-01 2008-12-15 2009-01-01 2009-01-15 2009-02-01 2009-02-15 2009-03-01 2009-03-15
2009-11-01 2009-11-15 2009-12-01 2009-12-15 2010-01-01 2010-01-15 2010-02-01 2010-02-15 2010-03-01 2010-03-15
2010-11-01 2010-11-15 2010-12-01 2010-12-15 2011-01-01 2011-01-15 2011-02-01 2011-02-15 2011-03-01 2011-03-15

Acknowledgment

This study was supported by the Director, Office of Science, Office of Biological and Environmental Research of the U.S. Department of Energy Regional and Global Modeling and Analysis (RGMA) and used resources of the National Energy Research Scientific Computing Center (NERSC), also supported by the Office of Science of the U.S. Department of Energy under Contract no. DE-AC02-05CH11231.

We would like to thank the National Council of Science and Technology of Mexico (CONACYT) and UC Mexus for the doctoral fellowship #409048 that partially supported this work.

This project was supported by the Environmental Resilience Institute, funded by Indiana University's Prepared for Environmental Change Grand Challenge initiative.

We would like to acknowledge the Research Data Archive (RDA), managed by the Data Engineering and Curation Section (DECS) of the Computational and Information Systems Laboratory (CISL) at the National Center for Atmospheric Research for providing the ERA5 dataset at `https://rda.ucar.edu/datasets/ds633.0/`.

We would like to acknowledge the European Centre for Medium-Range Weather Forecasts and ERA-20C Project (`https://www.ecmwf.int/en/forecasts/datasets/reanalysis-datasets/era-20c`). ERA-20C was accessed through the Copernicus Climate Change Service (C3S) Climate Data Store (CDS) - `https://apps.ecmwf.int/datasets/data/era20c-ofa/`.

CPC Global Unified Precipitation data provided by the NOAA/OAR/ESRL PSL, Boulder, Colorado, USA, from their Web site at `https://psl.noaa.gov/data/gridded/data.cpc.globalprecip.html`.

We acknowledge the World Climate Research Programme's Working Group on Coupled Modelling, which is responsible for CMIP, and we thank the climate modeling groups (listed in Table 3.1 of this paper) for producing and making available their model output. For CMIP the U.S. Department of Energy's Program for Climate Model Diagnosis and Intercomparison provides coordinating support and led development of software infrastructure in partnership

with the Global Organization for Earth System Science Portals.

We acknowledge Livneh, Ben & National Center for Atmospheric Research Staff (Eds). Last modified 12 Dec 2019. "The Climate Data Guide: Livneh gridded precipitation and other meteorological variables for continental US, Mexico and southern Canada." Retrieved from `https://climatedataguide.ucar.edu/climate-data/livneh-gridded-precipitation-and-other-meteorological-variables-continental-us-mexico`.

We would like to acknowledge the ClimateNet team who facilitated the labeling tool and data for the ARTMIP workshop AR labeling campaign, in alphabetical order: Karthik Kashinath, Sol Kim, Jiayi Chen, and Kevin Yang.

We would like to acknowledge participants in the ARTMIP workshop ClimateNet AR labeling campaign, in alphabetical order: Alan Rhoades, Allison Michaelis, Ashley Payne, Brian Kawzenuk, Eric Shearer, Huanping Huang, Jonathan Rutz, Paul Ullrich, Sol Kim, Swen Brands, Yang Zhou, and Zhenhai Zhang.

We would like to thank the three anonymous reviewers for Chapter's 2 published article "Constraining and Characterizing the Size of Atmospheric Rivers: A Perspective Independent From the Detection Algorithm", whose input greatly improved the presentation and quality of this article.

We would like to acknowledge Dr. William Collins, Dr. Paul Ullrich, Dr. Shu-Hua Chen, and Dr. Travis O'Brien, the committee members for this thesis dissertation. We thank you for your time and effort. Your input and suggestionsz have helped this work to develop into what it is today.

Bibliography

Magaña, Víctor and Pérez, Joel and Vázquez, Jorge and Pérez, José (2003). Impact of el niño on precipitation in mexico. *Geofísica Internacional*.

Adams, D. K. and Comrie, A. C. (1997). The north american monsoon. *Bulletin of the American Meteorological Society*, 78(10):2197 – 2214.

Agustín Breña-Naranjo, J., Pedrozo-Acuña, A., Pozos-Estrada, O., Jiménez-López, S. A., and López-López, M. R. (2015). The contribution of tropical cyclones to rainfall in mexico. *Physics and Chemistry of the Earth, Parts A/B/C*, 83-84:111–122. Emerging science and applications with microwave remote sensing data.

Arriaga-Ramírez, Sarahí and Cavazos, Tereza (2010). Regional trends of daily precipitation indices in northwest mexico and southwest united states. *Journal of Geophysical Research: Atmospheres*, 115(D14).

Blamey, R. C., Ramos, A. M., Trigo, R. M., Tomé, R., and Reason, C. J. (2018). The influence of atmospheric rivers over the South Atlantic on winter rainfall in South Africa. *Journal of Hydrometeorology*, 19(1):127–142.

Breitburg, Denise; Grégoire, Marilaure and Isensee, Kirsten (2018). The ocean is losing its breath: declining oxygen in the world's ocean and coastal waters; summary for policy makers.

Cavazos, Tereza and Arriaga-Ramírez, Sarahí (2012). Downscaled climate change scenarios for baja california and the north american monsoon during the twenty-first century. *Journal of Climate*, 25(17):5904 – 5915.

Chen, M., Shi, W., Xie, P., Silva, V. B. S., Kousky, V. E., Wayne Higgins, R., and Janowiak, J. E. (2008). Assessing objective techniques for gauge-based analyses of global daily precipitation. *Journal of Geophysical Research: Atmospheres*, 113(D4).

Choi, K.-Y., Vecchi, G. A., and Wittenberg, A. T. (2015). Nonlinear zonal wind response to enso in the cmip5 models: Roles of the zonal and meridional shift of the itcz/spcz and the simulated climatological precipitation. *Journal of Climate*, 28(21):8556 – 8573.

Copernicus Climate Change Service (2017). ERA5: Fifth generation of ECMWF atmospheric reanalyses of the global climate.

Cordeira, J. M., Martin Ralph, F., and Moore, B. J. (2013). The development and evolution of two atmospheric rivers in proximity to western north pacific tropical cyclones in october 2010. *Monthly Weather Review*, 141(12):4234–4255.

Cruz López, M. (2011). Comparación del ciclo agrícola actual con el de hace unos diez anos en San Juan Jalpa municipio San Felipe Del Progreso Estado de México: Evidencia de adapatación al cambio climático. *Ra Ximhai. Revista de Sociedad, Cultura y Desarrollo Sustentable*, 7(1):95–106.

Curtis, S. (2007). The atlantic multidecadal oscillation and extreme daily precipitation over the US and mexico during the hurricane season. *Climate Dynamics*, 30(4):343–351.

De Luna, M., Waliser, D., Guan, B., Sengupta, A., Raymond, C., and Ye1, H. (2020). Tropical atmospheric rivers. Paper presented at the Virtual Symposium by the International Atmospheric Rivers Conference (IARC) Community, 5-9 October, 2020.

De Luna, M. I. (2021). Tropical atmospheric rivers. *Ph.D. dissertation, California State University, Los Angeles*, ProQuest Dissertations Publishing.

Dettinger, M. (2011). Climate change, atmospheric rivers, and floods in California - a multimodel analysis of storm frequency and magnitude changes. *Journal of the American Water Resources Association*, 47(3):514–523.

Dettinger, M., Ralph, F., and Lavers, D. (2015). Setting the stage for a global science of atmospheric rivers. *Eos*, 96.

Dettinger, M. D. (2013). Atmospheric Rivers as Drought Busters on the U.S. West Coast. *Journal of Hydrometeorology*, 14(6):1721–1732.

Dettinger, M. D., Ralph, F. M., Das, T., Neiman, P. J., and Cayan, D. R. (2011). Atmospheric Rivers, Floods and the Water Resources of California. *Water*, 3(2):445–478.

Dirmeyer, P. A. and Brubaker, K. L. (2007). Characterization of the Global Hydrologic Cycle from a Back-Trajectory Analysis of Atmospheric Water Vapor. *Journal of Hydrometeorology*, 8(1):20–37.

Dominguez, C., Done, J. M., and Bruyère, C. L. (2020). Easterly wave contributions to seasonal rainfall over the tropical americas in observations and a regional climate model. *Climate Dynamics*, 54(1):191–209.

Dominguez, Christian and Magaña, Victor (2018). The role of tropical cyclones in precipitation over the tropical and subtropical north america. *Frontiers in Earth Science*, 6.

Domínguez-Hernández, G., Cepeda-Morales, J., Soto-Mardones, L., Rivera-Caicedo, J. P., Romero-Rodríguez, D. A., Inda-Díaz, E. A., Hernández-Almeida, O. U., and Romero-Bañuelos, C. (2020). Semi-annual variations of chlorophyll concentration on the Eastern Tropical Pacific coast of Mexico. *Advances in Space Research*, 65(11):2595–2607.

Dong, L., Leung, L. R., Lu, J., and Gao, Y. (2019). Contributions of extreme and non-extreme precipitation to california precipitation seasonality changes under warming. *Geophysical Research Letters*, 46(22):13470–13478.

Douglas, A. V. and Englehart, P. J. (2007). A climatological perspective of transient synoptic features during name 2004. *Journal of Climate*, 20(9):1947 – 1954.

Díaz, S., Salinas-Zavala, C., and Hernández-Vázquez, S. (2008). Variability of rainfall from tropical cyclones in northwestern México and its relation to SOI and PDO. *Atmósfera*, 21:213 – 223.

Eldardiry, H., Mahmood, A., Chen, X., Hossain, F., Nijssen, B., and Lettenmaier, D. P. (2019). Atmospheric River–Induced Precipitation and Snowpack during the Western United States Cold Season. *Journal of Hydrometeorology*, 20(4):613–630.

Espinoza, V., Waliser, D. E., Guan, B., Lavers, D. A., and Ralph, F. M. (2018). Global Analysis of Climate Change Projection Effects on Atmospheric Rivers. *Geophysical Research Letters*, 45(9):4299–4308.

European Centre for Medium-Range Weather Forecasts (2014). Era-20c project (ecmwf atmospheric reanalysis of the 20th century). https://doi.org/10.5065/D6VQ30QG. (Updated daily.) Accessed January 2022.

Eyring, V., Bony, S., Meehl, G. A., Senior, C. A., Stevens, B., Stouffer, R. J., and Taylor, K. E. (2016). Overview of the Coupled Model Intercomparison Project Phase 6 (CMIP6) experimental design and organization. *Geoscientific Model Development*, 9(5):1937–1958.

Farfán, L. M. and Fogel, I. (2007). Influence of tropical cyclones on humidity patterns over southern baja california, mexico. *Monthly Weather Review*, 135(4):1208–1224.

Gao, Y., Lu, J., and Leung, L. R. (2016). Uncertainties in Projecting Future Changes in Atmospheric Rivers and Their Impacts on Heavy Precipitation over Europe. *Journal of Climate*, 29(18):6711–6726.

Gao, Y., Lu, J., Leung, L. R., Yang, Q., Hagos, S., and Qian, Y. (2015). Dynamical and thermodynamical modulations on future changes of landfalling atmospheric rivers over western North America. *Geophysical Research Letters*, 42(17):7179–7186.

Garaboa-Paz, D., Eiras-Barca, J., Huhn, F., and Pérez-Muñuzuri, V. (2015). Lagrangian coherent structures along atmospheric rivers. *Chaos: An Interdisciplinary Journal of Nonlinear Science*, 25(6):063105.

García Amaro de Miranda, E. (2003). Distribución de la precipitación en la República Mexicana. *Investigaciones geográficas*, pages 67 – 76.

Gelaro, R., McCarty, W., Suárez, M. J., Todling, R., Molod, A., Takacs, L., Randles, C. A., Darmenov, A., Bosilovich, M. G., Reichle, R., Wargan, K., Coy, L., Cullather, R., Draper, C., Akella, S., Buchard, V., Conaty, A., da Silva, A. M., Gu, W., Kim, G.-K., Koster, R., Lucchesi, R., Merkova, D., Nielsen, J. E., Partyka, G., Pawson, S., Putman, W., Rienecker, M., Schubert, S. D., Sienkiewicz, M., and Zhao, B. (2017). The Modern-Era Retrospective Analysis for Research and Applications, Version 2 (MERRA-2). *Journal of Climate*, 30(14):5419–5454.

Gershunov, A., Shulgina, T., Clemesha, R. E. S., Guirguis, K., Pierce, D. W., Dettinger, M. D., Lavers, D. A., Cayan, D. R., Polade, S. D., Kalansky, J., and Ralph, F. M. (2019). Precipitation regime change in Western North America: The role of Atmospheric Rivers. *Scientific Reports*, 9(1):9944.

Gershunov, A., Shulgina, T., Ralph, F. M., Lavers, D. A., and Rutz, J. J. (2017). Assessing the climate-scale variability of atmospheric rivers affecting western North America. *Geophysical Research Letters*, 44(15):7900–7908.

Gimeno, L., Dominguez, F., Nieto, R., Trigo, R., Drumond, A., Reason, C. J., Taschetto, A. S., Ramos, A. M., Kumar, R., and Marengo, J. (2016). Major Mechanisms of Atmospheric Moisture Transport and Their Role in Extreme Precipitation Events. *Annual Review of Environment and Resources*, 41(1):117–141.

Gimeno, L., Nieto, R., Vázquez, M., and Lavers, D. A. (2014). Atmospheric rivers: a mini-review. *Frontiers in Earth Science*, 2(March):1–6.

Goldenson, N., Leung, L. R., Bitz, C. M., and Blanchard-Wrigglesworth, E. (2018). Influence of atmospheric rivers on mountain snowpack in the western United States. *Journal of Climate*, 31(24):9921–9940.

Griffa, A., Owens, K., Piterbarg, L., and Rozovskii, B. (1995). Estimates of turbulence parameters from lagrangian data using a stochastic particle model. *Journal of Marine Research*, 53(3):371–401.

Guan, B., Molotch, N. P., Waliser, D. E., Fetzer, E. J., and Neiman, P. J. (2010). Extreme snowfall events linked to atmospheric rivers and surface air temperature via satellite measurements. *Geophysical Research Letters*, 37(20):2–7.

Guan, B. and Waliser, D. E. (2015). Detection of atmospheric rivers: Evaluation and application of an algorithm for global studies. *Journal of Geophysical Research: Atmospheres*, 120(24):12514–12535.

Guan, B., Waliser, D. E., and Ralph, F. M. (2018). An Intercomparison between Reanalysis and Dropsonde Observations of the Total Water Vapor Transport in Individual Atmospheric Rivers. *Journal of Hydrometeorology*, 19(2):321–337.

Haffke, C. and Magnusdottir, G. (2013). The south pacific convergence zone in three decades of satellite images. *Journal of Geophysical Research: Atmospheres*, 118(19):10,839–10,849.

Hu, H., Dominguez, F., Wang, Z., Lavers, D. A., Zhang, G., and Ralph, F. M. (2017). Linking Atmospheric River Hydrological Impacts on the U.S. West Coast to Rossby Wave Breaking. *Journal of Climate*, 30(9):3381–3399.

Huang, H., Patricola, C. M., Bercos-Hickey, E., Zhou, Y., Rhoades, A., Risser, M. D., and Collins, W. D. (2021). Sources of subseasonal-to-seasonal predictability of atmospheric rivers and precipitation in the western United States. *Journal of Geophysical Research: Atmospheres*, 126:e2020JD034053.

Inda-Díaz, H. A., O'Brien, T. A., Zhou, Y., and Collins, W. D. (2021). Constraining and characterizing the size of atmospheric rivers: A perspective independent from the detection algorithm. *Journal of Geophysical Research: Atmospheres*, 126(16):e2020JD033746. e2020JD033746 2020JD033746.

Kim, J., Waliser, D. E., Neiman, P. J., Guan, B., Ryoo, J. M., and Wick, G. A. (2013). Effects of atmospheric river landfalls on the cold season precipitation in California. *Climate Dynamics*, 40(1-2):465–474.

LaCasce, J. (2008). Statistics from lagrangian observations. *Progress in Oceanography*, 77(1):1 – 29.

Lavers, D. A., Pappenberger, F., Richardson, D. S., and Zsoter, E. (2016a). ECMWF Extreme Forecast Index for water vapor transport: A forecast tool for atmospheric rivers and extreme precipitation. *Geophysical Research Letters*, 43(22):11,852–11,858.

Lavers, D. A., Ralph, F. M., Waliser, D. E., Gershunov, A., and Dettinger, M. D. (2015). Climate change intensification of horizontal water vapor transport in CMIP5. *Geophysical Research Letters*, 42(13):5617–5625.

Lavers, D. A. and Villarini, G. (2013a). Atmospheric rivers and flooding over the central United States. *Journal of Climate*, 26(20):7829–7836.

Lavers, D. A. and Villarini, G. (2013b). The nexus between atmospheric rivers and extreme precipitation across Europe. *Geophysical Research Letters*, 40(12):3259–3264.

Lavers, D. A., Waliser, D. E., Ralph, F. M., and Dettinger, M. D. (2016b). Predictability of horizontal water vapor transport relative to precipitation: Enhancing situational awareness for forecasting western U.S. extreme precipitation and flooding. *Geophysical Research Letters*, 43(5):2275–2282.

Leung, L.-R. and Qian, Y. (2009). Atmospheric rivers induced heavy precipitation and flooding in the western U.S. simulated by the WRF regional climate model. *Geophysical Research Letters*, 36(3):1–6.

Li, C. and Wettstein, J. J. (2012). Thermally driven and eddy-driven jet variability in reanalysis. *Journal of Climate*, 25(5):1587–1596.

Lintner, B. R. and Boos, W. R. (2019). Using atmospheric energy transport to quantitatively constrain south pacific convergence zone shifts during enso. *Journal of Climate*, 32(6):1839 – 1855.

Livneh, B., Bohn, T. J., Pierce, D. W., Munoz-Arriola, F., Nijssen, B., Vose, R., Cayan, D. R., and Brekke, L. (2015). A spatially comprehensive, hydrometeorological data set for mexico, the u.s., and southern canada 1950–2013. *Scientific Data*, 2(1).

Livneh, Ben & National Center for Atmospheric Research Staff (Eds) (Last modified 12 Dec 2019). ERA5: Fifth generation of ECMWF atmospheric reanalyses of the global climate. https://climatedataguide.ucar.edu/climate-data/livneh-gridded-precipitation-and-other-meteorological-variables-continental-us-mexico.

Lora, J. M., Mitchell, J. L., Risi, C., and Tripati, A. E. (2017). North Pacific atmospheric rivers and their influence on western North America at the Last Glacial Maximum. *Geophysical Research Letters*, 44(2):1051–1059.

Lora, J. M., Shields, C. A., and Rutz, J. J. (2020). Consensus and Disagreement in Atmospheric River Detection: ARTMIP Global Catalogues. *Geophysical Research Letters*, 47(20):1–10.

Massoud, E., Espinoza, V., Guan, B., and Waliser, D. (2019). Global climate model ensemble approaches for future projections of atmospheric rivers. *Earth's Future*, 7(10):1136–1151.

Matías Méndez and Víctor Magaña (2010). Regional aspects of prolonged meteorological droughts over mexico and central america. *Journal of Climate*, 23(5):1175 – 1188.

McClenny, E. (2020). Using simpler models to understand atmospheric river responses to sea-surface temperature increases. *Available from Dissertations & Theses @ University of California; ProQuest Dissertations & Theses A&I. (2568603716)*, pages Retrieved from `https://www.proquest.com/dissertations--theses/using--simpler--models--understand--atmospheric--river/docview/2568603716/se--2?accountid=14505`.

McClenny, E. E., Ullrich, P. A., and Grotjahn, R. (2020). Sensitivity of Atmospheric River Vapor Transport and Precipitation to Uniform Sea Surface Temperature Increases. *Journal of Geophysical Research: Atmospheres*, 125(21):1–20.

Mundhenk, B. D., Barnes, E. A., and Maloney, E. D. (2016). All-season climatology and variability of atmospheric river frequencies over the North Pacific. *Journal of Climate*, 29(13):4885–4903.

Neiman, P. J., Ralph, F. M., White, A. B., Kingsmill, D. E., and Persson, P. O. (2002). The statistical relationship between upslope flow and rainfall in California's coastal mountains: Observations during CALJET. *Monthly Weather Review*, 130(6):1468–1492.

Neiman, P. J., Ralph, F. M., Wick, G. A., Lundquist, J. D., and Dettinger, M. D. (2008). Meteorological Characteristics and Overland Precipitation Impacts of Atmospheric Rivers Affecting the West Coast of North America Based on Eight Years of SSM/I Satellite Observations. *Journal of Hydrometeorology*, 9(1):22–47.

Neiman, P. J., Ralph, M. F., Moore, B. J., Hughes, M., Mahoney, K. M., Cordeira, J. M., and Dettinger, M. D. (2013). The landfall and inland penetration of a flood-producing atmospheric river in Arizona. Part I: Observed synoptic-scale, orographic, and hydrometeorological characteristics. *Journal of Hydrometeorology*, 14(2):460–484.

Newell, R. E., Newell, N. E., Zhu, Y., and Scott, C. (1992). Tropospheric rivers? – a pilot study. *Geophysical Research Letters*, 19(24):2401–2404.

Newell, R. E. and Zhu, Y. (1994). Tropospheric rivers: A one-year record and a possible application to ice core data. *Geophysical Research Letters*, 21(2):113–116.

NOAA Physical Science Laboratory (2008). CPC global unified gauge-based analysis of daily precipitation.

O'Brien, T. A., Collins, W. D., Rauscher, S. A., and Ringler, T. D. (2014). Reducing the computational cost of the ECF using a nuFFT: A fast and objective probability density estimation method. *Computational Statistics and Data Analysis*, 79:222–234.

O'Brien, T. A., Kashinath, K., Cavanaugh, N. R., Collins, W. D., and O'Brien, J. P. (2016). A fast and objective multidimensional kernel density estimation method: FastKDE. *Computational Statistics and Data Analysis*, 101:148–160.

O'Brien, T. A., Risser, M. D., Loring, B., Elbashandy, A. A., Krishnan, H., Johnson, J., Patricola, C. M., O'Brien, J. P., Mahesh, A., Arriaga Ramirez, S., Rhoades, A. M., Charn, A., Inda Díaz, H., and Collins, W. D. (2020a). Detection of atmospheric rivers with inline uncertainty quantification: TECA-BARD v1.0.1. *Geoscientific Model Development*, 13(12):6131–6148.

O'Brien, T. A., Risser, M. D., Loring, B., Elbashandy, A. A., Krishnan, H., Johnson, J., Patricola, C. M., O'Brien, J. P., Mahesh, A., Arriaga Ramirez, S., Rhoades, A. M., Charn, A., Inda Díaz, H., and Collins, W. D. (2020b). Detection of atmospheric rivers with inline uncertainty quantification: TECA-BARD v1.0.1. *Geoscientific Model Development*, 13(12):6131–6148.

O'Brien, T. A., Wehner, M. F., Payne, A. E., Shields, C. A., Rutz, J. J., Leung, L. R., Ralph, F. M., Collow, A., Gorodetskaya, I., Guan, B., Lora, J. M., McClenny, E., Nardi, K. M., Ramos, A. M., Tomé, R., Sarangi, C., Shearer, E. J., Ullrich, P. A., Zarzycki, C., Loring, B., Huang, H., Inda-Díaz, H. A., Rhoades, A. M., and Zhou, Y. (2021). Increases in future ar count and size: Overview of the artmip tier 2 cmip5/6 experiment. *Journal of Geophysical Research: Atmospheres*, page e2021JD036013.

O'Neill, B. C., Tebaldi, C., Van Vuuren, D. P., Eyring, V., Friedlingstein, P., Hurtt, G., Knutti, R., Kriegler, E., Lamarque, J. F., Lowe, J., Meehl, G. A., Moss, R., Riahi, K., and Sanderson, B. M. (2016). The Scenario Model Intercomparison Project (ScenarioMIP) for CMIP6. *Geoscientific Model Development*, 9(9):3461–3482.

Paltan, H., Waliser, D., Lim, W. H., Guan, B., Yamazaki, D., Pant, R., and Dadson, S. (2017). Global Floods and Water Availability Driven by Atmospheric Rivers. *Geophysical Research Letters*, 44(20):10,387–10,395.

Payne, A. E., Demory, M.-E., Leung, L. R., Ramos, A. M., Shields, C. A., Rutz, J. J., Siler, N., Villarini, G., Hall, A., and Ralph, F. M. (2020). Responses and impacts of atmospheric rivers to climate change. *Nature Reviews Earth & Environment*, 1(3):143–157.

Payne, A. E. and Magnusdottir, G. (2015). An evaluation of atmospheric rivers over the North Pacific in CMIP5 and their response to warming under RCP 8.5. *Journal of Geophysical Research: Atmospheres*, 120(21):11,173–11,190.

Payne, A. E. and Magnusdottir, G. (2016). Persistent landfalling atmospheric rivers over the west coast of North America. *Journal of Geophysical Research*, 121(22):13,287–13,300.

Polade, S. D., Gershunov, A., Cayan, D. R., Dettinger, M. D., and Pierce, D. W. (2017). Precipitation in a warming world: Assessing projected hydro-climate changes in California and other Mediterranean climate regions. *Scientific Reports*, 7(1):10783.

Poli, P., Hersbach, H., Dee, D. P., Berrisford, P., Simmons, A. J., Vitart, F., Laloyaux, P., Tan, D. G. H., Peubey, C., Thépaut, J.-N., Trémolet, Y., Hólm, E. V., Bonavita, M., Isaksen, L., and Fisher, M. (2016). Era-20c: An atmospheric reanalysis of the twentieth century. *Journal of Climate*, 29(11):4083 – 4097.

Porter, J. R. and Semenov, M. A. (2005). Crop responses to climatic variation. *Philosophical Transactions of the Royal Society B: Biological Sciences*, 360(1463):2021–2035.

Prabhat, Kashinath, K., Mudigonda, M., Kim, S., Kapp-Schwoerer, L., Graubner, A., Karaismailoglu, E., von Kleist, L., Kurth, T., Greiner, A., Mahesh, A., Yang, K., Lewis, C., Chen, J., Lou, A., Chandran, S., Toms, B., Chapman, W., Dagon, K., Shields, C. A., O'Brien, T., Wehner, M., and Collins, W. (2021). Climatenet: an expert-labeled open dataset and deep learning architecture for enabling high-precision analyses of extreme weather. *Geoscientific Model Development*, 14(1):107–124.

Price, G. R. (1972). Extension of covariance selection mathematics. *Annals of Human Genetics*, 35(4):485–490.

Ralph, F., Rutz, J. J., Cordeira, J. M., Dettinger, M., Anderson, M., Reynolds, D., Schick, L. J., and Smallcomb, C. (2019a). A scale to characterize the strength and impacts of atmospheric rivers. *Bulletin of the American Meteorological Society*, 100(2):269–289.

Ralph, F. M., Coleman, T., Neiman, P. J., Zamora, R. J., and Dettinger, M. D. (2013). Observed Impacts of Duration and Seasonality of Atmospheric-River Landfalls on Soil Moisture and Runoff in Coastal Northern California. *Journal of Hydrometeorology*, 14(2):443–459.

Ralph, F. M., Dettinger, M., Lavers, D., Gorodetskaya, I. V., Martin, A., Viale, M., White, A. B., Oakley, N., Rutz, J., Spackman, J. R., Wernli, H., and Cordeira, J. (2017a). Atmospheric rivers emerge as a global science and applications focus. *Bulletin of the American Meteorological Society*, 98(9):1969–1973.

Ralph, F. M., Dettinger, M., Lavers, D., Gorodetskaya, I. V., Martin, A., Viale, M., White, A. B., Oakley, N., Rutz, J., Spackman, J. R., Wernli, H., and Cordeira, J. (2017b). Atmospheric rivers emerge as a global science and applications focus. *Bulletin of the American Meteorological Society*, 98(9):1969 – 1973.

Ralph, F. M. and Dettinger, M. D. (2011). Storms, floods, and the science of atmospheric rivers. *Eos, Transactions American Geophysical Union*, 92(32):265–266.

Ralph, F. M., Dettinger, M. D., Cairns, M. M., Galarneau, T. J., and Eylander, J. (2018). Defining "Atmospheric River": How the Glossary of Meteorology Helped Resolve a Debate. *Bulletin of the American Meteorological Society*, 99(4):837–839.

Ralph, F. M., Neiman, P. J., Kiladis, G. N., Weickmann, K., and Reynolds, D. W. (2010). A Multiscale Observational Case Study of a Pacific Atmospheric River Exhibiting Tropical–Extratropical Connections and a Mesoscale Frontal Wave. *Monthly Weather Review*, 139(4):1169–1189.

Ralph, F. M., Neiman, P. J., and Rotunno, R. (2005). Dropsonde observations in low-level jets over the northeastern Pacific Ocean from CALJET-1998 and PACJET-2001: Mean vertical-profile and atmospheric-river characteristics. *Monthly Weather Review*, 133(4):889–910.

Ralph, F. M., Neiman, P. J., and Wick, G. A. (2004). Satellite and CALJET Aircraft Observations of Atmospheric Rivers over the Eastern North Pacific Ocean during the Winter of 1997/98. *Monthly Weather Review*, 132(7):1721–1745.

Ralph, F. M., Neiman, P. J., Wick, G. A., Gutman, S. I., Dettinger, M. D., Cayan, D. R., and White, A. B. (2006). Flooding on California's Russian River: Role of atmospheric rivers. *Geophysical Research Letters*, 33(13):3–7.

Ralph, F. M., Rutz, J. J., Cordeira, J. M., Dettinger, M., Anderson, M., Reynolds, D., Schick, L. J., and Smallcomb, C. (2019b). A Scale to Characterize the Strength and Impacts of Atmospheric Rivers. *Bulletin of the American Meteorological Society*, 100(2):269–289.

Ramos, A. M., Blamey, R. C., Algarra, I., Nieto, R., Gimeno, L., Tomé, R., Reason, C. J., and Trigo, R. M. (2019). From amazonia to southern africa: atmospheric moisture transport through low-level jets and atmospheric rivers. *Annals of the New York Academy of Sciences*, 1436(1):217–230.

Ramos, A. M., Trigo, R. M., Liberato, M. L. R., and Tomé, R. (2015). Daily Precipitation Extreme Events in the Iberian Peninsula and Its Association with Atmospheric Rivers*. *Journal of Hydrometeorology*, 16(2):579–597.

Rhoades, A. M., Risser, M. D., Stone, D. A., Wehner, M. F., and Jones, A. D. (2021). Implications of warming on western United States landfalling atmospheric rivers and their flood damages. *Weather and Climate Extremes*, 32:100326.

Rodean, H. C. (1996). Stochastic Lagrangian Models of Turbulent Diffusion. *Meteorological Monographs*, 48:1–84.

Romero-Rodríguez, D. A., Soto-Mardones, L. A., Cepeda-Morales, J., Rivera Caicedo, J. P., and Inda Díaz, E. A. (2020). Satellite-derived turbidity influence factors at small river mouths, tropical Pacific coast off México. *Advances in Space Research*. Aceptado el 3 de agosto de 2020.

Rutz, J. J., James Steenburgh, W., and Martin Ralph, F. (2014). Climatological characteristics of atmospheric rivers and their inland penetration over the western united states. *Monthly Weather Review*, 142(2):905–921.

Rutz, J. J., Shields, C. A., Lora, J. M., Payne, A. E., Guan, B., Ullrich, P., O'Brien, T., Leung, L. R., Ralph, F. M., Wehner, M., Brands, S., Collow, A., Goldenson, N., Gorodetskaya, I., Griffith, H., Kashinath, K., Kawzenuk, B., Krishnan, H., Kurlin, V., Lavers, D., Magnusdottir, G., Mahoney, K., McClenny, E., Muszynski, G., Nguyen, P. D., Prabhat, M., Qian, Y., Ramos, A. M., Sarangi, C., Sellars, S., Shulgina, T., Tome, R., Waliser, D., Walton, D., Wick, G., Wilson, A. M., and Viale, M. (2019). The Atmospheric River Tracking Method Intercomparison Project (ARTMIP): Quantifying Uncertainties in Atmospheric River Climatology. *Journal of Geophysical Research: Atmospheres*, 124(24):13777–13802.

Sawford, B. L. (1991). Reynolds number effects in lagrangian stochastic models of turbulent dispersion. *Physics of Fluids A: Fluid Dynamics*, 3(6):1577–1586.

Sellars, S. L., Kawzenuk, B., Nguyen, P., Ralph, F. M., and Sorooshian, S. (2017). Genesis, Pathways, and Terminations of Intense Global Water Vapor Transport in Association with Large-Scale Climate Patterns. *Geophysical Research Letters*, 44(24):12,465–12,475.

Shearer, E. J., Nguyen, P., Sellars, S. L., Analui, B., Kawzenuk, B., Hsu, K.-l., and Sorooshian, S. (2020). Examination of global midlatitude atmospheric river lifecycles using an object-oriented methodology. *Journal of Geophysical Research: Atmospheres*, 125(22):e2020JD033425.

Shields, C. A. and Kiehl, J. T. (2016). Atmospheric river landfall-latitude changes in future climate simulations. *Geophysical Research Letters*, 43(16):8775–8782.

Shields, C. A., Rutz, J. J., Leung, L. Y., Martin Ralph, F., Wehner, M., Kawzenuk, B., Lora, J. M., McClenny, E., Osborne, T., Payne, A. E., Ullrich, P., Gershunov, A., Goldenson, N., Guan, B., Qian, Y., Ramos, A. M., Sarangi, C., Sellars, S., Gorodetskaya, I., Kashinath, K., Kurlin, V., Mahoney, K., Muszynski, G., Pierce, R., Subramanian, A. C., Tome, R., Waliser, D., Walton, D., Wick, G., Wilson, A., Lavers, D., Prabhat, Collow, A., Krishnan, H., Magnusdottir, G., and Nguyen, P. (2018). Atmospheric River Tracking Method Intercomparison Project (ARTMIP): Project goals and experimental design. *Geoscientific Model Development*, 11(6):2455–2474.

Simmons, A. J. and Burridge, D. M. (1981). An energy and angular-momentum conserving vertical finite-difference scheme and hybrid vertical coordinates. *Monthly Weather Review*, 109(4):758 – 766.

Skinner, C. B., Lora, J. M., Payne, A. E., and Poulsen, C. J. (2020). Atmospheric river changes shaped mid-latitude hydroclimate since the mid-holocene. *Earth and Planetary Science Letters*, 541:116293.

Smith, B. L., Yuter, S. E., Neiman, P. J., and Kingsmill, D. E. (2009). Water Vapor Fluxes and Orographic Precipitation over Northern California Associated with a Landfalling Atmospheric River. *Monthly Weather Review*, 138(1):74–100.

Taylor, K. E., Stouffer, R. J., and Meehl, G. A. (2012). An overview of CMIP5 and the experiment design. *Bulletin of the American Meteorological Society*, 93(4):485–498.

Ullrich, P. A. and Zarzycki, C. M. (2017). TempestExtremes: a framework for scale-insensitive pointwise feature tracking on unstructured grids. *Geoscientific Model Development*, 10(3):1069–1090.

Viale, M. and Nuñez, M. N. (2011). Climatology of winter orographic precipitation over the subtropical central Andes and associated synoptic and regional characteristics. *Journal of Hydrometeorology*, 12(4):481–507.

Viale, M., Valenzuela, R., Garreaud, R. D., and Ralph, F. M. (2018). Impacts of Atmospheric Rivers on Precipitation in Southern South America. *Journal of Hydrometeorology*, 19(10):1671–1687.

Viguera, B., Martínez-Rodríguez, M., Donatti, C., Harvey, C., and Alpízar, F. (2017). *Impactos del cambio climático en la agricultura de Centroamérica, estrategias de mitigación y adaptación. Materiales de fortalecimiento de capacidades técnicas del proyecto CASCADA (Conservación Internacional-CATIE).* Conservación Internacional.

Waliser, D. and Guan, B. (2017). Extreme winds and precipitation during landfall of atmospheric rivers. *Nature Geoscience*, 10(3):179–183.

Warner, M. D., Mass, C. F., and Salatheé, E. P. (2012). Wintertime extreme precipitation events along the Pacific Northwest Coast: Climatology and synoptic evolution. *Monthly Weather Review*, 140(7):2021–2043.

Wehner, M. F., Reed, K. A., Li, F., Prabhat, Bacmeister, J., Chen, C.-T., Paciorek, C., Gleckler, P. J., Sperber, K. R., Collins, W. D., Gettelman, A., and Jablonowski, C. (2014). The effect of horizontal resolution on simulation quality in the community atmospheric model, cam5.1. *Journal of Advances in Modeling Earth Systems*, 6(4):980–997.

Zhang, Z. and Ralph, F. M. (2021). The influence of antecedent atmospheric river conditions on extratropical cyclogenesis. *Monthly Weather Review*, 149(5):1337 – 1357.

Zhang, Z., Ralph, F. M., and Zheng, M. (2019a). The relationship between extratropical cyclone strength and atmospheric river intensity and position. *Geophysical Research Letters*, 46(3):1814–1823.

Zhang, Z., Ralph, F. M., and Zheng, M. (2019b). The Relationship Between Extratropical Cyclone Strength and Atmospheric River Intensity and Position. *Geophysical Research Letters*, 46(3):1814–1823.

Zhou, Y. and Kim, H. (2019). Impact of distinct origin locations on the life cycles of landfalling atmospheric rivers over the u.s. west coast. *Journal of Geophysical Research: Atmospheres*, 124(22):11897–11909.

Zhou, Y., Kim, H., and Guan, B. (2018). Life cycle of atmospheric rivers: Identification and climatological characteristics. *Journal of Geophysical Research: Atmospheres*, 123(22):12,715–12,725.

Zhu, Y. and Newell, R. E. (1998). A Proposed Algorithm for Moisture Fluxes from Atmospheric Rivers. *Monthly Weather Review*, 126(3):725–735.